An Empirical Investigation of Energy Transfer from the M_2 tide to M_2 Subharmonic Wave Motions in the Kauai Channel

A THESIS SUBMITTED TO THE GRADUATE DIVISION OF
THE UNIVERSITY OF HAWAIʻI IN PARTIAL FULFILLMENT OF
THE REQUIREMENTS FOR THE DEGREE OF MASTER OF
SCIENCE IN OCEANOGRAPHY

May 2013

By
Sherry H. Chou

Thesis Committee:

Douglas S. Luther, Chair
Janet M. Becker
Glenn S. Carter
Mark Merrifield

We certify that we have read this thesis and that, in our opinion, it is satisfactory in scope and quality as a thesis for the degree of Master of Science in Oceanography.

Thesis Committee Chair: Douglas Luther

Glenn Carter

Mark Merrifield

ACKNOWLEDGEMENTS

Abstract

Long-duration observations of horizontal currents throughout nearly the entire water column at a location in the Kauai Channel, Hawaii (21.75˚N, 158.75˚W), are used to test hypotheses about the existence of energetic oscillations driven by non-linear processes acting on the semi-diurnal tide. For decades it has been believed that three classes of resonant interactions, based on weakly interacting, non-linear wave theory, are the dominant mechanisms for moving energy through frequency-wavenumber space of the internal wave field. Energy is thought to flow from sources, such as the tides and wind-forced inertial waves, toward small spatial scales and dissipation. A number of recent studies have suggested that non-linear processes, such as Parametric Subharmonic Instability, will result in a flow of energy from the principal semi-diurnal M_2 tide directly and quickly into small-vertical-scale oscillations at the M_2 subharmonic frequency, $M_1 = M_2/2$ (0.966 cycles/day, or cpd), and that this can occur anywhere equatorward of 28.8˚ latitude. However, numerical experiments have been highly idealized, and most observational studies lack sufficient frequency resolution to spectrally distinguish between linear diurnal tidal constituents and oscillations of M_1 frequency.

Observations for this study come from moored Acoustic Doppler Current Profilers (ADCPs) which were deployed from November 2002 to June 2003 in the Kauai Channel as part of the Hawaii Ocean Mixing Experiment (HOME). These velocity time-series cover nearly the entire water column with 8-m resolution, and are long enough to clearly resolve in frequency the energy in M_1 currents as distinct from currents forced by the principal diurnal tidal constituents O_1 (0.930 cpd) and K_1 (1.003 cpd). Energetic semi-diurnal tidal beams are observed in this dataset, and diurnal-band spectral energies in both velocity and shear fields appear to be dominated by locally generated internal tides at O_1 and K_1. The ratio of velocity power spectral densities at M_1 relative to M_2 is approximately 10^{-2}, which is lower than expected from some numerical simulations. We find with bispectral analysis that a triad of waves with frequencies at O_1, K_1 and M_2 has higher bispectral energy (by an order of magnitude) and higher bicoherence (> 0.1) than a triad with frequencies at M_1, M_1 and M_2 from 420-1000 m at this location.

Contents

1. INTRODUCTION

1.1 Tidal Energetics and Mixing

Tidal forcing from the Sun and Moon generates 3.7 Terawatts (TW) of mechanical power, of which 3.5 TW is dissipated in the ocean (Munk and Wunsch, 1998). Satellite altimeter data has revealed that approximately 1 TW of the barotropic tide is likely dissipated in the deep oceans, predominantly in regions of rough bottom topography (Ray and Mitchum, 1996, 1997; Egbert and Ray, 2000, 2001, 2003). These findings suggest tides are a potentially significant source of energy for diapycnal mixing and hence maintaining the density stratification of the global ocean.

The Hawaiian Ridge was identified by acoustic experiments and satellite altimetry as a region of significant deep-ocean barotropic tidal energy loss as well as a probable source of energetic internal tides (Dushaw et al., 1995; Ray and Mitchum, 1996). The Hawaii Ocean Mixing Experiment (HOME) is an integrated program of historical data analysis, modeling, and observations focused on tidally driven mixing at the Hawaiian Ridge. Specifically, HOME was formulated with three main goals: **1.** to determine whether the tide is a major energy source leading to significant mixing at the Hawaiian Ridge; **2.** to develop a quantitative energy budget which includes barotropic and baroclinic tidal energy loss as well as local dissipation; **3.** to identify the main mechanisms which transfer energy from large to small scales (Pinkel et al., 2000).

By the time HOME field programs were completed in 2003, it had became clear through historical data analysis (Finnigan et al., 2002), numerical modeling (Johnston and Merrifield, 2003), and in-situ measurements (Rudnick et al., 2003) that tides were indeed

a major energy source associated with enhanced mixing at the Hawaiian Ridge. Due to

the predominantly cross-isobath tidal flow and the steep topography of the Hawaiian

Ridge, the majority of the energy lost from the semi-diurnal barotropic tide goes into

forcing low mode internal tides that radiate away, and only a small fraction of the

barotropic tide is dissipated locally through turbulence (St. Laurent and Garrett, 2002;

Zaron and Egbert, 2006). A model study of the Kaena Ridge region in the Kauai Channel

between the islands of Oahu and Kauai (Carter et al., 2008) estimates that of the energy

lost from the M_2 barotropic tide in this region, approximately 6% is lost to dissipation by

bottom friction and ~85% is converted to internal tides (of which ~74% radiates away

from the study region and only ~19% is locally dissipated).

Quantifying the rate of tidal energy loss and closing the energy budget for the

Hawaiian Ridge have proven to be challenging tasks. Estimates of barotropic tidal

energy loss (Egbert and Ray, 2001, 2003), internal tide generation and dissipation

(Kang et al., 2000; Merrifield and Holloway, 2002; Johnston and Merrifield, 2003;

Zaron and Egbert, 2006; Martin and Rudnick, 2007; Carter et al., 2008; Zaron et al.,

2009; Klymak et al., 2010), and directly measurable dissipation (Klymak et al., 2006)

all have non-negligible error-bars and levels of uncertainty.

With respect to the third goal of HOME, internal tide generation and

dissipation are important aspects of cross-scale energy transfer which have become

better understood. A number of modeling studies (Merrifield et al., 2001; Merrifield

and Holloway, 2002; Carter et al., 2008) have produced simulations of internal tide

generation which are consistent with observations. Shear and convective instabilities

have been suggested as mechanisms for tidal dissipation in flows along the steeply sloped ridge bottom, based on Thorpe scale analysis of tidally driven overturns on the southern flank of Kaena Ridge (Aucan et al., 2006). Density overturns also were observed in moored measurements of temperature near the ridge top, usually during periods of reduced background stratification associated with vertical strain of the internal tide (Levine and Boyd, 2006). In contrast to the southern flank of Kaena Ridge, the northern flank is exposed to near-inertial waves generated by winter storms north of the ridge, which combine with internal tidal motions to induce high-strain conditions leading to mixing (Aucan and Merrifield, 2008).

Non-linear interactions between internal waves have long been conjectured as playing a dominant role in the transfer of energy from large to small scales, although there is still much uncertainty about the importance of specific processes (St. Laurent and Garrett, 2002). Observations from HOME have been used to identify Parametric Subharmonic Instability (PSI) as a possible mechanism for energy transfer from the large-scale baroclinic tides down to smaller vertical scales at Kaena Ridge (Carter and Gregg, 2006; Rainville and Pinkel, 2006a; Sun, 2010). However, the datasets used by these studies are relatively short in duration (≤ 6 weeks), and consequently the results obtained are limited in their frequency resolution and statistical reliability. The significance of this limitation will be discussed further in Chapter 5.

1.2 Energy Transfer through Non-linear Resonant Interactions

Although barotropic tidal dissipation is associated with enhanced mixing at the

Hawaiian Ridge, numerical modeling and observations from HOME show that

approximately 62% of the barotropic tidal energy lost in the Kaena Ridge study region is

transferred to low mode internal tides which do not dissipate locally (Carter et al., 2008).

In general, internal waves represent a significant portion of observed variability in the

ocean (Müller, 1986), and internal wave breaking is thought to be a main cause of

diapycnal mixing (e.g. St. Laurent and Garrett, 2002; Gregg et al., 2003). The breaking of

internal waves has been observed to occur at scales of ~100 m (Aucan et al., 2006),

which is small compared to the km scales of internal wave generation. The energy

cascade in wavenumber space can potentially span many orders of magnitude as energy is

transferred from the large-scale waves directly forced by the tides to the smaller scale

internal waves which are more easily dissipated (Polzin, 2004).

An important advance in the study of internal wave dynamics occurred with the

development of a model of the internal wave spectrum using observations and linear

wave theory (Garrett and Munk, 1972, 1975). The general shape of the Garrett-Munk

(GM) model spectrum is thought to be invariant in the ocean due to redistribution of

energy from large to small vertical scales through topographic scattering and non-linear

wave-wave interactions (McComas and Bretherton, 1977; Garrett and St. Laurent, 2002).

According to weakly interacting, non-linear wave theory, there are three main

classes of resonant wave-wave interactions[1] which contribute to energy transfer rates in

---

1   Energy redistribution through resonant non-linear interactions was first described in the fluid dynamical
    context using surface gravity waves as an example (Phillips,1960); perturbation expansion of the
    Fourier components of surface displacement showed that the dominant mechanism of energy transfer
    resulted from tertiary interaction terms whose amplitudes grow linearly with time.

different parts of the GM spectrum: **1.** induced diffusion, **2.** elastic scattering, and **3.** PSI

(McComas and Bretherton, 1977). The conditions for resonance among a triad of waves

with wave number $\mathbf{k}_j$ and frequency ω_j are:

$$\mathbf{k}_1 \pm \mathbf{k}_2 = \mathbf{k}_3 \tag{1}$$

$$\omega_1 \pm \omega_2 = \omega_3 \tag{2}$$
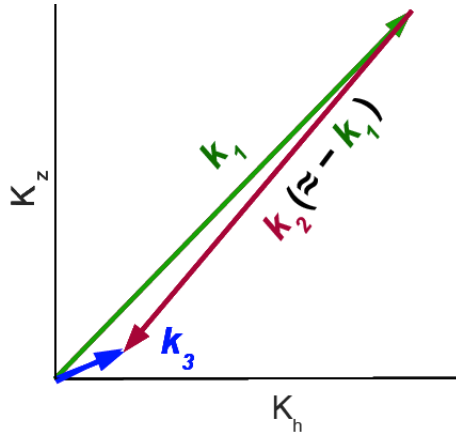
Figure 1.1 Wave number vector diagram of a triad of waves in the PSI class, as
defined by McComas and Bretherton (1977).

In the case of PSI triads (Fig. 1.1), a large-scale primary wave ($\mathbf{k}_3$) can transfer

energy to 2 small-scale secondary[2] waves of approximately opposite wave numbers and

nearly equal frequencies, at a rate proportional to the energy of the primary wave

(McComas and Bretherton, 1977). Although PSI was first observed in a laboratory setting

less than 50 years ago (Korobov and Lamb, 2008), the excitation of subharmonic surface

gravity waves was documented almost two centuries ago by Faraday (1831). In the

context of internal tides, energy from the principal semi-diurnal M_2 tide could be

---

2   What are often called *parent* and *daughter* waves will be referred to as *primary* and *secondary* waves,
    respectively.

transferred by PSI to a pair of internal waves whose frequencies add to M_2, at latitudes where the secondary waves can propagate as free waves[3]. As discussed by McComas and Müller (1981), initial estimates of energy transfer rates relied on the random-phase approximation put forward by Hasselmann (1966), and led to the conclusion (Olbers and Pomphrey, 1981) that at all latitudes PSI was ineffective and negligible as a mechanism for redistributing tidal energy in the internal wave spectrum.

Interest in PSI as a resonant interaction facilitating cross-scale energy transfer and mixing has grown within the last decade based on numerical simulations such as Hibiya et al. (2002), which showed that energy transfer from semi-diurnal tide to near-inertial waves of higher vertical wave-numbers was possible for the Hawaiian Ridge location at 23°N (equatorward of the ½M_2 Subharmonic Turning Latitude[4], or M_1 SHTL) and not for the Aleutian Ridge location at 53°N. Related observational studies found elevated shear and diapycnal diffusivity at the Hawaiian Ridge when compared to the Aleutian Ridge (Nagasawa et al., 2002; Hibiya and Nagasawa, 2004). Results from a more sophisticated numerical model which considered a larger range of latitudes (MacKinnon and Winters, 2005) further suggested that PSI could rapidly transfer substantial fractions of energy from the M_2 internal tide to small-scale waves and turbulent dissipation, at latitudes close to the M_1 SHTL.

A large and growing number of empirical studies (Carter and Gregg, 2006; Rainville and Pinkel, 2006a; Alford et al., 2007; Toole, 2007; Alford, 2008; Sun, 2010;

---

3 Free internal waves are restricted to having frequencies between the Coriolis parameter $f = 2\Omega \sin \lambda$ (where Ω is the rate of Earth's rotation and λ is latitude) and the buoyancy frequency N.

4 The turning latitude of M_2 subharmonic waves is defined as the latitude where Coriolis parameter $f = $ ½M_2, i.e. $\sin^{-1}$ (½$M_2/2\Omega$) = 28.8°, and is often referred to as the "critical latitude".

Xie et al., 2011; Sun et al., 2011; Chinn et al., 2012; Liao et al., 2012; MacKinnon et al.,

2013a, 2013b) and numerical modeling studies (Lamb, 2004; Gerkema et al., 2006;

Simmons, 2008; Korobov and Lamb, 2008; Nikurashin and Legg, 2011; Hazewinkel and

Winters, 2011) have continued these lines of inquiry to investigate the workings and

importance of non-linear energy transfers from the M_2 internal tide. Some have suggested

that processes such as PSI will result in a flow of energy from the M_2 tide directly and

quickly into small-vertical-scale oscillations at M_1, the M_2 subharmonic frequency (Table

1.1), where it can immediately influence the occurrence of instabilities and mixing. In

addition to observational and numerical studies, analytical (Foda and Hill, 1998; Young et

al., 2008) and experimental (Joubaud et al., 2012; Bourget et al., 2013) studies of PSI

have also been carried out. However, much uncertainty remains about the spectral

characteristics and energy transfer rates of such non-linear processes, as experiments

have so far been highly idealized, and observational studies have not been based on

spatially and temporally comprehensive datasets.

Authors	Summary	Main Results
Hibiya and Nagasawa, 2004	Observations show elevated shear and diapycnal diffusivity at the Hawaiian Ridge when compared to the Aleutian Ridge.	Supportive of model results from Hibiya et al., (2002) showing PSI was active in moving tidal energy to smaller scales and facilitating mixing.
MacKinnon and Winters, 2005 (MW05)	Idealized numerical study using 3-D model of Winters et al. (2004) and constant buoyancy frequency N ; initialized with poleward propagating mode-one internal waves of M_2 frequency. Model domain is (3300x3300x4) km, from 15°- 45°N.	Significant (62%) and rapid (10-day timescale) loss of M_2 tidal energy at the M_1 SHTL, accompanied by increased spectral energy at M_1 frequency and turbulent dissipation rate. Ratio of M_1 and M_2 spectral energy (in velocity field): >10 at 29°N, ~10^{-1} at 24°N, ~10^{-2} at 22°N.
Gerkema et al., 2006	Non-linear and non-hydrostatic model (MIT-gcm) in 2-D and with constant N simulates internal tide generation (forced by M_2 barotropic tide) over a continental slope. Model domain is (350x4) km, with run time ~8 days.	Energy is transferred from M_2 to M_1 very rapidly (2-day timescale) at 27.5°N and at the equator. Ratio of M_1 and M_2 spectral energy (velocity): ~10^{-3} at 45°N, ~1 at 27.5°N, ~10^{-2} at equator.
Carter and Gregg, 2006	Shipboard Doppler sonar was used to measure velocity over the Kaena Ridge Crest (~22°N) for 22 days, along 12 survey lines spread over a 35-km section of the ridge.	Bispectral analysis of current and shear fields suggests coupling of M_2 internal tide and M_1 frequency waves between 525-595 m. Ratio of M_1 and M_2 spectral energy (velocity, shear): (~10^{-1}, ~10).
Simmons et al. (2008)	2-D global baroclinic tidal model initialized with semi-diurnal internal tides was used to calculate vertical displacement spectra for latitude bands in the North Pacific (20°N, 30°N, 40°N).	Spectral analysis "clearly indicates that the large amplitude disturbances are at the M_2/2 [M_1] frequency". Ratio of M_1 and M_2 spectral energy (vertical displacement): ~1 at 30°N, <10^{-2} at 20°N.
Sun, 2010	Velocity and density profiles were collected aboard the R/P FLIP during a 6-week deployment on the southern flank of Kaena Ridge (21.68°N), where water depth was ~1100 m.	Bispectral analysis shows significant bicoherence between diurnal-band shear and semi-diurnal-band vertical velocity, suggesting transfer of energy from M_2 tide to M_1 waves via PSI.
Xie et al, 2011	Moored current measurements from 52-436 m were collected for ~75 days in the South China Sea (20.58°N), where water depth was ~2500 m.	Spectral and bispectral analysis of M_1 and M_2 waves shows "rapid, persistent energy transfer to PSI-triads. Clearly, PSI is one of dominant mechanisms of the cascade of internal tidal energy down to small dissipation scales available for mixing."
Liao et al., 2012	Moored current measurements from 30-190 m were collected for > 8 months in the Luzon Strait (20°N), where water depth was ~2760 m.	Bispectral analysis suggests M_1 internal waves are non-linearly coupled with the M_2 internal tide. Ratio of M_1 and M_2 spectral energy (velocity, shear): (~$^1/_2$, ~10^{-1}).

Table 1.1 Studies which suggest PSI transfers energy from M_2 tide to M_1 internal waves.

1.3 Project Objectives

The HOME dataset under present study is unique in its temporal extent and depth coverage. A long dataset is essential for studying tidal phenomenon near the M_1 frequency, due to the presence of diurnal internal tides. The top row and first column of Table 1.2 show the frequencies of interest in this study, and the frequency differences are shown in the matrix. The frequency separation between the luni-solar diurnal tide K_1 and M_1 is nearly the same as the separation between M_1 and the principal lunar diurnal tide O_1 (~ 0.037, double boxed in the matrix). According to the Rayleigh criterion from classical optics (Emery and Thomson, 2004), the minimum record length T needed to distinguish between two adjacent spectral peaks separated by df = 0.037 cpd is approximately 1/df $\sim$ 27 days. However, even with pure sinusoidal inputs, T > 41 days is needed to resolve three adjacent spectral peaks (Fig1.2).

Frequencies (cpd)		1.9323 M_2	1.0027 K_1	0.9662 M_1	0.9295 O_1	0.7432 f (A2)	0.7394 f (C2)
1.9323	M_2	--	0.9296	0.9662	1.0028	1.1891	1.1929
1.0027	K_1		--	0.0365	0.0732	0.2595	0.2633
0.9662	M_1			--	0.0367	0.2230	0.2268
0.9295	O_1				--	0.1863	0.1901
0.7432	f (A2)					--	0.0038
0.7394	f (C2)						--
DFT cycles per record length		316	164	158	152	121	
DFT cycles per day		1.9323	1.0029	0.9662	0.9295	0.7399	

Table 1.2 Frequencies of interest are shown in cycles per day (cpd) in the first row and column; differences are shown in the matrix. Inertial frequency f is calculated for the HOME A2 and C2 mooring locations. Nearest Discrete Fourier Transform (DFT) harmonics for T = 163.5 days are shown for comparison (bottom 2 rows).
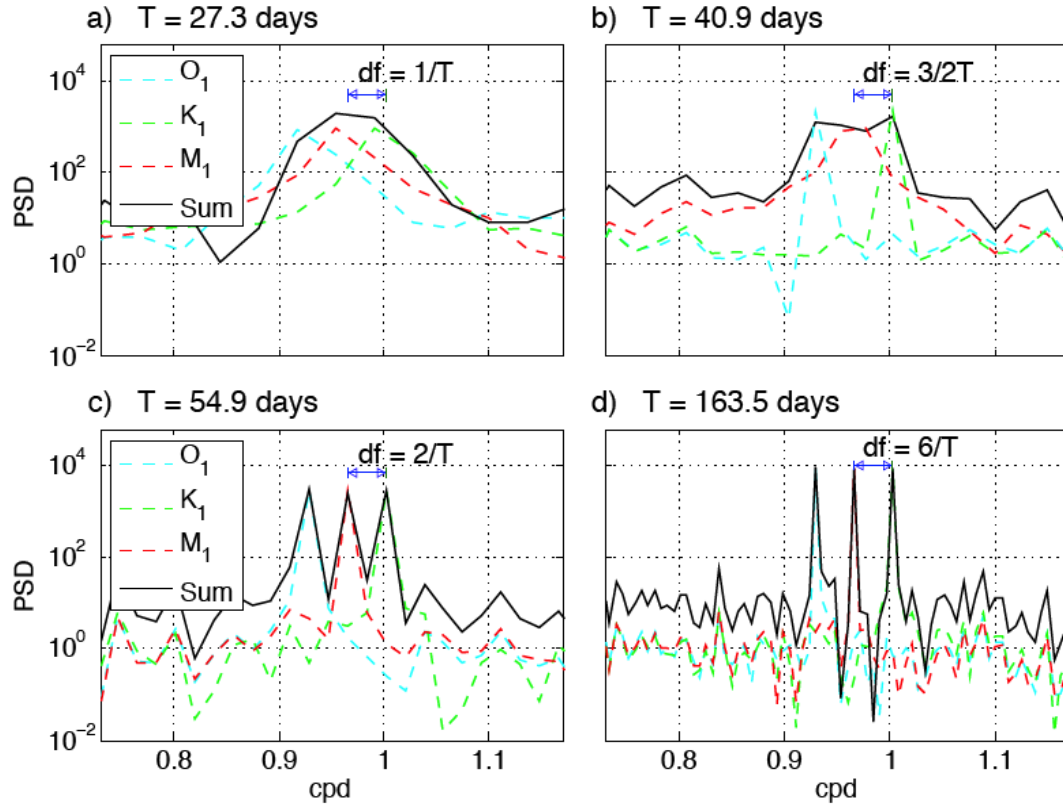
Figure 1.2 Frequency spectra of synthetic sinusoidal signals with frequencies in the diurnal band (O_1, K_1, and M_1) and pseudo-randomly generated red noise show that **a)** separation of DFT harmonics by df is insufficient for resolving spectral peaks separated also by df; **b)** record length of T=3/2df is still insufficient for resolving three adjacent spectral peaks; **c)** a minimum record length of T=2/df is needed to resolve purely sinusoidal signals with O_1, K_1, and M_1 frequencies; **d)** the present study uses record length of 163.5 days, which result in Fourier Transform harmonics being separated by 0.006 cpd, or df/6.

Using input signals with more realistic bandwidth (~0.03 cpd, which is a lower bound estimate for the O_1 and K_1 shear spectral peaks observed at this location), the record length requirement for separating the spectral contributions of O_1, K_1 and M_1 becomes even larger (Fig. 1.3). Although a 75-day time-series, such as that used by Xie et al. (2011), can show separate O_1 and K_1 peaks in the kinetic energy spectrum, diurnal band energy in the shear variance spectrum appears centered near M_1 as one broad peak

due to increased bandwidth at the higher vertical wavenumbers emphasized by shear.

With a record of 163.5 days, separate spectral peaks in the diurnal band of the shear

variance spectrum become apparent. Bandwidth, frequency resolution, spectral leakage,

and statistical reliability are important issues to consider in spectral analysis, and will be

discussed in more detail in Chapters 3 and 5.
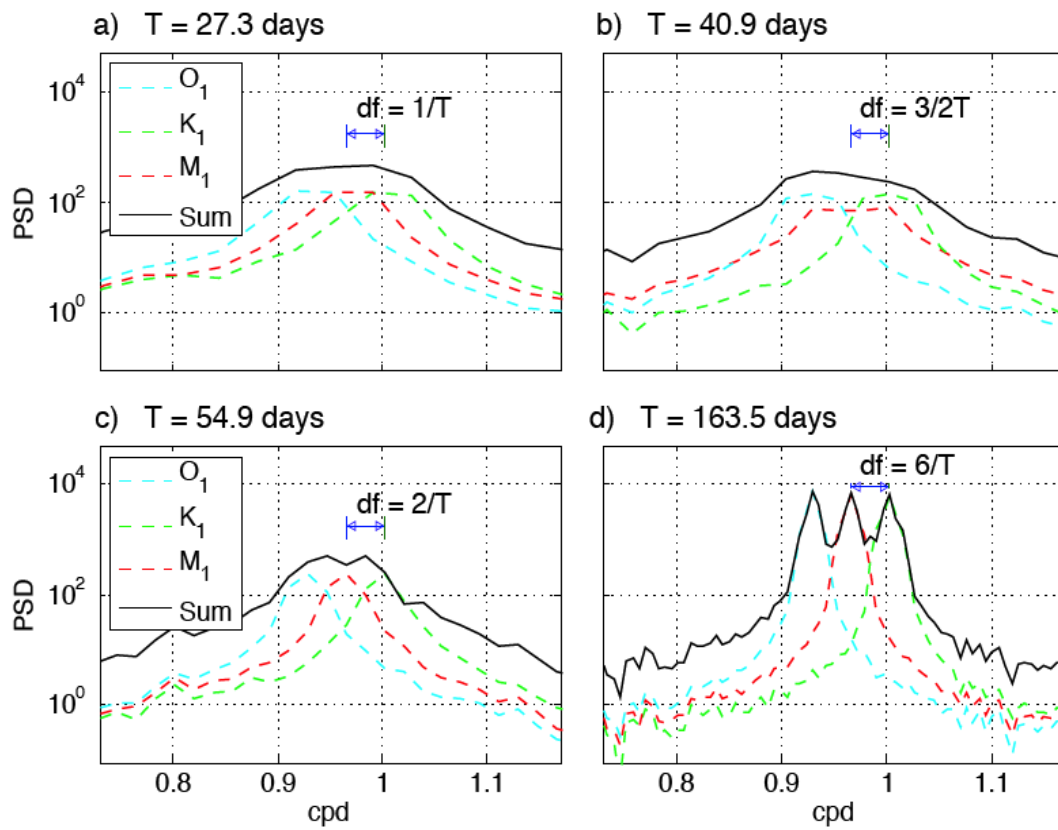
Figure 1.3 Frequency spectra for synthetic time-series with frequencies in the diurnal band, as in Fig. 1.2, and bandwidth of 0.03 cpd (by summing five sinusoids whose frequencies differ by 7.5×10^{-3} cpd, with the largest amplitude in the middle frequency) show that record lengths equal to **a)** 1/df, **b)** 3/2df, and **c)** 2/df are insufficient for resolving three adjacent spectral peaks separated by df = 0.037; **d)** has sufficient resolution, using record length of 163.5 days (6/df).

The principal purpose of this work is to quantify the energy at M_1, relative to M_2 internal tide energy, with a dataset from HOME that has sufficient length in time to clearly resolve in frequency the energy in M_1 horizontal currents as distinct from the O_1 and K_1 currents, and has a unique vertical extent (~1000 m) that encompasses both a distinct, depth-limited beam of semi-diurnal tide energy and a bottom semi-diurnal tide generation site (Zilberman et al., 2011). The presence of energetic internal tides is important because there are suggestions (Carter and Gregg, 2006; Gerkema et al., 2006; Simmons et al., 2008) that tidal beams, as opposed to just low-vertical-mode inputs, yield faster transfer of energy from M_2 to M_1. A secondary purpose of the present study is to provide a direct assessment of the occurrence of non-linear interactions between M_2 and M_1 in this unique HOME dataset, using bispectral analysis.

1.4 Summary

Internal waves are known to be a crucial source of energy for such phenomena as deep ocean mixing that maintains, with subduction, the abyssal stratification. However, the energy cascade from large, generation scales to small, dissipation scales is a fundamental aspect of diapycnal mixing that is not well understood. Non-linear processes, such as PSI, have been conjectured to be the main mechanisms for facilitating this energy cascade (McComas and Bretherton, 1977; Hibiya et al., 2002; Furuichi et al., 2005; Xie et al., 2011), with many studies suggesting that direct and rapid energy transfer from the large-scale M_2 tide to small-scale oscillations at the M_1 frequency can occur anywhere within the tropics (Table 1.1). Observational efforts to demonstrate the

existence of non-linear energy fluxes from M_2 to M_1 usually have not explicitly

distinguished non-linearly produced M_1 energy from diurnal-band barotropic and internal

tides, due to insufficient data length. The present study will quantify the spectral energy

of M_1 relative to M_2, and consider whether there is observable non-linear interaction

between waves of these two frequencies.

The dataset used in this study is introduced in Chapter 2, and the methods used for

spectral analysis are described in Chapter 3. The results and discussion are presented in

Chapters 4 and 5, and the Conclusion in Chapter 6.

2. HOME OBSERVATIONS

The Nearfield phase of HOME was designed to observe mixing processes over the Hawaiian Ridge in enough detail to determine their dynamics, which can then be assimilated into models and generalized to other locations (Boyd et al., 2005). There are four main components in the Nearfield program: High Frequency (HF) radar (Chavanne et al., 2010a, 2010b), moorings (Boyd et al., 2005; Aucan et al., 2006; Aucan and Merrifield, 2008; Guiles, 2009; Zilberman et al., 2011), Research Platform Floating Instrument Platform (R/P FLIP) (Rainville and Pinkel, 2006a, 2006b; Rainville et al., 2010; Sun, 2010; Sun and Pinkel, 2012; Pinkel et al., 2012), and mobile instruments such as SeaSoar, microstructure profilers and Doppler sonars (Carter and Gregg, 2006; Klymak et al., 2006, 2008; Martin and Rudnick, 2007; Klymak and Moum, 2007a, 2007b; Cole et al., 2009).

2.1 Moorings A2 and C2

This study is focused on the HOME A2 and C2 moorings, which were deployed in the Kauai Channel from November 2002 to June 2003. The location of the A2 mooring was 21° 45.14' N, 158° 45.42' W, and the C2 mooring was located ~17 km to the southwest at 21° 38.06' N, 158° 51.60' W (Fig. 2.1). The purpose of the A2 mooring (at water depth of ~1300 m) was to sample the water column as completely as possible, with a total of 3 Acoustic Doppler Current Profilers, or ADCPs (two 75 kHz Workhorse Long Rangers and one 300 kHz Workhorse Mariner), 31 temperature sensors, 18 conductivity sensors, and 22 pressure sensors. The C2 mooring (at depth of ~4000 m) sampled the upper 900 m with 2 ADCPs (one 75 kHz Long Ranger and one 300 kHz Mariner), 10

conductivity sensors, and 7 pressure sensors; 31 temperature sensors were positioned

throughout the whole water column. All the ADCPs were positioned to be upward-
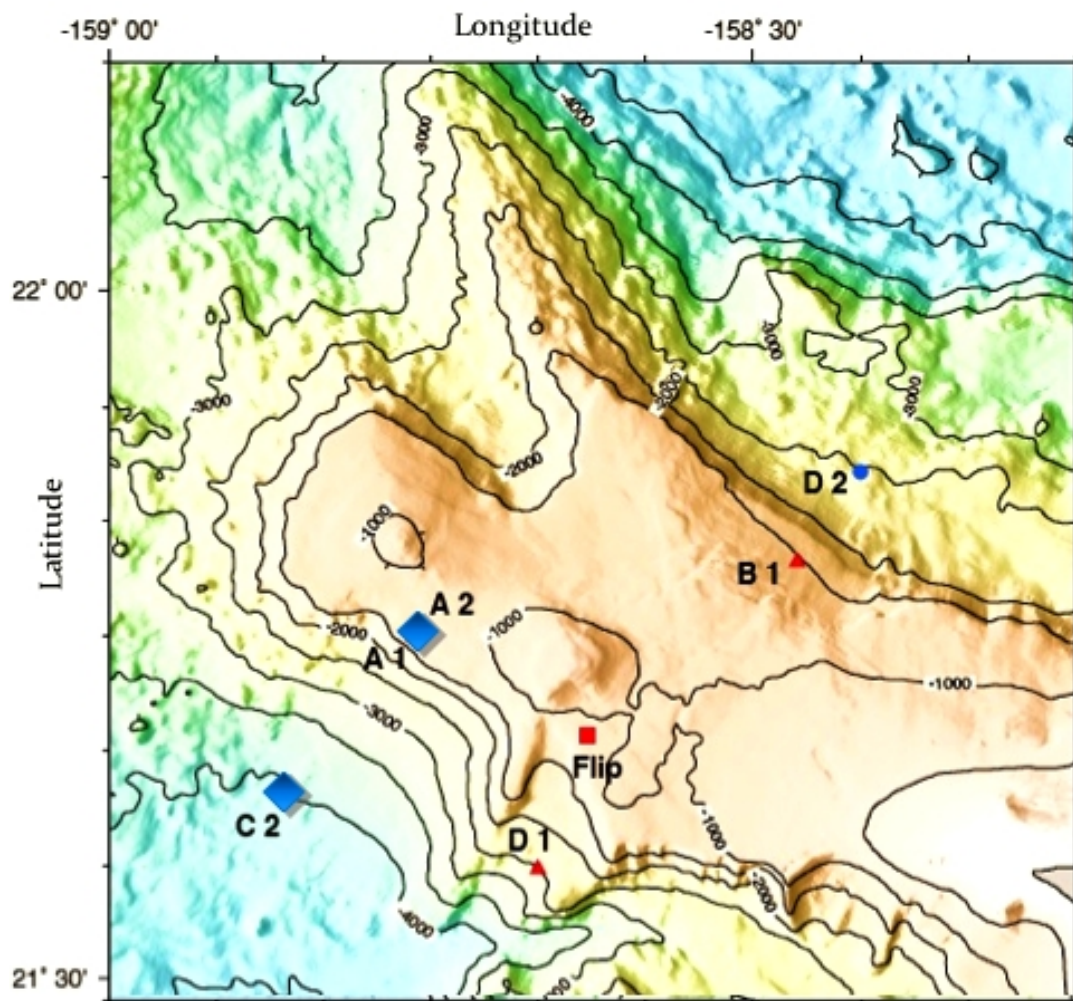
looking.

Figure 2.1 The locations of HOME A2 and C2 moorings (blue squares) are shown on a bathymetry map of Kaena Ridge, with contour lines every 500 m depth. Observation sites of the R/P FLIP and HOME moorings A1, B1, D1 and D2 are also shown (figure from D. Luther, adapted and used with permission).

This study uses data from three RDI Long Ranger ADCPs from the HOME A2 and C2 moorings. The basic characteristics of the utilized dataset are summarized in Table 2.1 (reasons for data truncation in the time domain will be discussed in Chapter 3). There were four main problems with data quality which resulted in reductions of usable data: **1.** poor signal return due to diurnal vertical migration of biological scatterers or large distance from the instrument (Boyd et al., 2005) (Fig. 2.2), **2.** acoustic side-lobe reflection from mooring line hardware (Boyd et al., 2005), **3.** interference between the upper and lower ADCPs on the A2 mooring during the first ~20 days of deployment (Guiles, 2009) and **4.** early termination of sampling by the A2 lower ADCP on May 16, 2003 (Boyd et al., 2005).

Mooring location	Instrument	Sampling period	Instrument (water) depth	[Depths used]/ Total	[Subset:02 Dec. 2002 - 15 May 2003]/Total
A2 (upper) (21.75° N 158.75° W)	RDI 75-kHz Long Ranger ADCP	16 minutes	746 m (1333 m)	[344 - 704] m/ [160 - 728] m (64%)	163.5 days / 207.8 days (79%)
A2 (lower) (21.75° N 158.75° W)	RDI 75-kHz Long Ranger ADCP	16 minutes	1314 m (1333 m)	[728 - 1240] m/ [720 - 1296] m (89%)	163.5 days/ 181.5 days (90%)
C2 (21.63° N 158.86° W)	RDI 75-kHz Long Ranger ADCP	10 minutes	743 m (4029 m)	[344 - 704] m/ [200 - 720] m (63%)	163.5 days/ 207.3 days (79%)

Table 2.1 Basic information about the ADCP dataset used in this study.

Overall, the data from Long Ranger ADCPs used in the Nearfield Program were of high quality, and benefited from the testing and adjustments made from ADCP deployments during the HOME Survey phase (Boyd et al., 2005). However, there was evidence of temporal as well as spatial variability in the quality of ADCP data due to the

above mentioned problems, and care has been taken in the present study to identify and

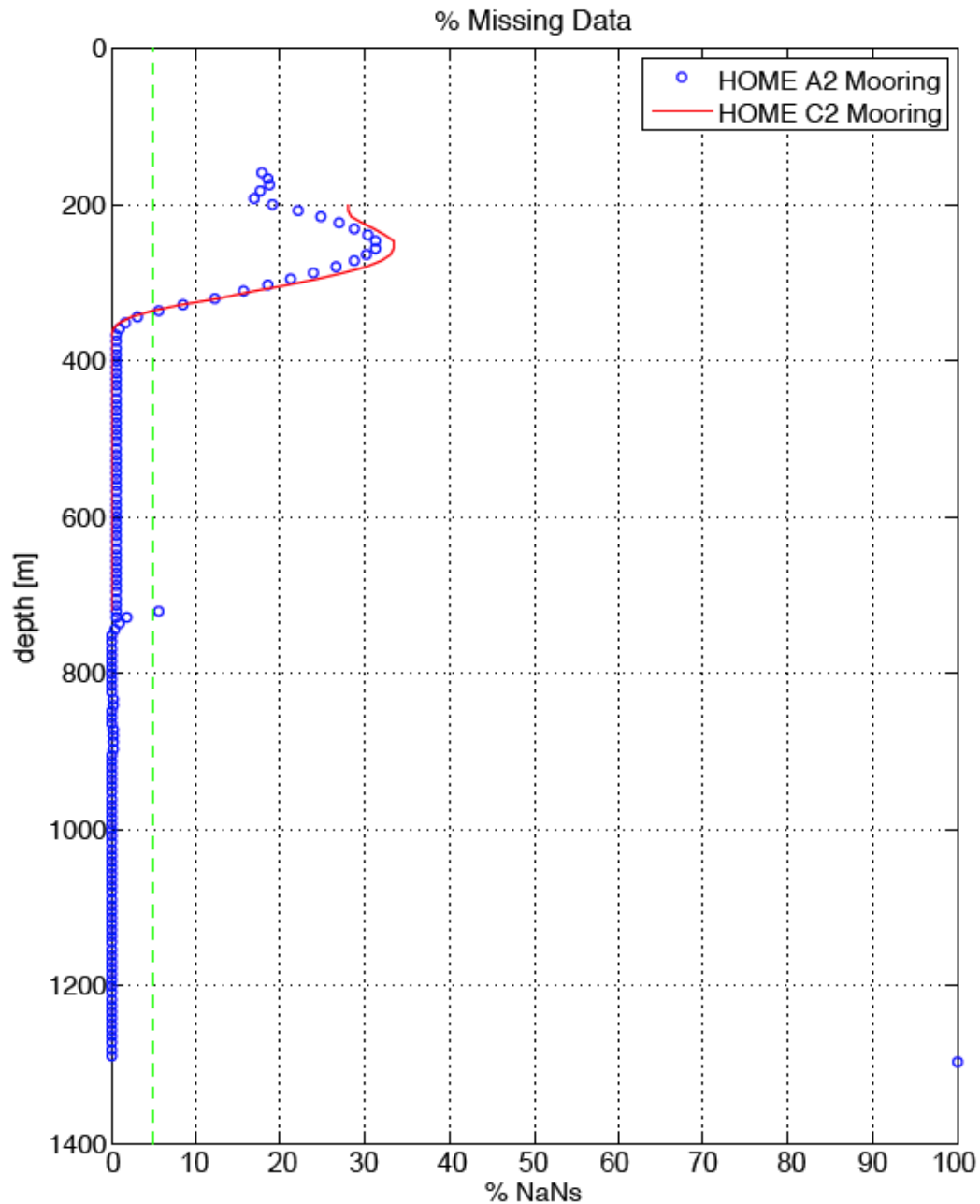remove segments of poor data quality following Guiles (2009) and Boyd et al. (2005).

Figure 2.2 Percentage of missing data due to poor signal return for the LR ADCPs were high above 350 m due to the diurnal vertical migration of biological scatters. Distance from the instrument is also a cause of poor signal return. Data from depths which show more than 5% of missing data (green dashed line) will not be considered in this study.

2.2 Locally Generated Internal Tides

Model estimates of energy flux at Kaena Ridge (Merrifield and Holloway, 2002) show beams of concentrated M_2 baroclinic energy moving up and away from the Ridge (Aucan et al., 2006). The HOME A2 and C2 moorings were designed to intersect the locally generated internal tide beams, and observations have verified the model predictions (Carter et al., 2008).

a. Semi-diurnal Internal tides

The presence of high-energy-density internal tidal beams is important to establish, as observational (Carter and Gregg, 2006) and numerical (Gerkema et al., 2006; Simmons, 2008) studies have emphasized the correlation between occurrence of non-linear energy transfer and tidal beams. Examination of minimally processed current measurements alone suggests that the HOME moorings A2 and C2 were within the path of locally generated and energetic semi-diurnal internal tides, which display beam-like structure. The current fields measured at 620 m on the A2 mooring (Fig. 2.3b) show clear indication of the spring-neap cycle and the approximately 12-hour period of semi-diurnal tides, with current vectors rotating anti-cyclonically, as expected of internal waves. At 420 m (Fig. 2.3a) and 804 m (Fig. 2.3c), the current fields display less regularity but still have clear signs of being dominated by semi-diurnal internal tides.
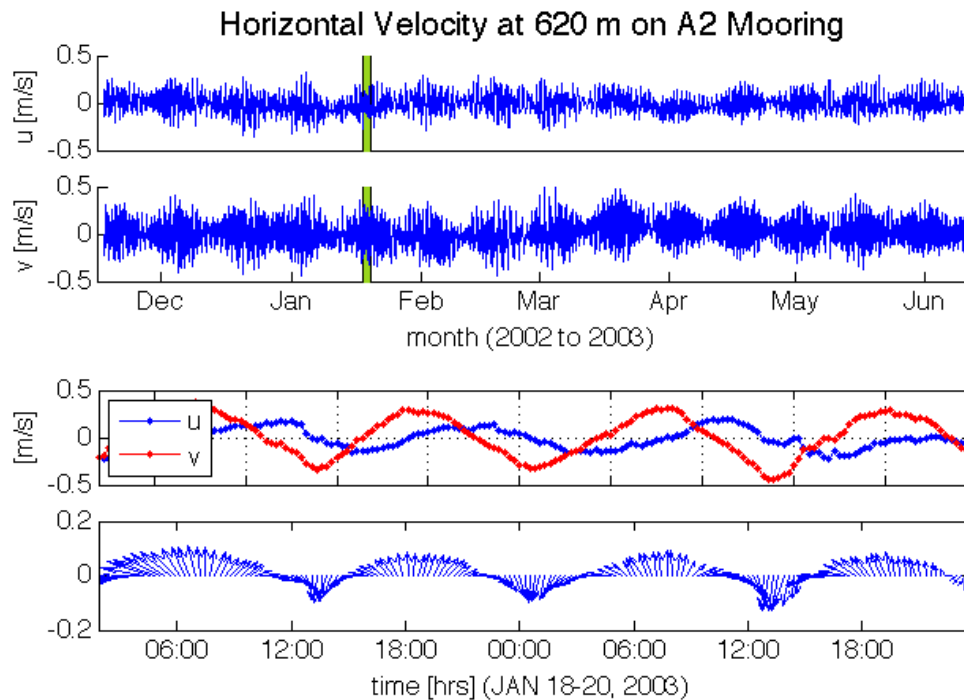
(a)
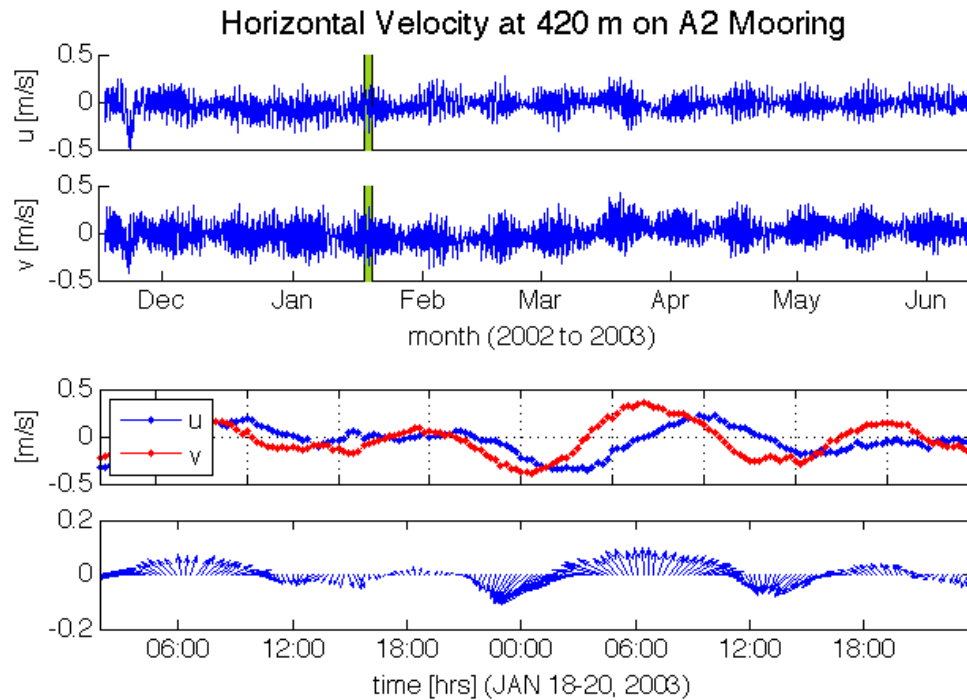
(b)

Figure 2.3 a-b) Horizontal current measurements from the HOME A2 mooring, averaged over 72 m and centered at 420 m **(a)** and 620 m **(b)**. At each depth, the top 2 panels show the full time-series, and the bottom 2 panels show two-day insets from January 18-20, 2003.

(c)
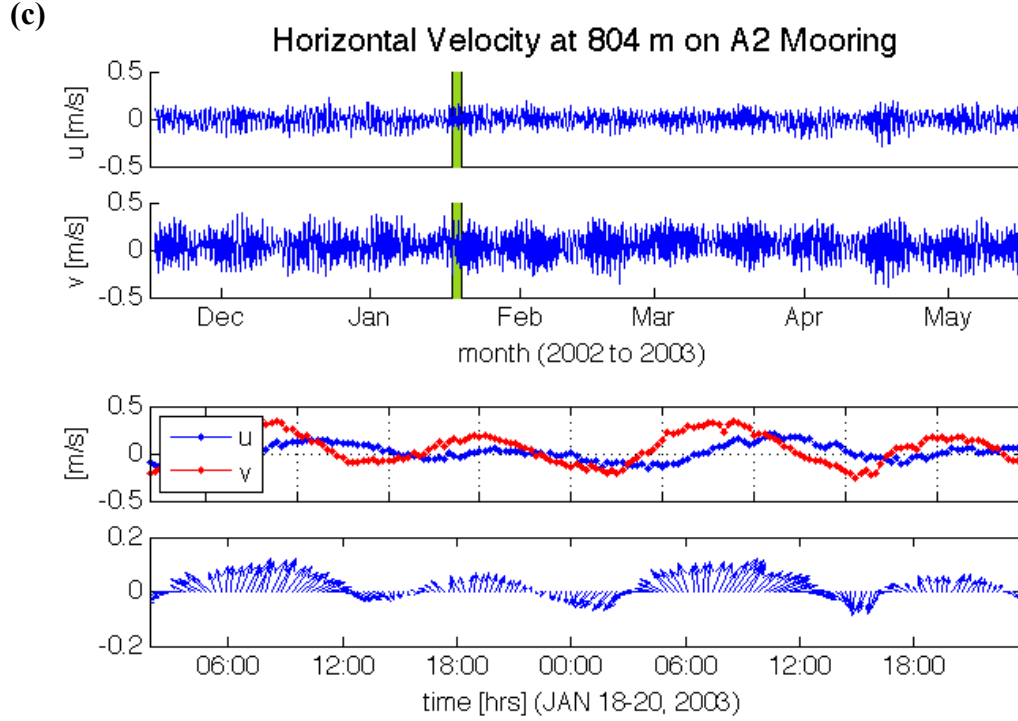
Figure 2.3 c) Horizontal current measurements from the HOME A2 mooring, averaged over 72 m and centered at 804 m.

Internal tides generated at Kaena Ridge are expected to have traveled farther up the water column from the A2 mooring to the C2 mooring location. Using equations for internal gravity waves in a rotating fluid with uniform buoyancy frequency N (Gill, 1982), the aspect ratio α of internal wave energy is:

$$\alpha \; = \; \frac{\text{vertical scale}}{\text{horizontal scale}} \; = \; \left(\frac{\omega^2 \; - \; f^2}{N^2 \; - \; \omega^2} \right)^{1/2} \tag{3}$$

Approximating N^2 as 2.8x10^{-5} [rad/s^2] (the 300-800 m depth average for Station Kaena at 21.85°N) gives $\alpha \sim 0.025$ for the M$_2$ internal tide. Accordingly, vertical displacement of ~425 m would be expected over the horizontal distance of 17 km between the A2 and C2 moorings. The semi-diurnal tide is indeed weaker at 620 m at the C2 mooring (Fig. 2.4b), and stronger higher in the water column at 420 m.

(a)

(b)
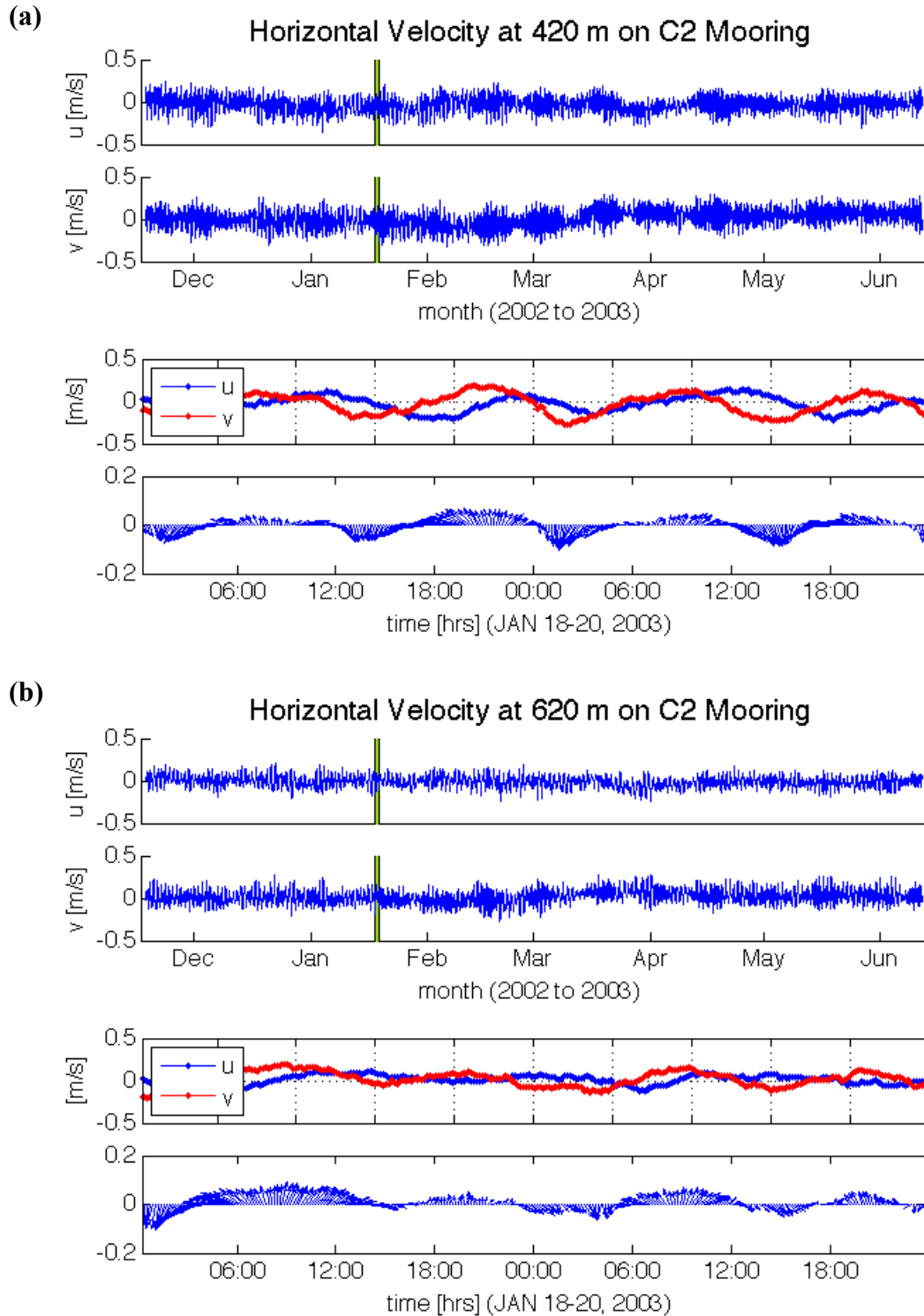
Figure 2.4 a-b) Horizontal current measurements from the HOME C2 mooring, averaged over 72 m and centered at **(a)** 420 m and **(b)** 620 m. At each depth, the top 2 panels show the full time-series, and the bottom 2 panels show two-day insets from January 18-20, 2003.

Depth-time maps of semi-diurnal velocity Power Spectral Density (PSD) from

Guiles (2009) show that semi-diurnal energy is concentrated in a beam-like manner in the

water column at the HOME A2 and C2 mooring locations (Fig. 2.5-6). Although the

variability in vertical extent and amplitude of each spring-neap cycle for the semi-diurnal

internal tide is large, there is clear upward propagation of the tidal beam with increased

distance from Kaena Ridge. The alignment of peak amplitudes from surface tides derived

from the altimetry-constrained global tide model TPXO6.2 (Egbert and Erofeeva, 2002)

with semi-diurnal horizontal currents provides further evidence that locally generated

internal tides are being observed.
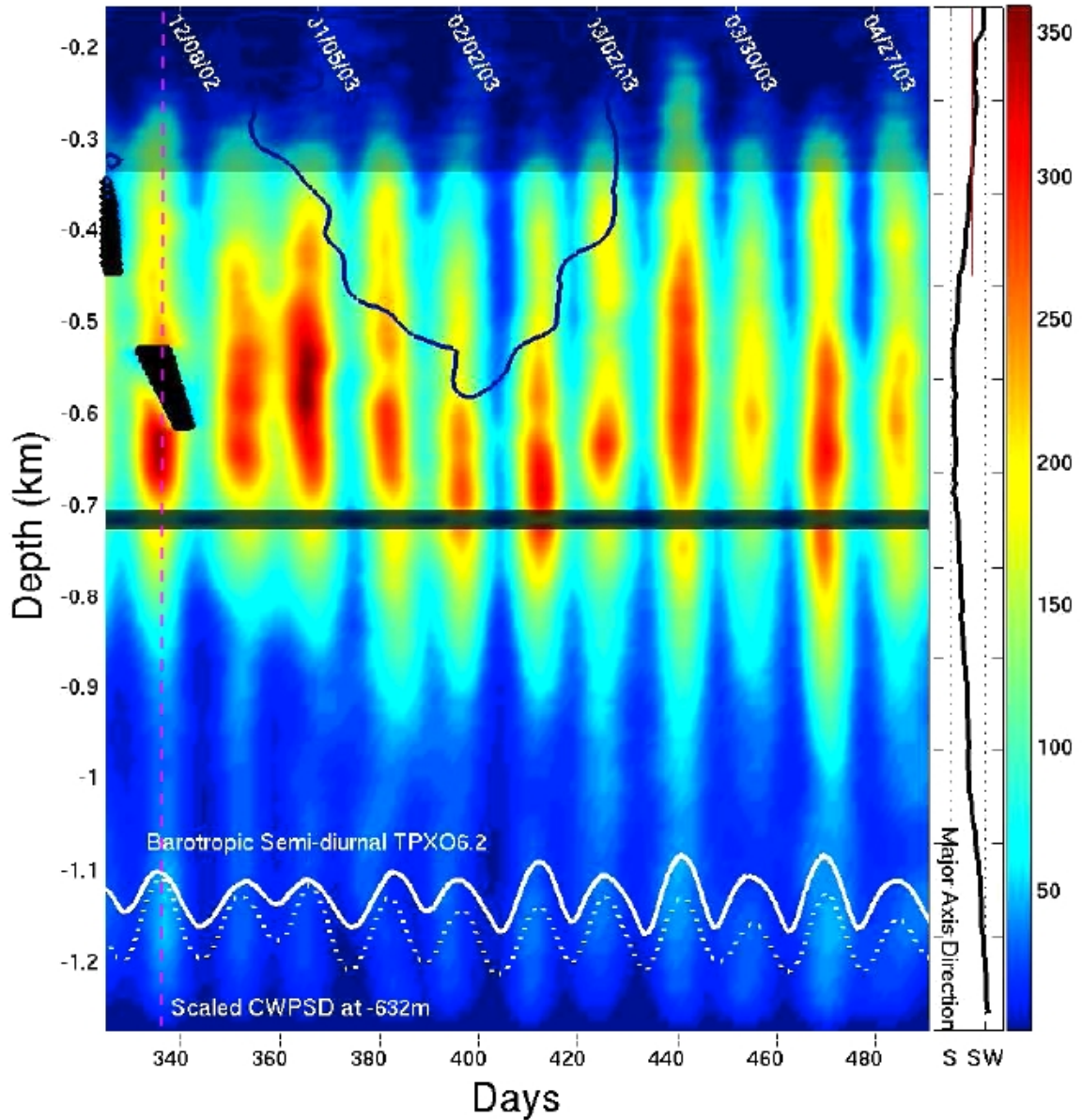
Figure 2.5 Depth-time map of horizontal velocity PSD [m² s⁻²/(rad/s)], band-passed for the semi-diurnal, for the HOME A2 mooring (shaded or blacked out regions indicate locations of poor ADCP data quality). Strong background flow is marked by the thin blue contour, where 15-day-averaged meridional velocity exceeds 5 cm/s in amplitude. Surface tide derived for this location (solid white line) and root-mean-squared time series of anti-cyclonic semi-diurnal horizontal current amplitude from 632 m (dotted white line) are aligned in peak amplitudes. Tidal ellipse major axis direction (right panel) are shown with scale lines at 180° and 225° (figure from Guiles, 2009, used with permission). Vertical dashed line indicates December 2, 2002, the beginning of the time-series considered in the present study.
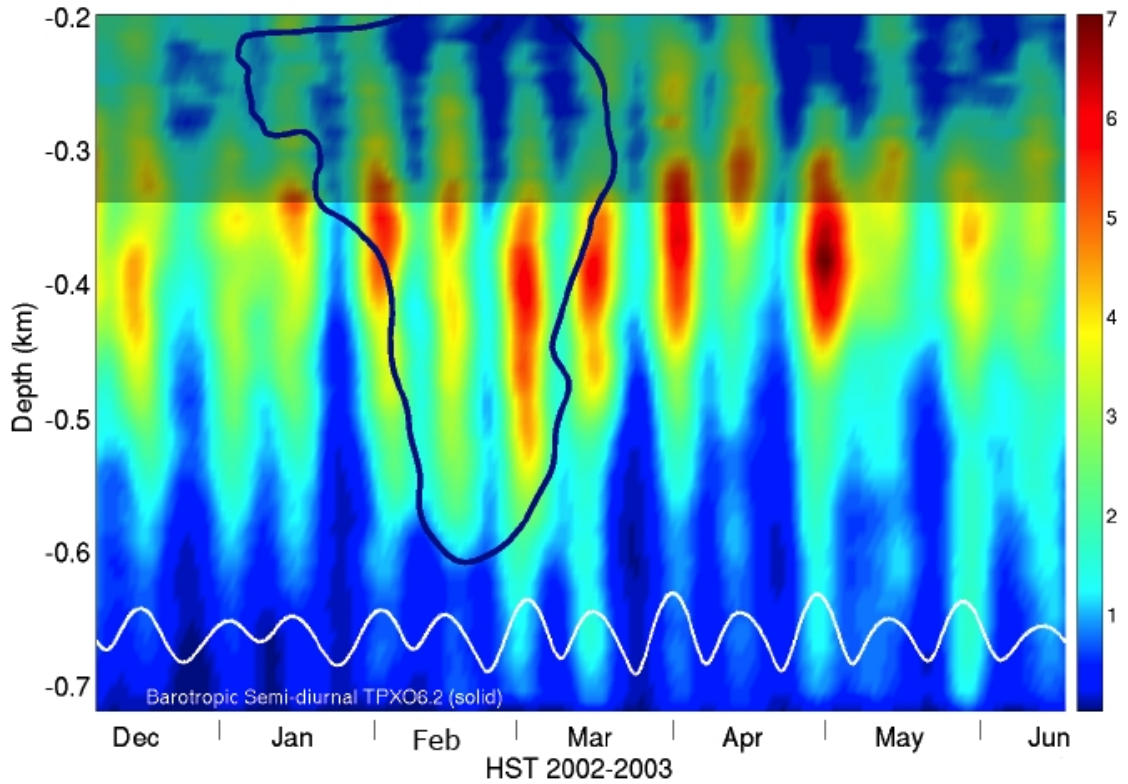
Figure 2.6 Depth-time map of semi-diurnal velocity PSD [m² s⁻²/(rad/s)] (sum of cyclonic and anti-cyclonic components) for the HOME C2 mooring (shaded region indicates poor ADCP data quality); surface tide derived for this location (solid white line). Strong background flow is marked by the thin blue contour, where 15-day-averaged meridional velocity exceeds 5 cm/s in amplitude (figure from M. Guiles, used with permission).

b. Diurnal Internal tides

The M_2 subharmonic is bracketed by, and extremely close in frequency to the principal diurnal tidal constituents O_1 and K_1 (df ~ 0.037 cpd) (Table 1.2). A depth-time map of diurnal velocity PSD for the HOME A2 mooring (Fig. 2.7) shows that overall diurnal energy is concentrated in a beam-like manner, with large temporal and spatial variability. The depths of maximal amplitudes for diurnal velocity PSD are lower in the water column than for semi-diurnal velocity PSD, consistent with equation (3), given a ridge crest source, and what is expected of internal tides at this location from numerical models, as well as the observations by Rainville and Pinkel (2006) in the HOME Nearfield (Fig. 2.8). Additionally, observations of K_1 currents at the A2 and C2 mooring locations are consistent with model prediction of locally generated K_1 internal tide (Fig. 2.9).

Although there was suggestive evidence in the HOME Farfield (430 km offshore to the southwest of Kaena Ridge) that diurnal baroclinic currents were in phase with semi-diurnal and not diurnal barotropic tides (Rainville and Pinkel, 2006a), at the A2 mooring location and with a much longer record, the peak amplitudes in diurnal baroclinic currents do appear to be aligned with peak amplitudes in the diurnal barotropic tide. With respect to horizontal baroclinic currents, amplitude maxima in diurnal and semi-diurnal velocity PSD occur at different times and depths (Fig. 2.6-2.7), suggesting that sustained non-linear interactions between the diurnal and semi-diurnal bands are unlikely.
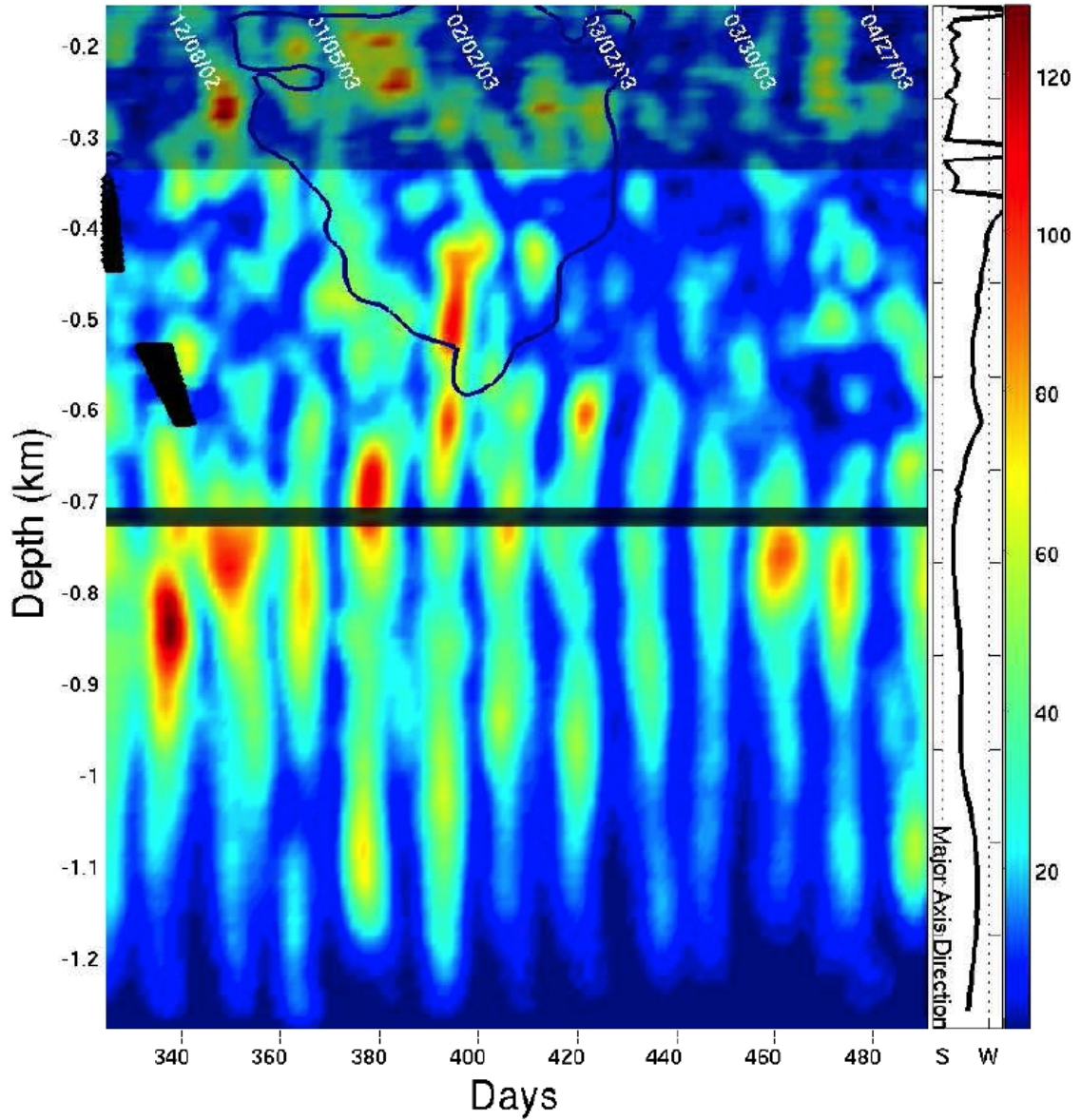
**Figure 2.7** Depth-time map of the diurnal band velocity PSD [m^2 s^{-2}/(rad/s)] (sum of cyclonic and anti-cyclonic components) for the HOME A2 mooring (ADCP data of poor quality are shaded or blacked out). Strong background flow is marked by the thin blue contour, where 15-day-averaged meridional velocity exceeds 5 cm/s in amplitude. Tidal ellipse major axis direction (right panel) are shown with scale lines at 180° and 225° (figure from Guiles, 2009, used with permission).
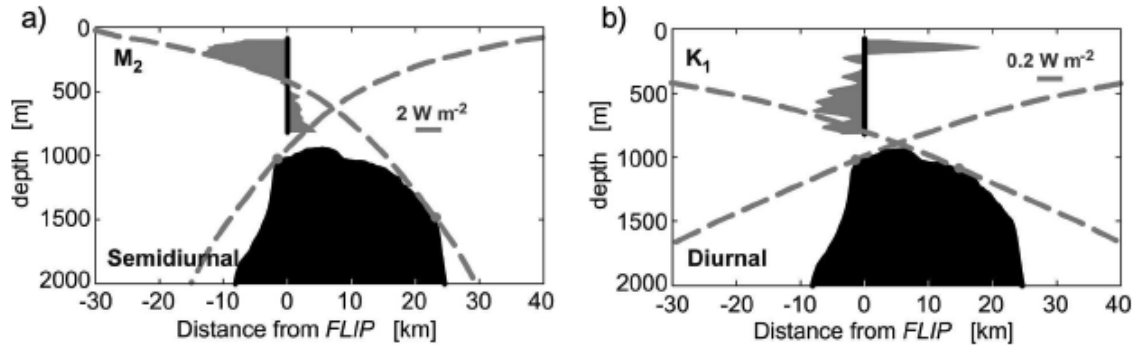
Figure 2.8 Cross-ridge profiles of energy flux in the HOME Nearfield location for
(a) semi-diurnal and **(b)** diurnal bands show the smaller vertical-scale of diurnal internal
tides. Topography is shown in black, and rays of propagating paths of M_2 and K_1 internal
tides are shown as dashed lines (figure from Rainville and Pinkel, 2006a, © American
Meteorological Society, used with permission).
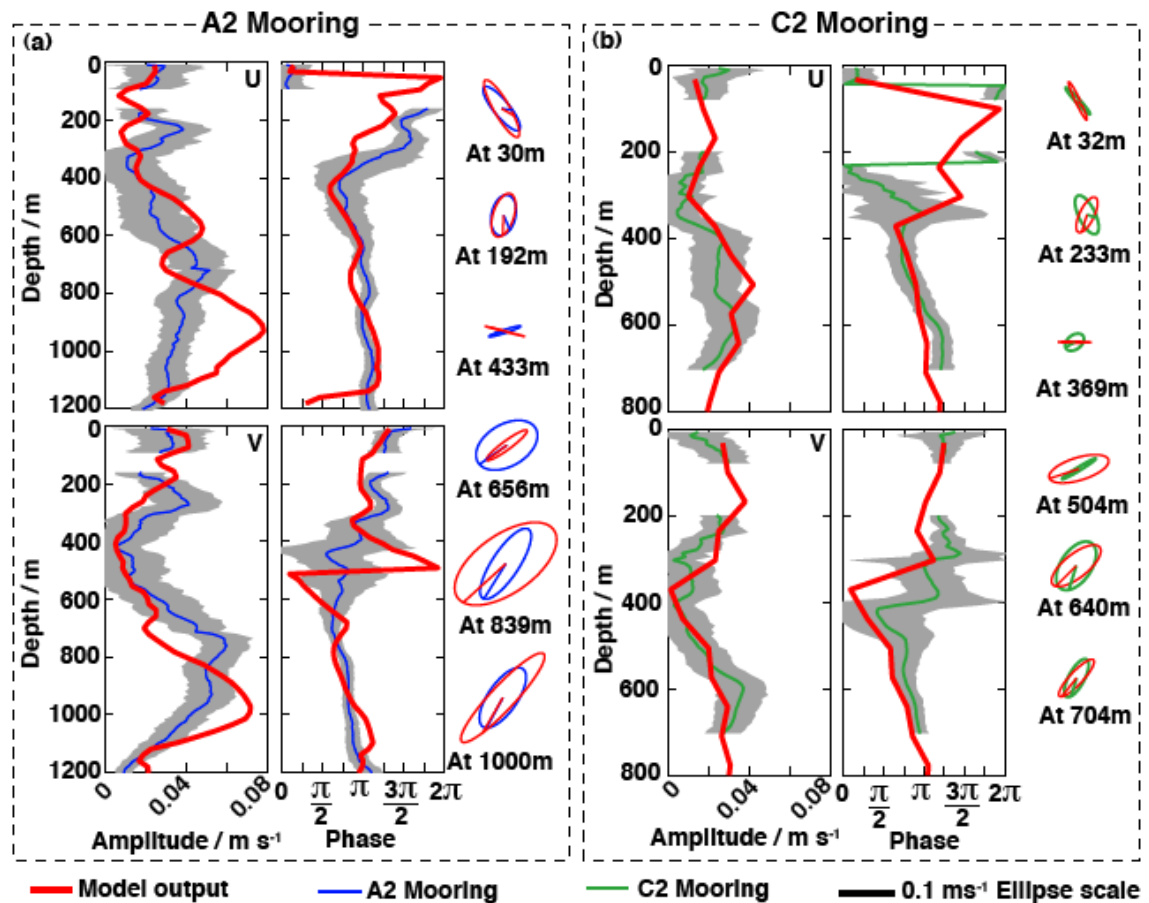
Figure 2.9 Observed phase and amplitude of K_1 horizontal velocities at the HOME A2
(a) and C2 **(b)** mooring locations are consistent with model output (figure from G.
Carter, used with permission).

3. METHODS

3.1 Estimating Vertical Shear

Available current measurements are binned at 8 m intervals and span 872 m in the vertical on the HOME A2 mooring. By examining velocity and small vertical-scale shear fields in the frequency domain, information can be gathered about how energy is distributed at the largest and smallest resolvable vertical scales, due to the vertical-shear spectrum being weighted towards larger wave-numbers when compared with the horizontal velocity spectrum. Vertical shear is calculated by taking the difference between adjacent velocity bins and interpolating using the Piecewise Cubic Hermite Interpolating Polynomial (PCHIP) function in MATLAB (Fig. 3.1). Depth interpolation allows for comparison between velocity and shear at the same levels, and PCHIP was chosen over a linear interpolation scheme to minimize error at the boundaries of the depth ranges being considered. The inclusion of spectra which might be influenced by edge-effects will be explicitly noted.

Figure 3.1. Snapshot of zonal velocity **(left)** and 8-m vertical shear **(right)** at 6 a.m. on January 19, 2003, from the HOME A2 mooring upper ADCP.

3.2 Modeling Barotropic Tide

In order to focus on internal wave interactions, estimated barotropic tide currents at the mooring locations are subtracted out from current measurements (Fig. 3.2). The Oregon State University tidal inversion software 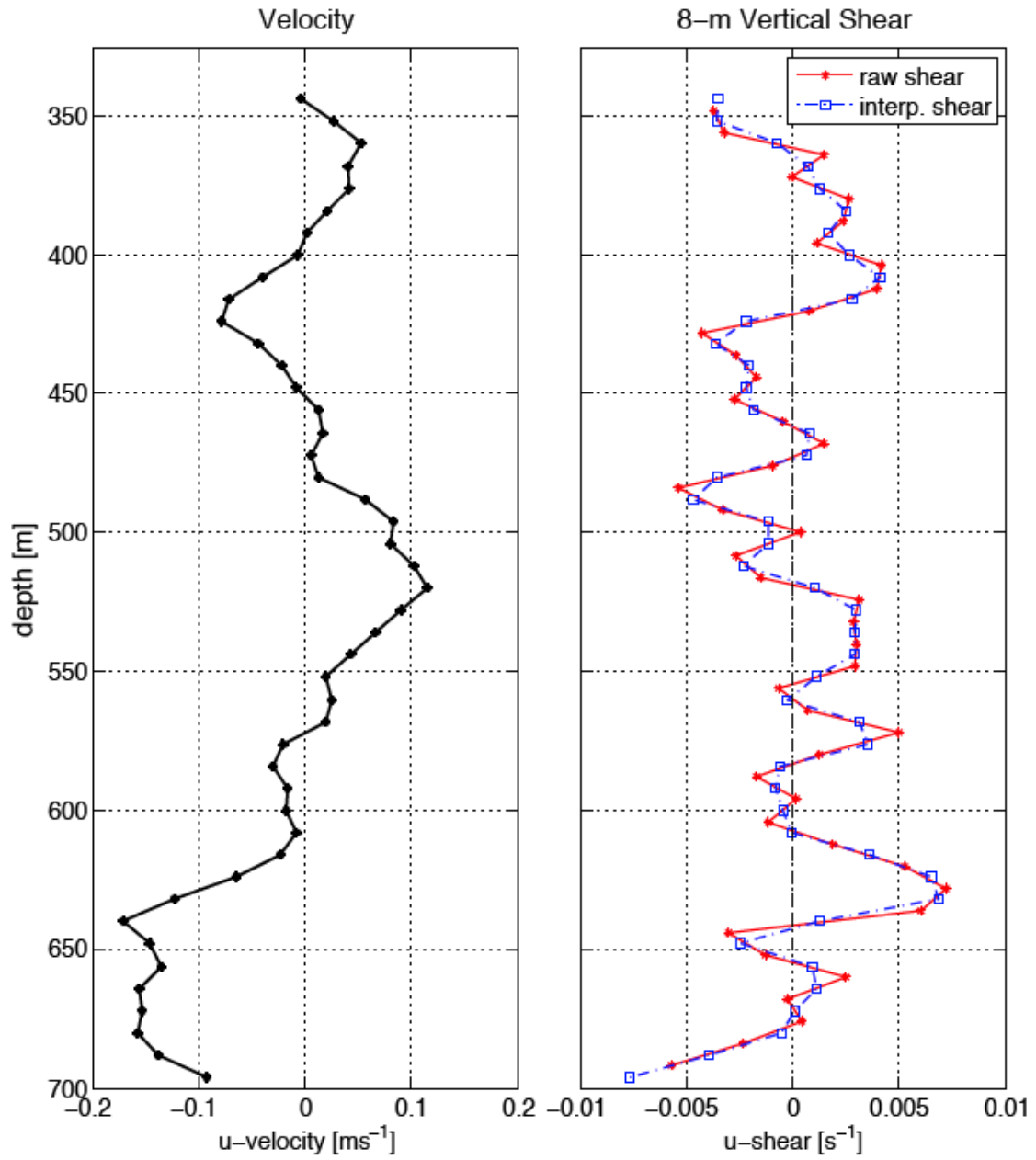(OTIS; Egbert and Erofeeva, 2002) has been widely used in studies of the Hawaiian Ridge (Zaron and Egbert, 2006; Zilberman et al., 2011; Pickering and Alford, 2012; Powell et al., 2012). The most up to date OTIS Regional Tidal Solution for the Kauai Channel is *Hawaii, 2010*[5], with eight primary (semi-diurnal, or D_2: M_2, S_2, N_2, K_2; diurnal, or D_1: K_1, O_1, P_1, Q_1) and two long period (Mf and Mm) harmonic constituents on a 1/60 degree resolution grid. The domain is approximately 18-26° N, 192-207° E, with boundary conditions provided by the OTIS global model TPXO 7.2. Barotropic tide solutions from *Hawaii, 2010* for the diurnal and semi-diurnal bands and for the M_2 tide at the A2 and C2 mooring locations (Fig. 3.3) are consistent with current observations at these locations.

To our knowledge, there has not been adequate study of the vertical structure of the barotropic tide in the presence of variable stratification and topography for the prediction of vertical barotropic current structure, especially in regions of internal tide generation. A numerical study of barotropic tidal flow over a continental slope (Holloway and Barnes, 1998) found that at a constant depth of 100 m and with constant stratification ($N = 0.016$ s^{-1}), a 10-15 m boundary layer occurs, with little or no shear in the barotropic current above the boundary layer. Without stratification the boundary layer was found to be much thicker, extending tens of meters. Although it is a crude approximation, for the purpose of

---

5   The model is available for download on the web at http://volkov.oce.orst.edu/tides/haw.html.

this study the barotropic tide will be assumed to be depth independent above 1250 m at

the HOME A2 mooring location.
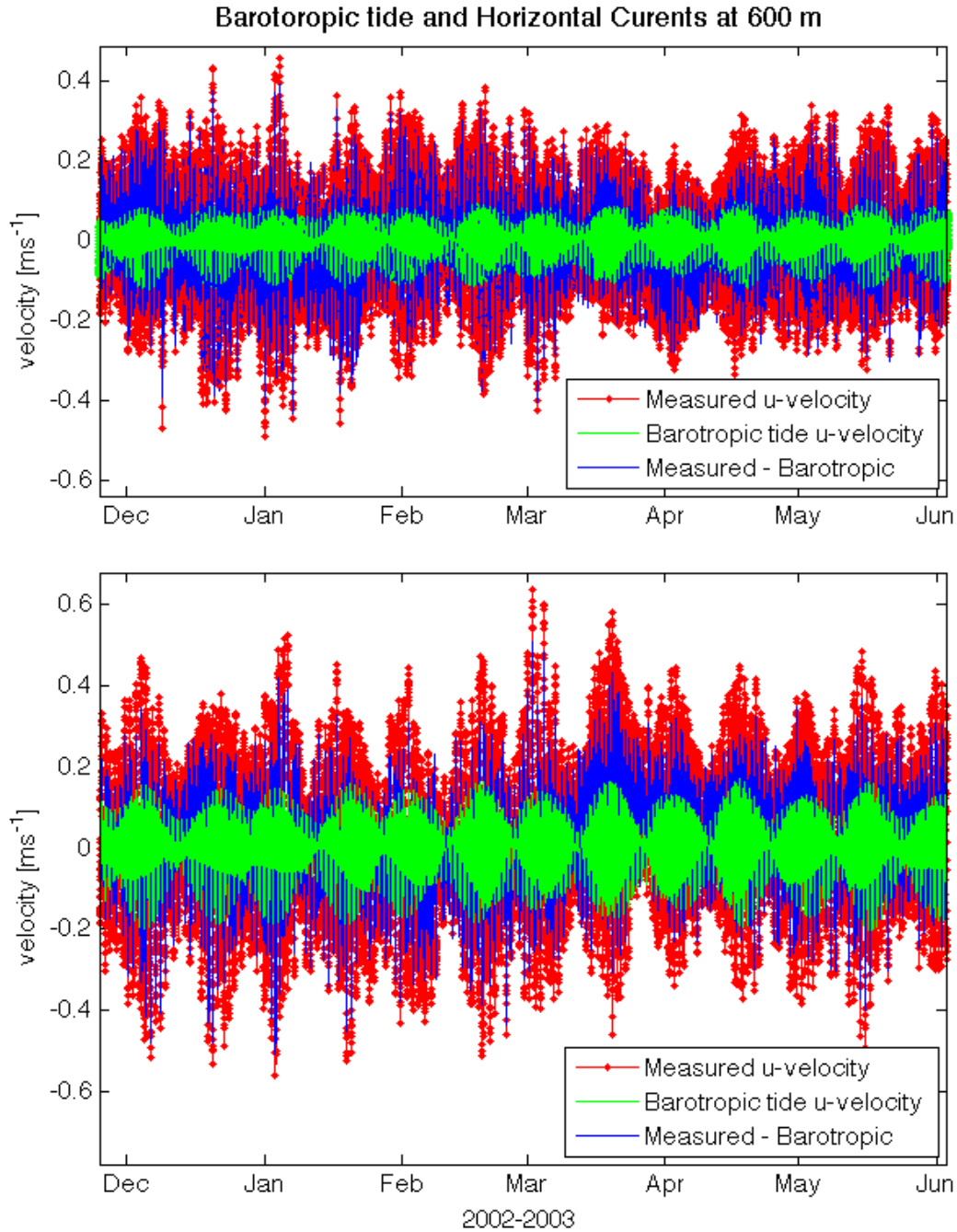
Figure 3.2 Time-series of depth-binned horizontal currents (red) at 600 m from the HOME A2 mooring are shown with *Hawaii 2010* predictions of barotropic tidal currents (green) and the estimate of baroclinic horizontal velocities (blue) obtained by subtracting barotropic tide predictions from the measured currents.
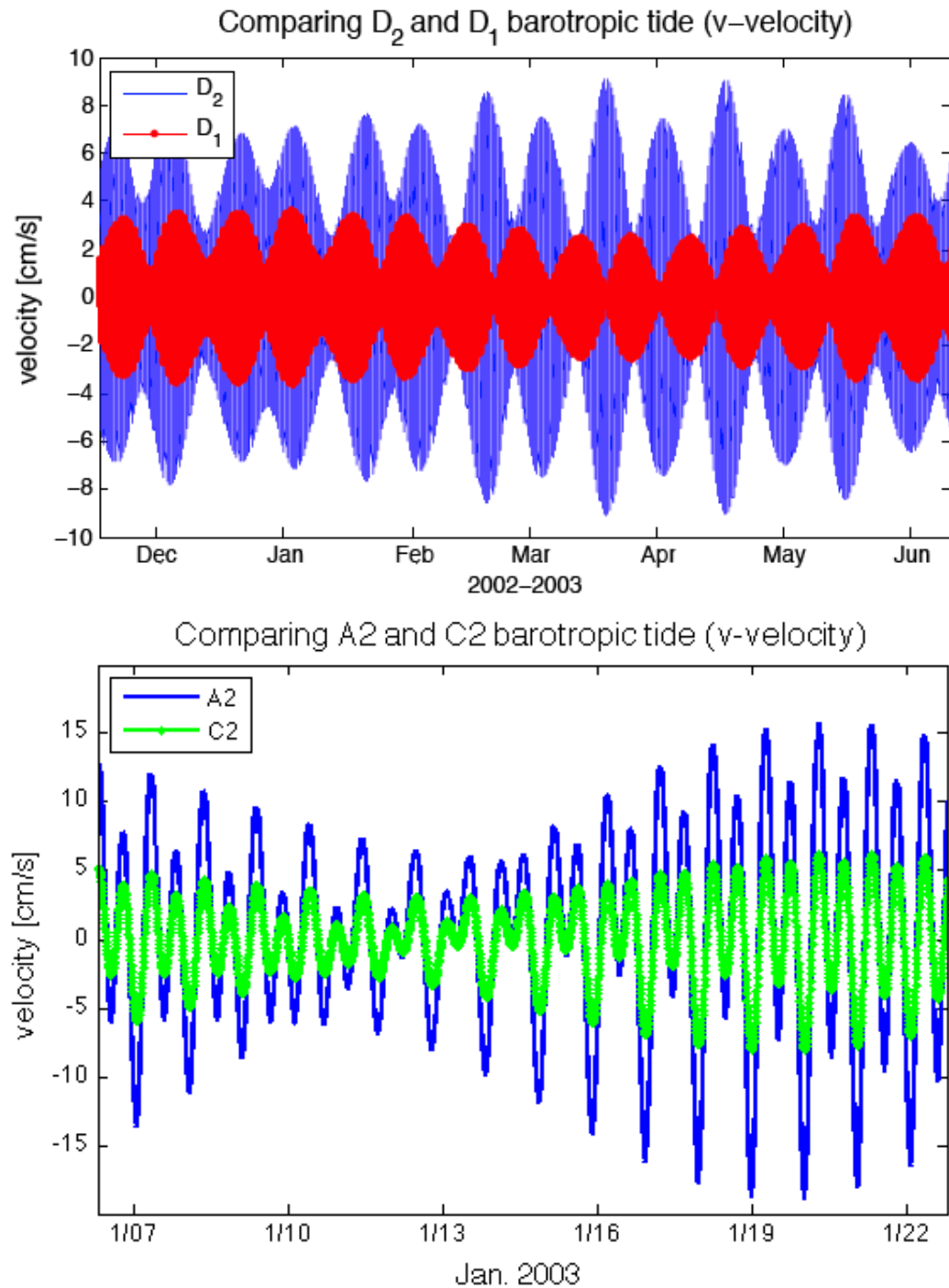
Figure 3.3 Barotropic tide predictions (meridional component only) for the HOME A2 mooring location **(top)** show that diurnal and semi-diurnal spring-neap cycles go in and out of phase, with the diurnal spring-neap cycle having a slightly shorter period; comparison of predictions for the HOME A2 mooring (blue) and C2 mooring (green) locations shows that amplitude changes appreciably but phase does not **(bottom)**.

3.3 Frequency Spectral Analysis

The primary goal of this project is to quantify the spectral energy at M_1, as distinct from energy at O_1 and K_1. Frequency spectral analysis is used due to the long dataset available for this study.

a. Discrete Fourier Transform (DFT) Harmonics

Not counting the zero-frequency, the gravest mode of a DFT is equal to the reciprocal of the data length ($\omega_1 \sim 1/T$). Other harmonics will be integral multiples of the gravest mode ($\omega_n \sim n/T$), with the highest mode being equal to half the sampling frequency (or Nyquist frequency). In addition to minimizing the frequency separation between DFT harmonics, alignment of DFT harmonics with the frequencies of interest is another important aspect of producing reliable and well-resolved spectra. The focus of this study is on three different frequencies in the diurnal band (O_1, M_1 and K_1), and the data lengths which have the least misalignment of DFT harmonics are numerically determined. Specifically, the optimal data length T can be described by:

$$\frac{p}{T} = O_1, \ \frac{q}{T} = M_1, \ \frac{r}{T} = K_1 \tag{4}$$

where *p, q* and *r* are as close to integers as possible. The error from misalignment of DFT harmonics is defined here as the root mean square of the differences between the frequencies of interest and their nearest Fourier Transform harmonic. Table 3.1 shows the 6 available record lengths which optimize the alignment of DFT harmonics with frequencies of interest in the diurnal band (Fig. 3.4). The data length of 163.5 days was

chosen over the longer available data length[6] mainly to facilitate comparison between all

three ADCPs available for this study (one of which has less than 191 days of data).

Data length (days)	Spectral points between O_1 (or K_1) and M_1	Root Mean Square Error (x10^{-3})
54.9	1	0.2016
81.8	2	0.1262
109.7	3	0.1210
136.6	4	0.0293
163.5	5	0.0766
191.5	6	0.0449

Table 3.1 Optimal data lengths for aligning Fourier Transform harmonics with O_1, K_1, and M_1 were determined numerically. The highlighted data length is used in this study.
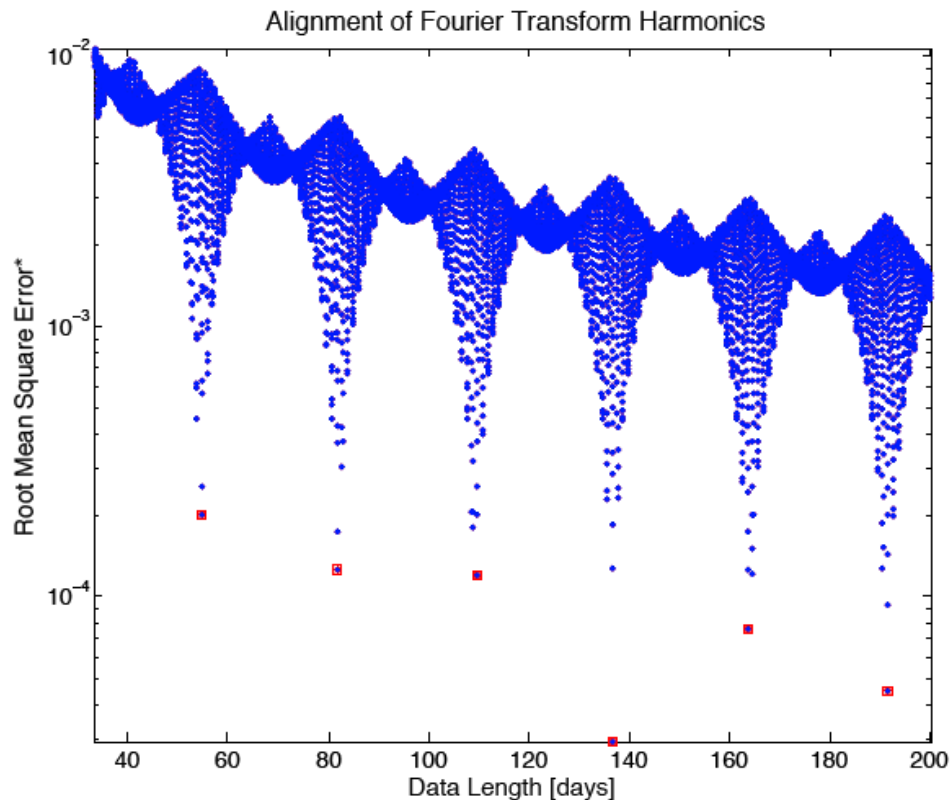
Figure 3.4 The root mean square error due to misalignment of DFT harmonics with the frequencies O_1, K_1, and M_1 reaches local minima for select data lengths (red squares).

---

6   Data length of 136.6 days was also not used despite having the lowest RMS error; it is preferable to use the longer data length of 163.5 days due to the primary importance of frequency resolution.

b. Data windows

When estimating the frequency spectrum of an infinite series from a finite record

length, energy at frequencies other than the Fourier harmonics is spread over a range of

frequencies; this is called "spectral leakage". The 10% tapered-cosine window (Fig. 3.5)

is used for its performance in reducing leakage and noise while maintaining a sharp peak

at the center frequency. The effects of data truncation and window tapering are illustrated

for a velocity time-series from the A2 upper ADCP (Fig. 3.6). The maximum overlap

between the three ADCPs is 181.5 days, and the 163.5 days segment used in the

frequency analysis was chosen to minimize the effect of ADCP problems on the A2

mooring during the first ~20 days of deployment (discussed in Chapter 2).
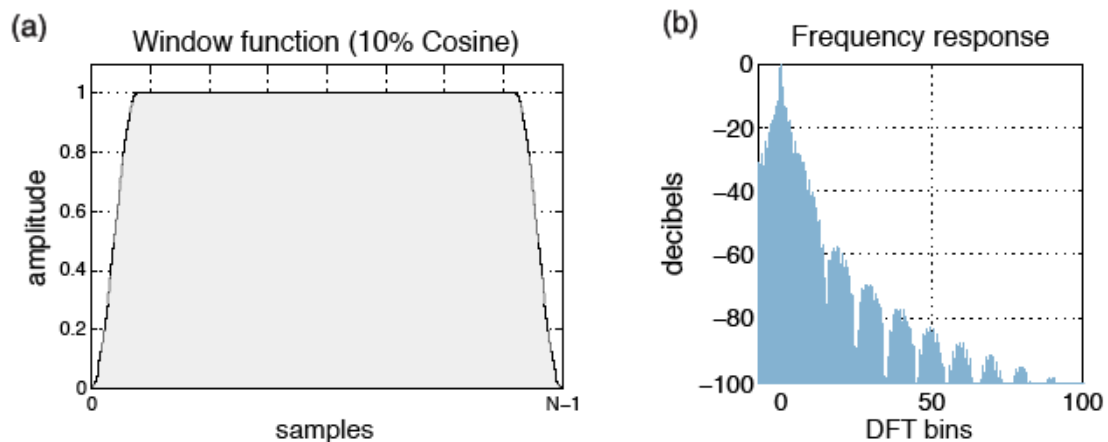
Figure 3.5 a) A constant function (of amplitude one) multiplied with the tapered-cosine window; **b)** the frequency response of the cosine window taper shows the central lobe at zero frequency, but also some "leakage" of energy to other DFT bins, falling off with distance from the central lobe.
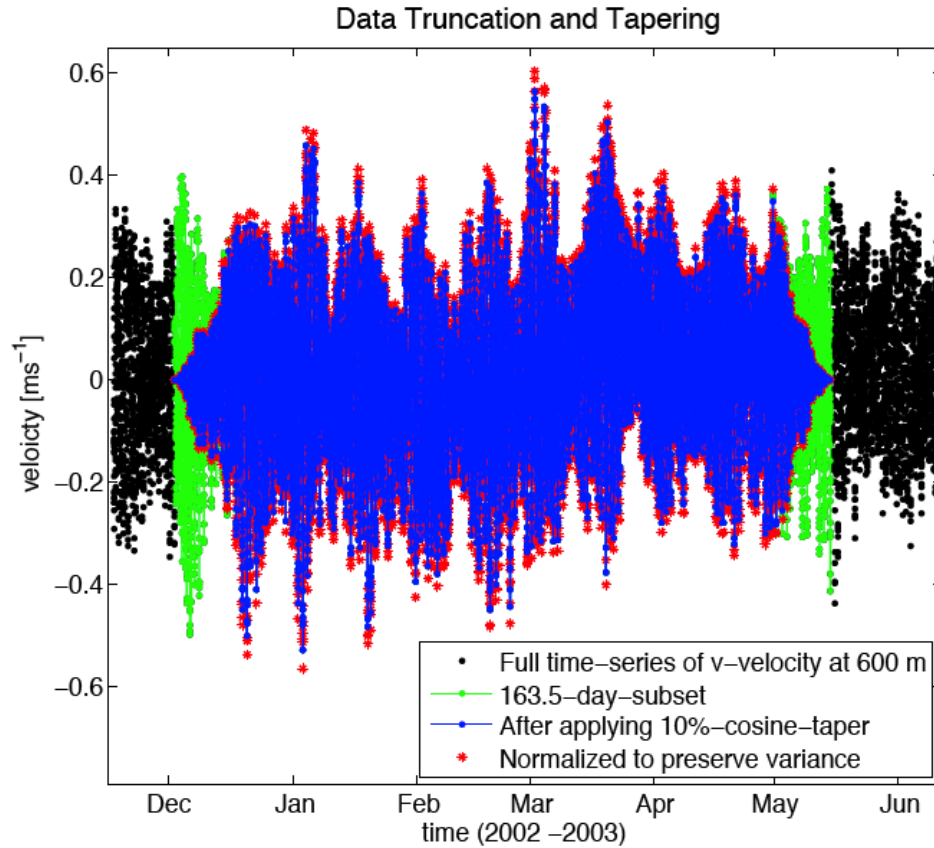
Figure 3.6 The result of data truncation and data-window tapering is shown for a meridional velocity time-series at 600 m on the HOME A2 mooring.

c. Rotary spectra

Rotational properties of the current field of internal waves have been investigated analytically and empirically (Müller et al., 1978), and it is useful to decompose horizontal current vectors into oppositely rotating components before examining their spectral content. To compute rotary spectra, DFT is performed on the complex variables $U = u + iv$ (horizontal velocity) and $\partial U / \partial z$ (vertical shear). Zonal and meridional velocity components are assumed to be independent in the sense that each spectral estimate of U and $\partial U / \partial z$ have two degrees of freedom and the positive frequency coefficients

(representing the cyclonic component) are independent from the negative frequency (anti-cyclonic) coefficients.

d. Spectral averaging

Each spectral estimator is a chi-squared function with only two degrees of freedom, and averaging is needed to increase the statistical reliability of a given spectral estimate (Emery and Thomson, 2004). Resolving the diurnal band is a central purpose of this study, and preserving high frequency resolution is a priority. Frequency-band averaging will be minimal (3 points), and depth-averaging will be over 10 ADCP depth-bins (80 m), when applicable. Ensemble or block-averaging (splitting the time-series into segments and averaging the resultant spectra) will not be applied.

With frequency-band averaging, adjacent spectral estimates are averaged together to increase the statistical reliability of the result, at the cost of losing resolution (Fig. 3.7). The spectrum is said to be "smoothed" by a window whose span is the number of estimates in an average. Although not necessary, odd number window spans are useful in that the center point is easily defined. To further increase the statistical reliability of PSD estimates, spectra calculated from different bins of ADCP data are averaged together. Spectral estimates from each depth bin are not necessarily independent from those of neighboring bins, and increases in degrees of freedom (DOF) from vertical-averaging is estimated by defining vertical coherence lengths separately for the horizontal velocity and vertical shear fields. In averaging together ten ADCP depth-bins, the DOF for shear spectral estimates are increased by a factor of 2.8, whereas there is no increase in the DOF for velocity spectral estimates (for details please see Appendix A).
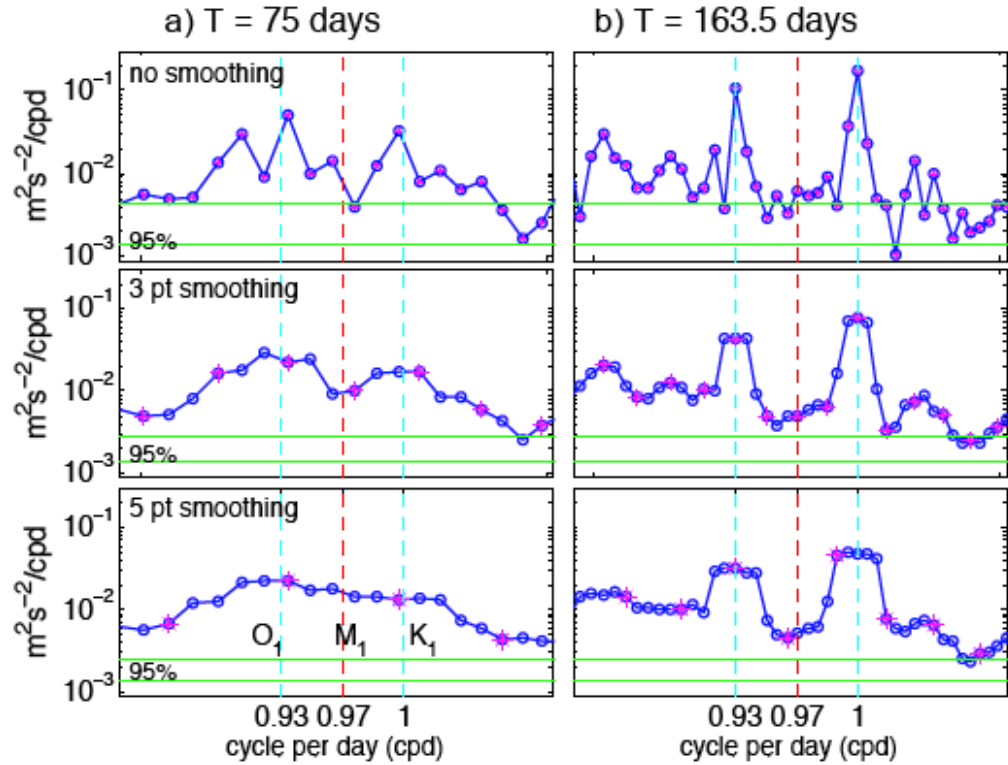
Figure 3.7 Frequency spectra calculated from **a)** 75 days and **b)** 163.5 days of A2 mooring velocity data, with no frequency smoothing **(top)**, 3-point smoothing **(middle)**, and 5-point smoothing **(bottom)**. The 95% confidence intervals (green lines) for independent points (pink markers) are smaller for larger window spans.

In order to compare power spectral densities across different depths, it is important to note the dependence of internal wave properties on the buoyancy frequency. Since normalized horizontal velocity scales as $N^{-1/2}$ (Leaman and Sanford, 1975), velocity PSD will scale as N^{-1}. Vertical length-scales are also affected by N, so shear should scale as $N^{-3/2}$ and shear PSD as N^{-3}. The stratification profile used in this study (Fig. 3.8) was calculated using the SeaWater MATLAB library written by Phil Morgan and Lindsay Pender of CSIRO Marine Research, using data collected from December 21, 2002 to April 26, 2003 at Station Kaena.
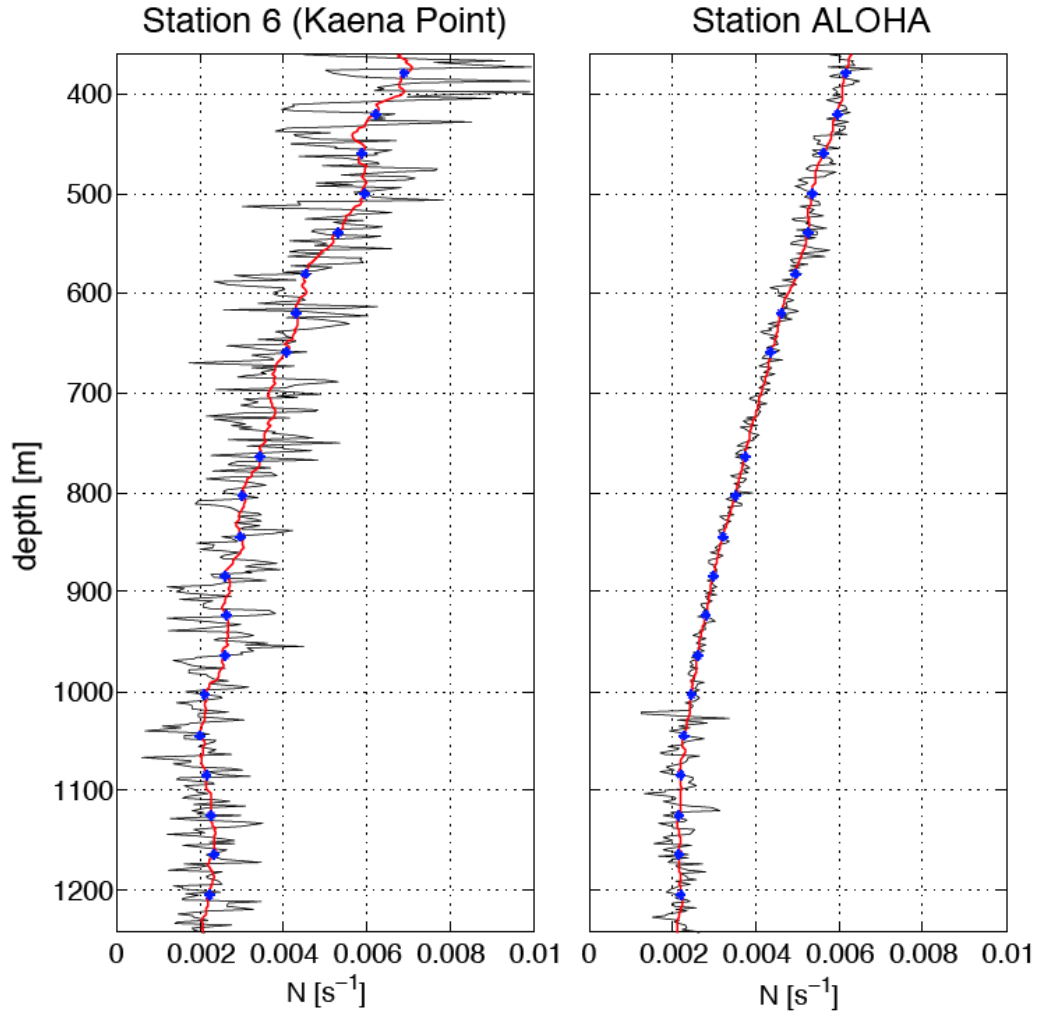
Figure 3.8 The buoyancy frequency N is calculated with salinity and temperature data from Station Kaena Point **(left)** and Station ALOHA **(right)**. The red curve is the square-root of the 70 m running average of N^2 calculated from 2-m resolution data (black) from the Hawaiian Ocean Time-series. Blue markers show the depths where 72 m vertical averaging was possible for the dataset under present study.

3.4 Bispectral Analysis

Many observational studies investigating nonlinear interactions between the M_2 tide

and M_1 have utilized bispectral techniques in addition to auto-spectral analysis (Carter

and Gregg, 2006; Sun, 2010; Xie et al., 2011; Liao et al., 2012; MacKinnon et al., 2013a).

The basic formulation of bispectra $B(\omega_j, \omega_k)$ and bicoherence $b(\omega_j, \omega_k)$ is standard (Kim

and Powers, 1979; Elgar and Guza, 1988):

$$B(\omega_j, \omega_k) := E\left[X_1(\omega_j)\, X_2(\omega_k)\, X_3{}^*(\omega_j + \omega_k)\right] \tag{5}$$

$$b(\omega_j, \omega_k) := \frac{\left|B(\omega_j, \omega_k)\right|}{\left(E\left[\left|X_1(\omega_j)X_2(\omega_k)\right|^2\right] E\left[\left|X_3(\omega_j + \omega_k)\right|^2\right]\right)^{1/2}} \tag{6}$$

where $X_i(\omega)$ are complex Fourier transform coefficients for stationary random processes

(* denotes complex conjugate, and $E[\ ]$ is the expected value). Calculations of

significance levels for bicoherence are often based on the DOF in each expected value

(estimated through frequency-averaging or ensemble-averaging).

The rotary bispectrum is a special case of just one vector process represented by its

rotary components (Yao et al., 1975). Fourier transform coefficients are calculated as

described in the previous section on auto-spectral analysis, except that a simple

rectangular window will be used instead of the tapered cosine window. The conditions for

resonant non-linear wave-wave interactions involving the M_2 tide as the large-scale

primary wave and two small-scale secondary waves with M_1 frequencies can potentially

occur for four distinct frequency triplets (Table 3.2).

	ω_1	ω_2	$\omega_3 = \omega_1 + \omega_2$
A	$+M_2$	$-M_1$	$+M_1$
B	$+M_1$	$-M_2$	$-M_1$
C	$-M_1$	$-M_1$	$-M_2$
D	$+M_1$	$+M_1$	$+M_2$

Table 3.2 Frequency triplets which could potentially fulfill resonance conditions for M_2 and M_1 waves.

A basic assumption of bispectral analysis is that the processes under study are stationary and random (Yao et al., 1975; Kim and Powers, 1979; Elgar and Guza, 1988), and it is unclear how the technique can be properly applied to nearly deterministic signals such as the tides. Various significance tests are essential to the reliability of bispectral analysis[7] (Yao, 1974), although it is beyond the scope of this study to carry out such tests. Instead, we first apply bispectral techniques to analyze a synthetic dataset containing only linear sinusoidal (deterministic) inputs[8] and white Gaussian noise (obtained from M. Guiles, personal communication). Expectation values are calculated by taking a weighted sum in 2-dimensional frequency space and then averaging in depth. The 5x5 Gaussian window used for the weighted sum (Fig. 3.9) is the matrix product of column vector W with its transpose, where

$$W := e^{-x^2/2c^2} \tag{7}$$

for integers $-2 \le x \le 2$ and $c = 0.8$.

---

7   Yao (1974) offers a detailed discussion of these testing techniques and in it the author cautions that "in order to have valid result, all the interpretation and calculations should only be based on the rotary spectral parameters which have passed these tests".

8   Eight tidal frequencies (as described in section 3.2) are included, with the relative amplitudes set with reference to the TPXO6.2 tidal model. An idealized inertial-band is also included.
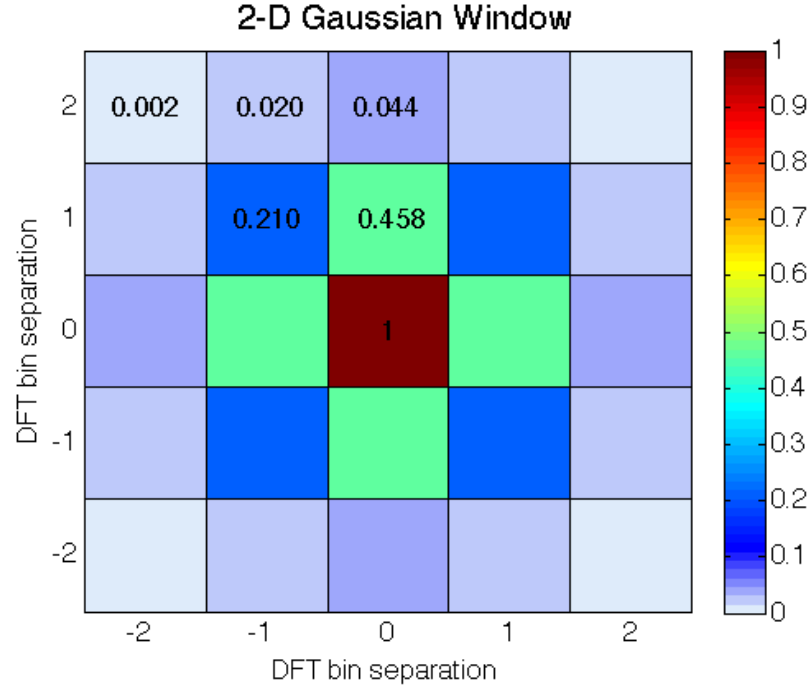
Figure 3.9 The expectation value for each frequency triplet is calculated by taking a weighted sum with the above 5x5 Gaussian window and then averaging in depth. The approximate increase in DOF from applying this Gaussian window filter is estimated as the sum of the weights in the matrix, or ~ 4.

For orientation, the full bispectrum is shown with the regions of interest bordered and labeled in red (Fig. 3.10). Frequency triplets will be described as (ω_j, ω_k, $\omega_j + \omega_k$), with the positive and negative signs of the frequencies denoting cyclonic and anti-cyclonic rotary components, respectively. Elevated bispectral values (at least one order of magnitude above the background) were found for various frequency triplets involving M_2, K_2, O_1, and K_1 (Fig. 3.11). Bicoherence levels that have been interpreted as indicating non-linear interactions are observed for this dataset (Fig. 3.12), even though there are no interactions between the signals in the synthetic dataset.
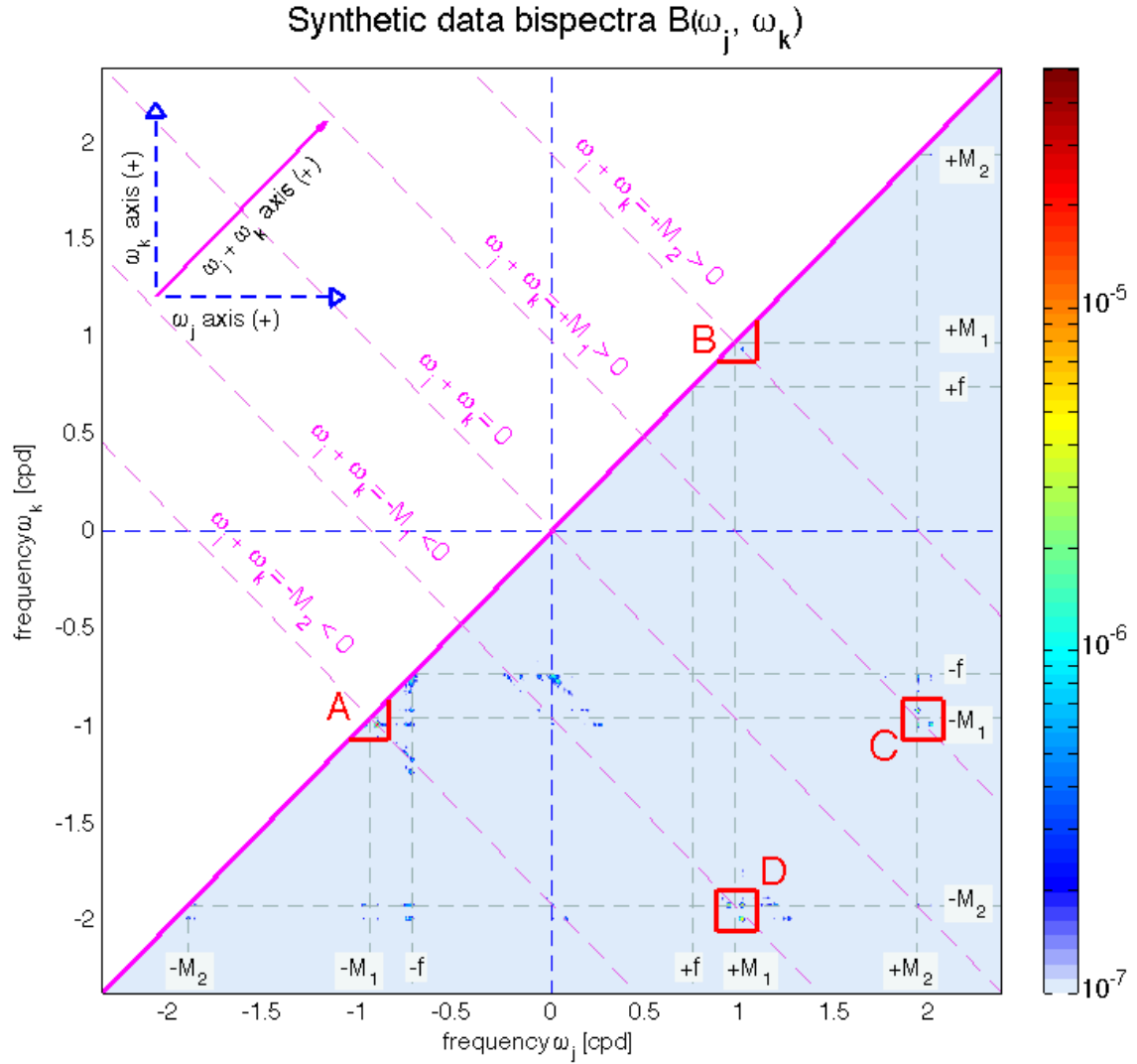
Figure 3.10 The bispectrum of a single process X (complex velocity $u+iv$) is symmetric across the $(\omega_j + \omega_k)$ axis (magenta) where $\omega_j = \omega_k$. Resonant triads involving M_2 and M_1 waves can occur for four distinct frequency triplets in regions A-D;
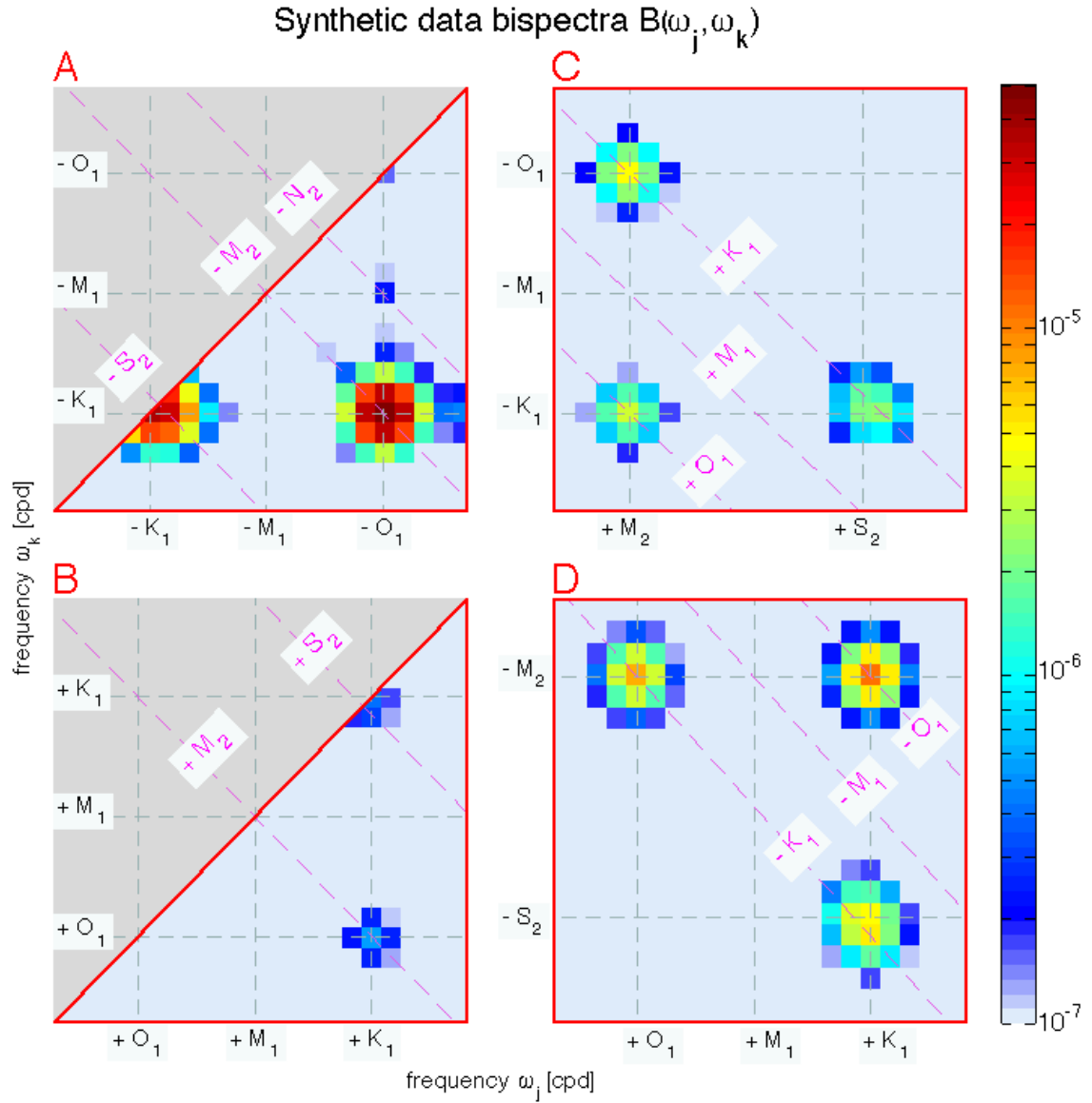
Figure 3.11 The four frequency triplets with the highest bispectral values occur in regions **A (top left):** $(-K_1, -K_1, -K_2)$, $(-O_1, -K_1, -M_2)$ and **D (bottom right):** $(+O_1, -M_2, -K_1)$, $(+K_1, -M_2, -O_1)$. The semi-diurnal tidal constituent K_2 (not plotted) has twice the frequency of K_1 and is less than 6×10^{-3} cpd from the frequency of S_2.
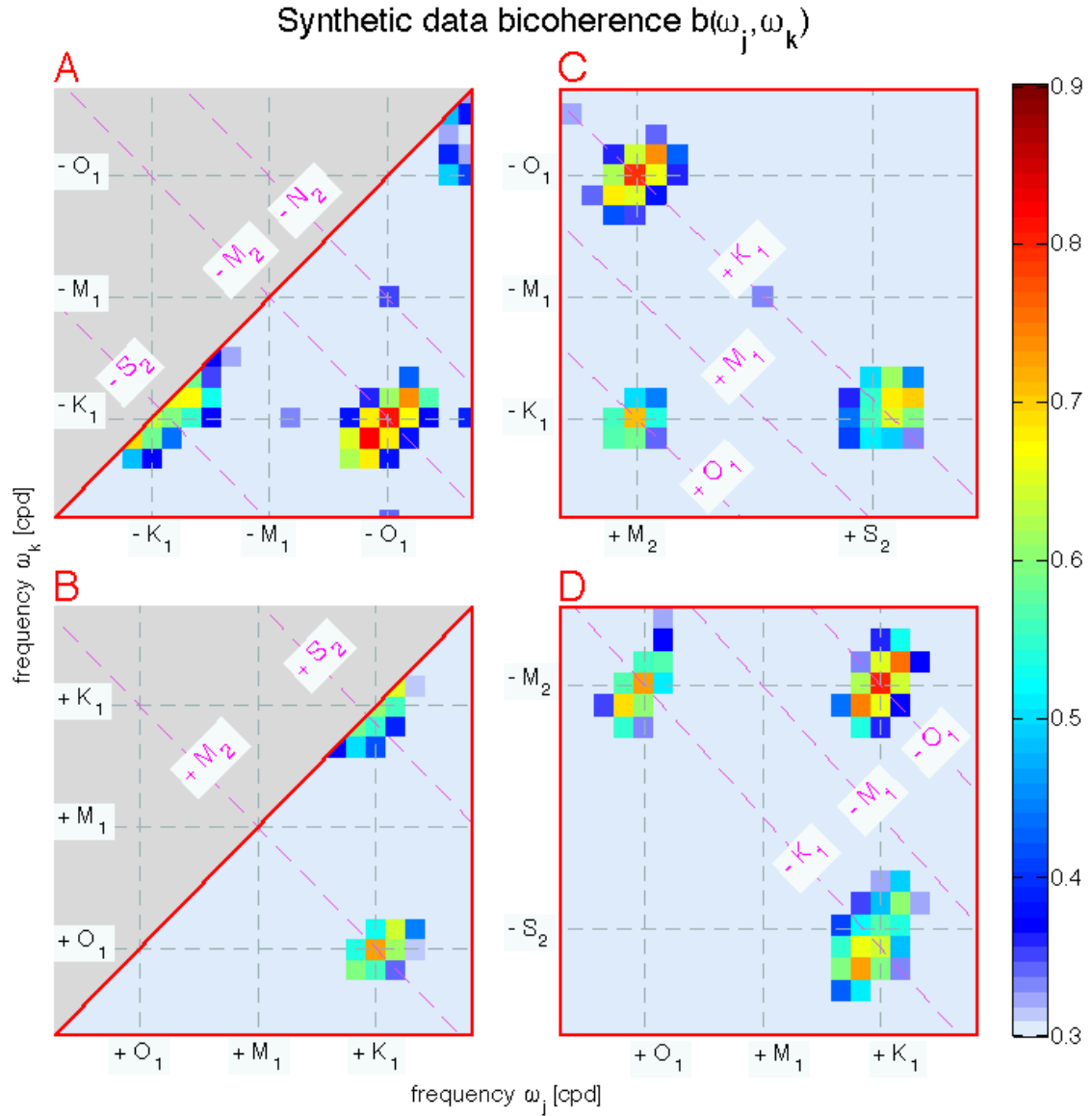
Figure 3.12 Bicoherence is normalized from 0 to 1, and significance levels are calculated following Elgar and Guza (1988). With approximately 8 DOF (4 from applying the Gaussian window filter), the 90% confidence level is ~ 0.76.

To our knowledge, the application of bispectral techniques to deterministic signals such as the coherent component of internal tides has not been thoroughly tested, and many issues remain about optimal methodology and interpretation of results. A few issues are especially relevant and worth noting:

1. The calculation of expectation values through frequency or ensemble-averaging,

 a. under what conditions are the two methods equivalent? Elgar and Guza (1988) show that there is convergence with increased DOF;

 b. what are the advantages and disadvantages of each method, in terms of data optimization and consideration of episodic events and low-frequency phenomena?

2. The estimation of degrees of freedom and bicoherence significance levels;

3. The appearance of strong bicoherence for triads which have no non-linear interaction.

Based on the literature (Table 3.3), expectations values are most often calculated by breaking up a time-series into multiple segments and ensemble-averaging. This has been done for short (~10 days) as well as long (> 8 months) datasets, at the cost of losing frequency resolution. In order to maintain frequency separation between M_1 and diurnal tidal constituents O_1 and K_1, expectation values for the present study will be calculated with a narrow-peak Gaussian window. Following Carter and Gregg (2006), horizontal velocity components are not considered independent DOF for bispectral analysis. Additional DOF from depth-averaging are calculated from estimates of vertical-coherence length-scale (described in Appendix A). Relevant parameters for bispectral analysis of the HOME A2 mooring dataset are summarized in Table 3.4.

	MacKinnon et al., 2013a	Liao et al., 2012	Carter and Gregg, 2006
Latitude	28.9ºN	20ºN	~21.65ºN
Depth ranges [m]	(400-750; 850-1250)	30-190	100-600
Total data length (T [days])	50	~263	10.95
Data windows (ΔT [days])	5; 50% overlapping	2; 50% overlapping	~2; non-uniform spacing
DFT variables	u_H (up, down), w	u and v, separately	u and v, averaged
DOF	120 (time: 20; depth: 3)	~104	10 (time: 5)
Confidence level	95%, $\sqrt{(6/DOF)} \sim 0.22$	90%, $\sqrt{(4.6/DOF)} \sim 0.21$	(90, 95)% : (0.68, 0.77)
Observed bicoherence	~0.54 depth-average	> 0.2 for diurnal band, from 50-100 m	> 0.6 for (0.98, 0.98) cpd, from 500-600 m
Pros/Cons	+ large vertical range + high resolution density + critical latitude, $f \approx M_1$ + mixing estimates	+ long time-series - small depth-range	- short, discontinuous T - location not fixed

Table 3.3 Comparison of representative studies which calculate bispectra and find significant bicoherence between the M_2 internal tide and waves of M_1 frequency.

	HOME A2 mooring (present study)
Latitude	21.75ºN
Depth ranges [m]	(344-704; 728-1288)
Total data length (T [days])	180-200
Data window (ΔT [days])	163.5
DFT variable	Complex velocity $u+iv$
DOF	8 (frequency-averaging: ~4)
Confidence level	(90, 95)% : (0.76, 0.87)
Pros/Cons	+ large vertical range and relatively long time-series - difficult to use semi-Lagrangian coordinates

Table 3.4 A summary of the HOME A2 mooring dataset and relevant parameters for bispectral analysis.

4. RESULTS

4.1 Spectral Energy of Velocity and Shear

Length of record in a time-series plays an essential role in determining the reliability of spectral analysis. Without sufficient record length and adequate frequency resolution, the entire diurnal band can appear as one broad (or "smeared") spectral peak centered on the M_2 subharmonic, M_1. Although the frequency resolution of a spectrum is often approximated as the reciprocal of record length (Emery and Thomson, 2004; Carter and Gregg, 2006), an exercise using simple sinusoids (Figures 1.2-3) showed that a longer record is required in practice. Based on the methods described in Chapter 3, velocity and shear power spectra were calculated using 163.5 days of depth-binned ADCP observations from HOME (described in Chapter 2).

Depth-frequency maps of velocity PSD (no depth-averaging) from both A2 and C2 moorings (Fig. 4.1) show distinct spectral peaks at semi-diurnal (M_2, S_2) and diurnal (O_1, K_1) tidal frequencies in both cyclonic and anti-cyclonic rotary components. For shear PSD (Fig. 4.2), spectral peaks at tidal frequencies are less clearly defined, but the anti-cyclonic components are still discernible, especially at the A2 mooring closer to the Ridge. The aspect ratio of internal waves decreases with frequency (with inertial motions being purely horizontal) and shear spectra, which are weighted towards smaller vertical scales, are dominated by strong near-inertial to diurnal-band energy. Spectral peaks at O_1 and K_1 are only clearly distinguishable below 1100 m at the A2 mooring location, where near-inertial energy approaches background levels. For increased statistical reliability, ten-bin depth-averages of frequency spectra will be examined (Figures 4.3-4).
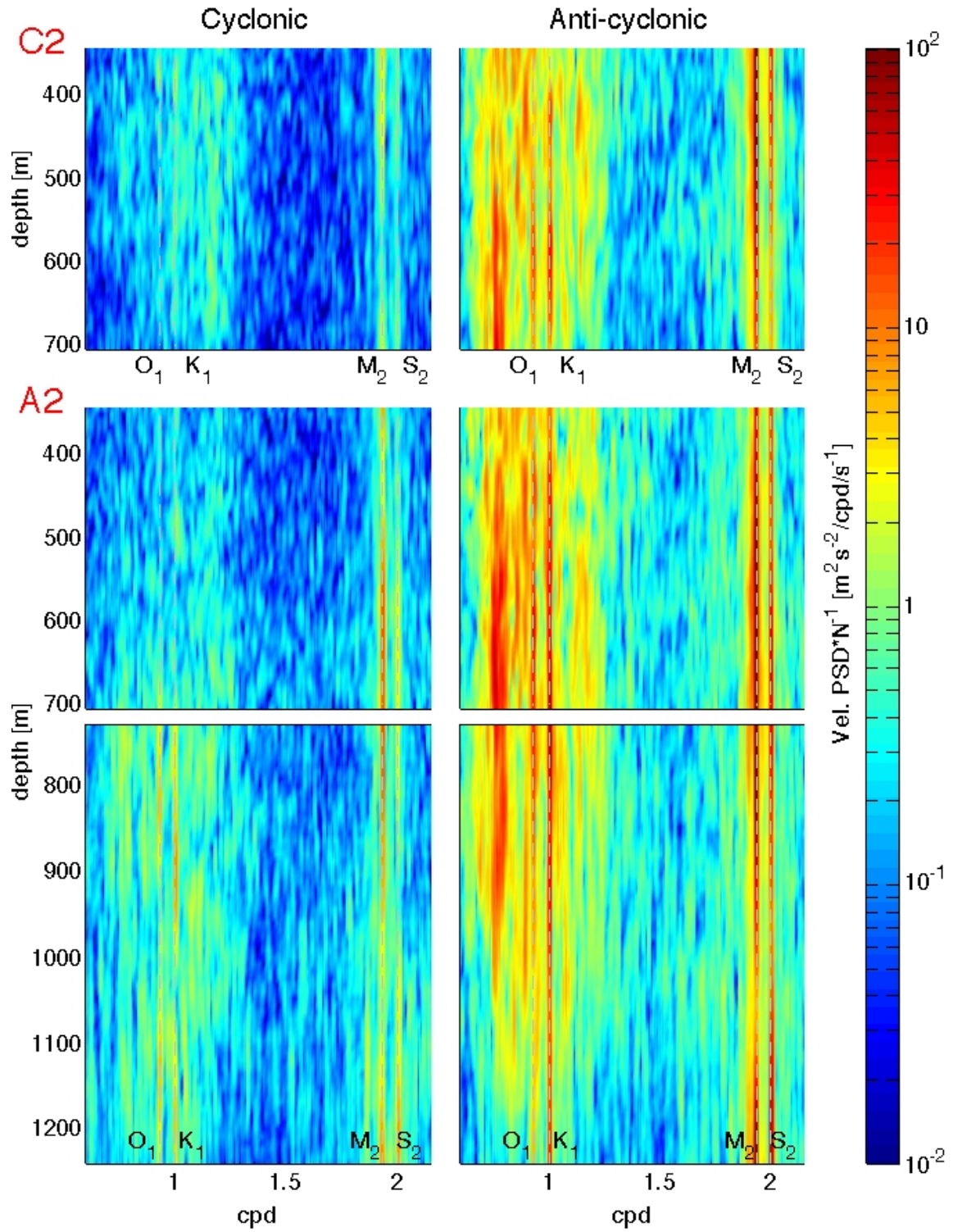
Figure 4.1 Velocity PSD (estimated barotropic tide currents have been subtracted from measured currents) from HOME moorings C2 **(upper panel)** and A2 **(lower two panels)**.
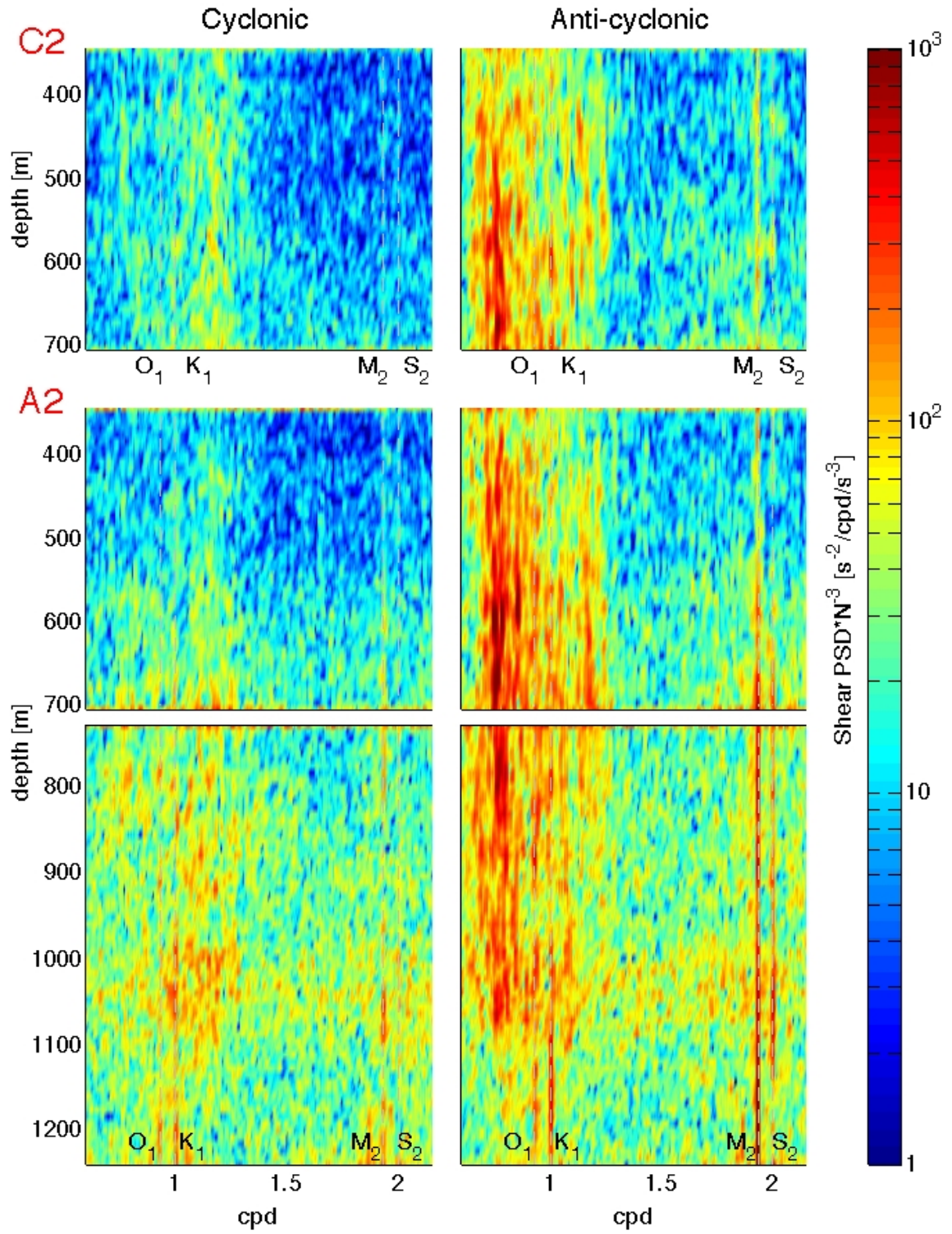
Figure 4.2 Shear PSD from HOME moorings C2 **(upper panel)** and A2 **(lower two panels)**.

In the full velocity spectrum (Fig. 4.3a, top panel) at 620 m, we can see relatively narrow and prominent spectral peaks at M_2 and $2M_2$, a slightly broader peak at $M_2 + f$, and a wide jagged "hill" spanning the near-inertial and diurnal-band frequencies. In the narrow-band velocity spectrum (Fig. 4.3b, top panel), the semi-diurnal and diurnal tidal constituents can be clearly discerned in both cyclonic and anti-cyclonic components. In the shear spectrum, the semi-diurnal spectral peak is less prominent than the broad near-inertial peak, as seen in the depth-frequency plots of shear PSD. Energy from near-inertial waves is apparent at the local inertial frequency f, with a gradual fall-off towards higher frequencies due to contribution from inertial waves coming from higher latitudes. Spectral peaks near $M_2 \pm f$ can be attributed to vertical advection of near-inertial shear by the semi-diurnal internal tide and possible non-linear wave-wave interactions between near-inertial waves and the M_2 internal tide (Guiles, 2009). Deeper in the water column at 1124 m (Fig. 4.4), spectral energy decreases overall, but peaks at the tidal frequencies are still clearly distinguishable in both velocity and shear spectra. Superharmonics of M_2 and {(integer multiples of M_2) $\pm f$} become more visible as the overall spectral energy decreases.

(a)

Figure 4.3 a) Rotary spectra of velocity **(top)** and shear **(bottom)** from the HOME A2 mooring at 620 m (averaged from 584-656 m depth), shown in the full frequency range (0.01-45 cpd). Ninety-five percent confidence intervals (green) depend on frequency and depth averaging, as discussed in Chapter 3;

(b)
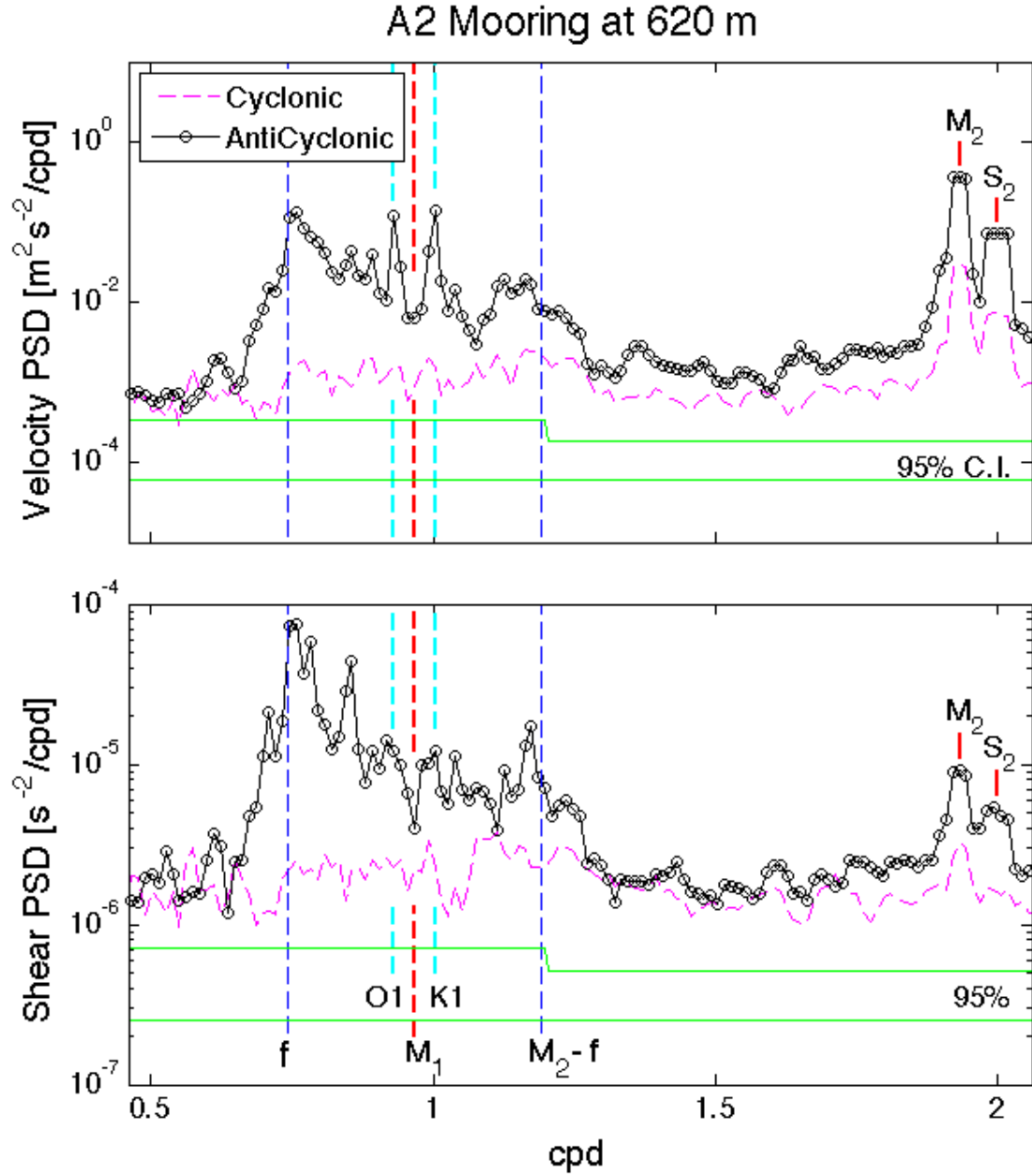
Figure 4.3 b) Rotary spectra of velocity **(top)** and shear **(bottom)** from the HOME A2 mooring at 620 m, shown in the narrow-band frequency range (0.5-2.1 cpd). For frequencies less than $M_2 - f$, every other plotted point is independent; for frequencies greater than $M_2 - f$, every third point is independent.
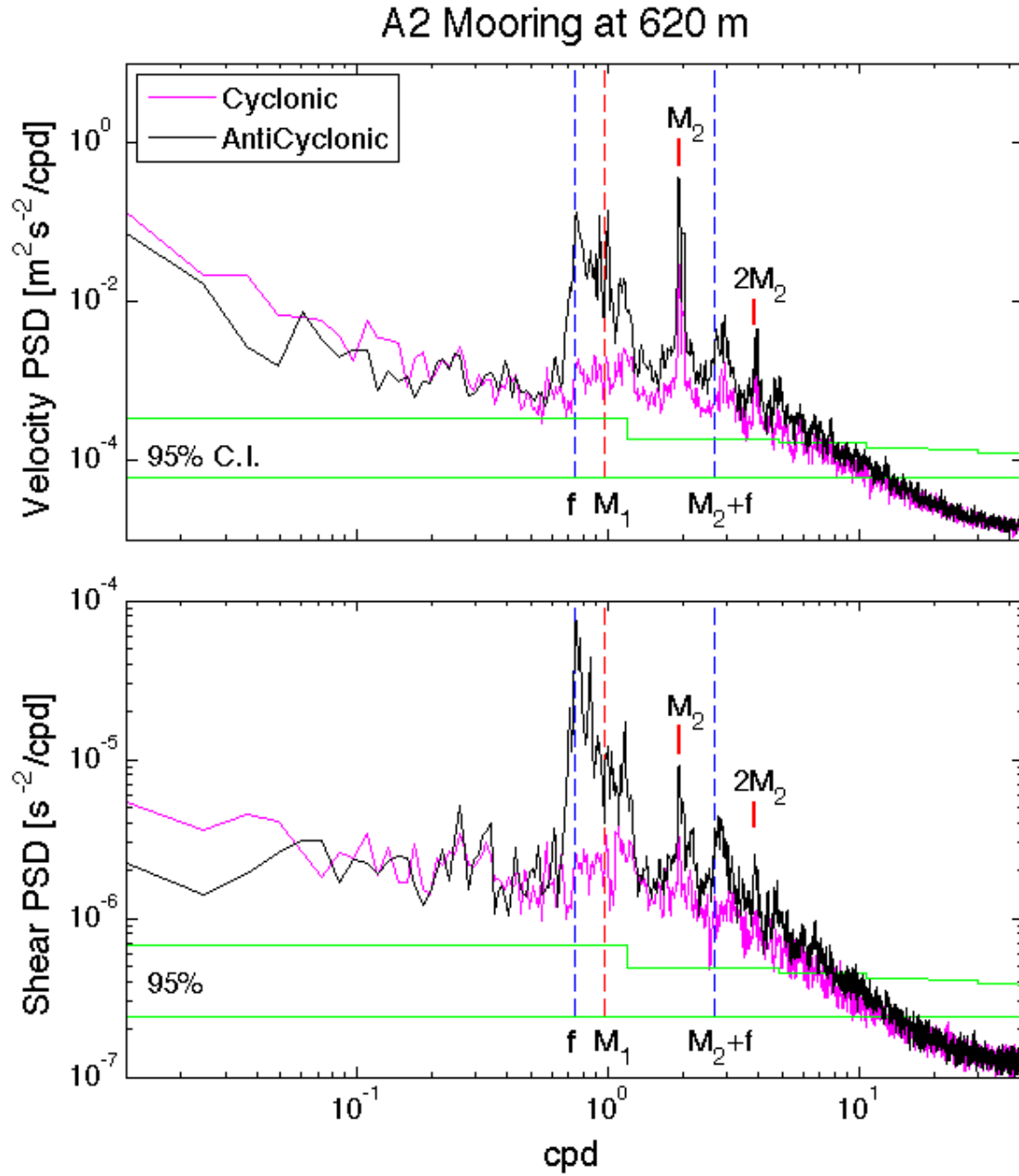
(a)
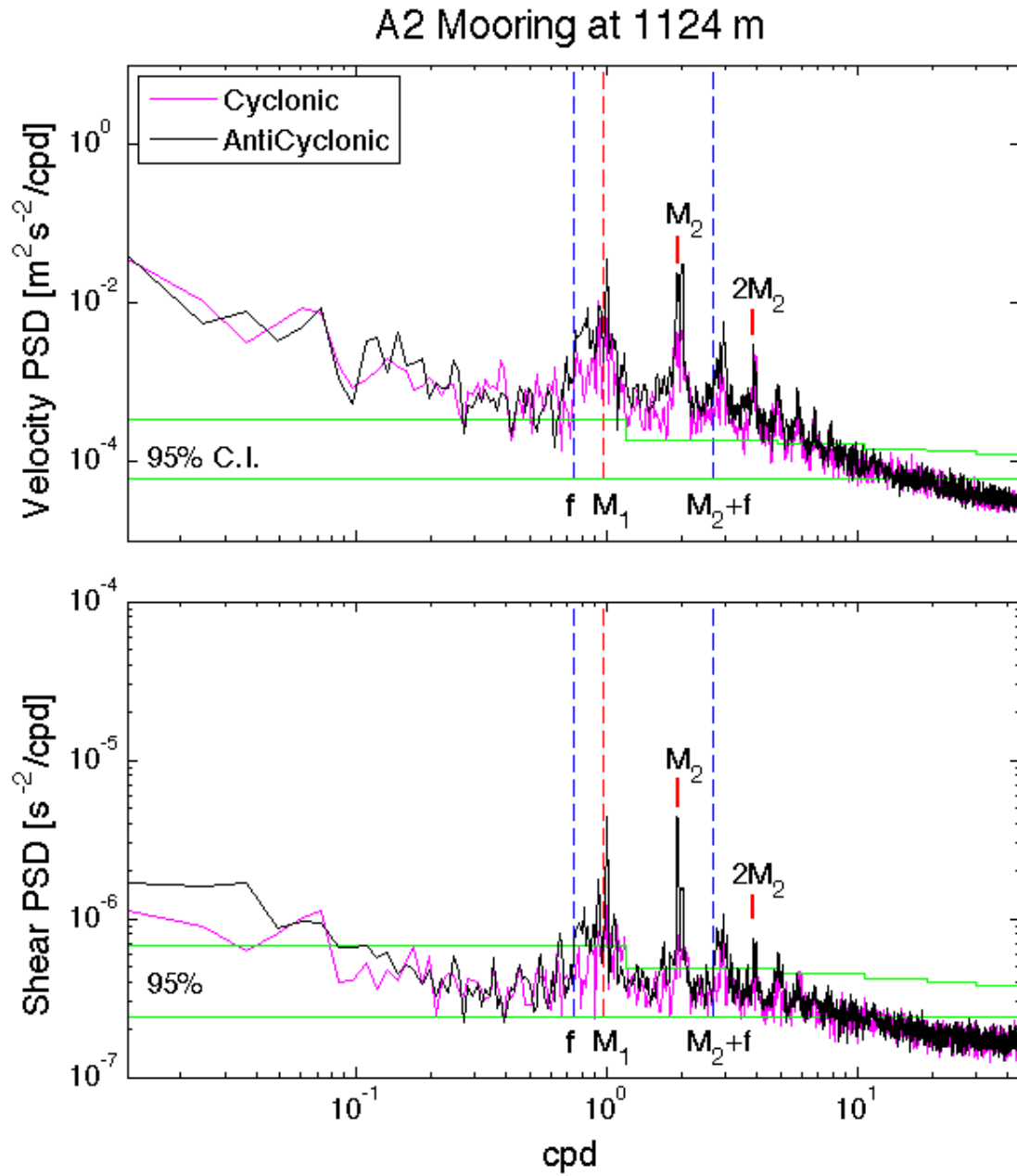
Figure 4.4 a) Rotary spectra of velocity **(top)** and shear **(bottom)** from the HOME A2 mooring at 1124 m (averaged from 1088-1160 m depth), shown in the full frequency range (0.01-45 cpd);

(b)
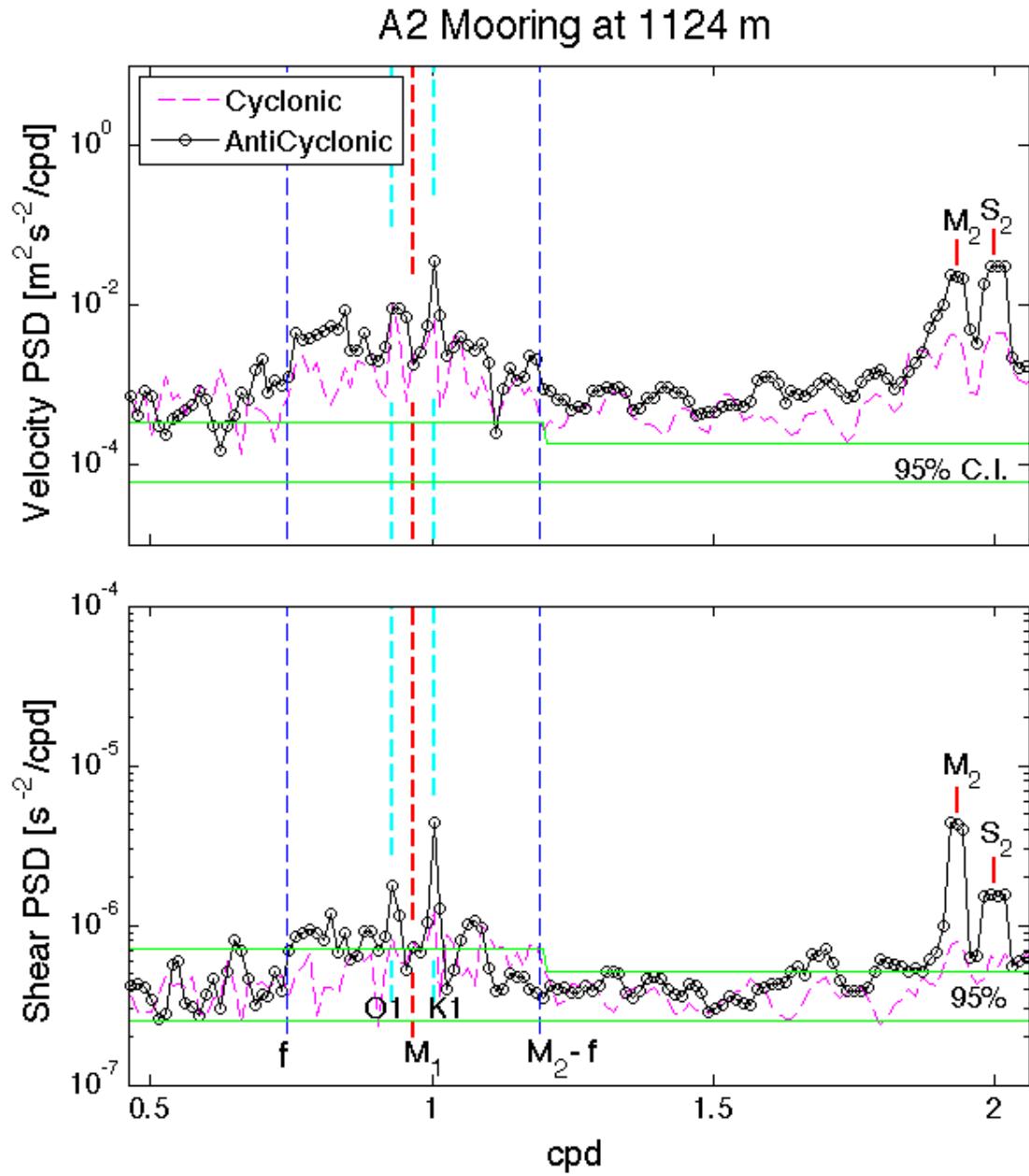
Figure 4.4 b) Rotary spectra of velocity **(top)** and shear **(bottom)** from the HOME A2 mooring at 1124 m, shown in the narrow-band frequency range (0.5-2.1 cpd).

The vertical profiles of velocity and shear PSD at M_1, the inertial frequency, and tidal frequencies (O_1, K_1, M_2) were calculated with three-point frequency-averaging and ten-bin depth-averaging (every other point in Figures 4.5-6 is independent). The velocity PSD profile for the A2 mooring shows M_2 internal tide energy at a maximum near 700 m (where unfortunately there is a gap in the data), and a more complex vertical structure for the local inertial and M_1 frequencies (Fig. 4.5). At the C2 mooring (Fig. 4.6), spectral energy at M_2 continues increasing up to the shallowest depth for which there are reliable observations (344 m), suggesting that the M_2 tidal beam has moved ~350 m in the vertical over a horizontal distance of 17 km (with ratio of vertical to horizontal scale close to 0.025, the calculated value of the aspect ratio based on equation 3).
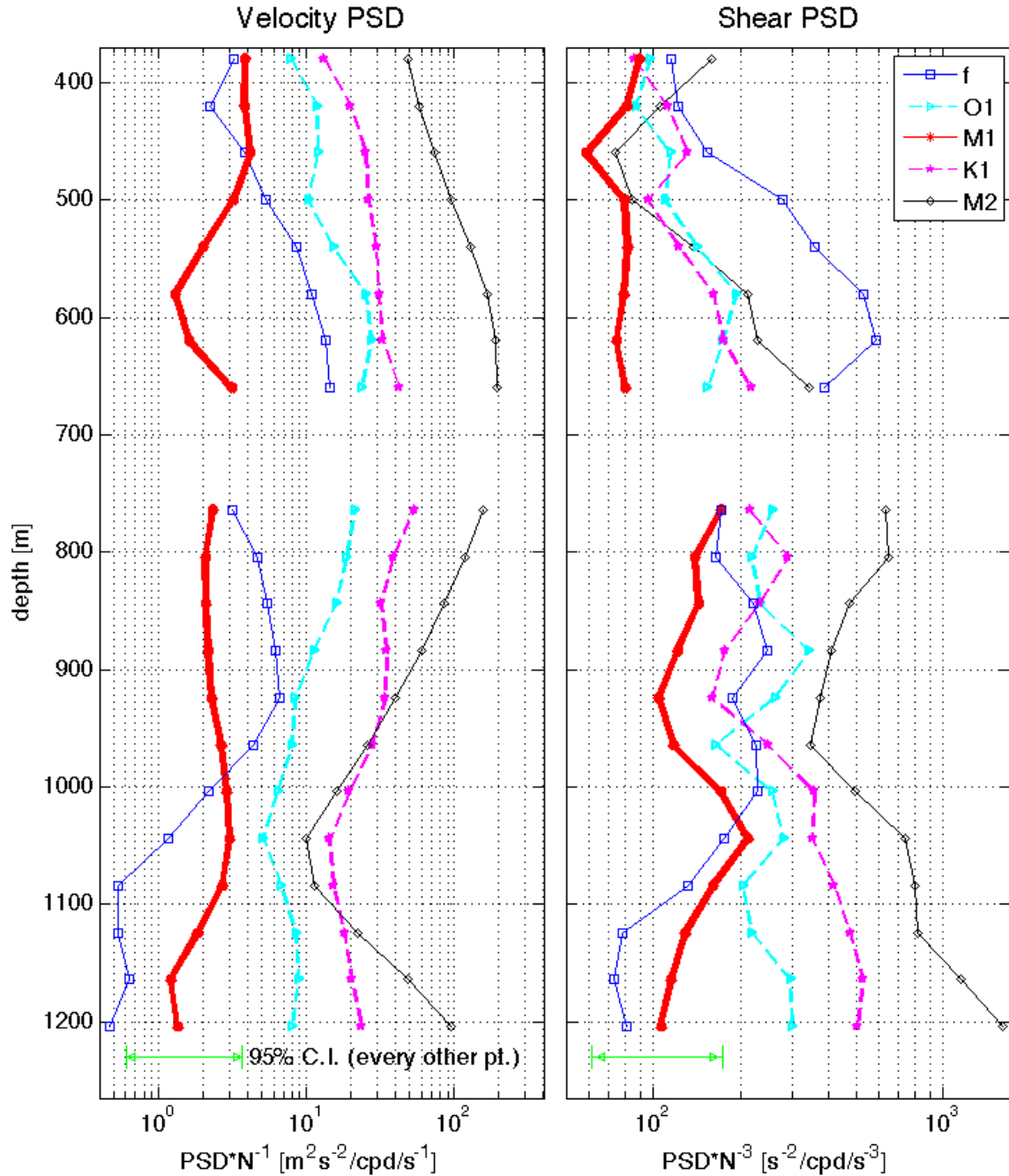
Figure 4.5 Scaled velocity PSD **(left)** and shear PSD **(right)** for the HOME A2 mooring. Power spectral densities were calculated as the average over a 3-component frequency band centered at the noted frequency. Depth-averaging was done with 50% overlapping windows spanning ten 8-m bins. Shear spectra from 344 m (and 728 m) might be influenced by error due to interpolation, affecting 1/10 of the averages at 380 m and 764 m.
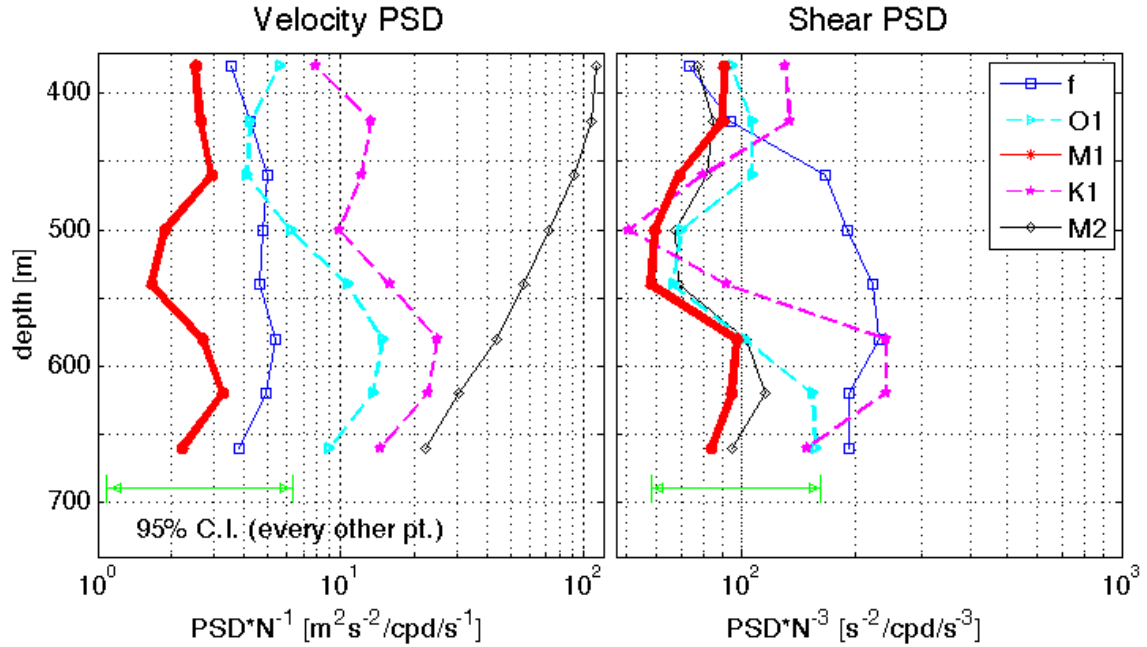
Figure 4.6 Scaled velocity PSD **(left)** and shear PSD **(right)** for the HOME C2 mooring (normalized by the reciprocal of the buoyancy frequency N). Shear spectra from 344 m might be influenced from error due to interpolation; affects 1/10 of spectra used for the average at 380 m.

4.2 Bispectra and Bicoherence of Velocity

Bispectral analysis is often used in the study of non-linear interactions, and its application to the HOME A2 mooring dataset can potentially facilitate further comparison with existing studies. At 764 m where the M_2 internal tide is extremely energetic, elevated bispectral values (exceeding background levels by at least an order of magnitude) were found for frequency triplets involving M_2, K_2, O_1 and K_1 (Fig. 4.7), similar to results from using a synthetic dataset (Fig. 3.11). As with the synthetic dataset, bicoherence levels that have been interpreted as indicating non-linear interactions are observed for current observations from the A2 mooring (Fig. 4.8).

The consistency relationship between cyclonic and anti-cyclonic components of internal waves (Müller and Siedler, 1976), already observed in the auto-spectra, explains why the highest bispectral values occur for triplets in region A (for reference to the full bispectrum, see Fig. 3.10). For a given point, the horizontal and vertical coordinates correspond to the frequency of the first and second waves of a triad, respectively, and the frequency of the third wave is equal to the sum of the first two waves. The intersections of three lines indicate triads of tidal frequencies, and most observed bispectral peaks in the shown regions occur at such intersections. In general, bispectra and bicoherence need to be considered together, with either one insufficient by itself for indicating non-linear interactions. The frequency triplet $(-K_1, -K_1, -K_2)$ is an example of elevated bispectra but insignificant bicoherence, and the triplets $(-O_1, -M_1, -N_2)$, and $(+K_1, +O_1, +M_2)$ are examples of high bicoherence (near the estimated 90% significance level) without elevated bispectra.

A depth profile of bispectral energy and bicoherence for four different frequency triplets (Fig. 4.9) shows that $(-O_1, -K_1, -M_2)$ consistently has both high bispectral and bicoherence values from 660-884 m. In contrast, the triplets $(-M_1, -M_1, -M_2)$ and $(-O_1, -M_1, -N_2)$ have bispectral values an order of magnitude less than $(-O_1, -K_1, -M_2)$ throughout most of the observed depths, and their bicoherence values are never above the 90% significance level. Our main conclusion is that the $(-O_1, -K_1, -M_2)$ triad has higher bispectral energy (by an order of magnitude) and higher bicoherence (> 0.1) than the $(-M_1, -M_1, -M_2)$ triad, continuously throughout the water column from 420-1000 m.
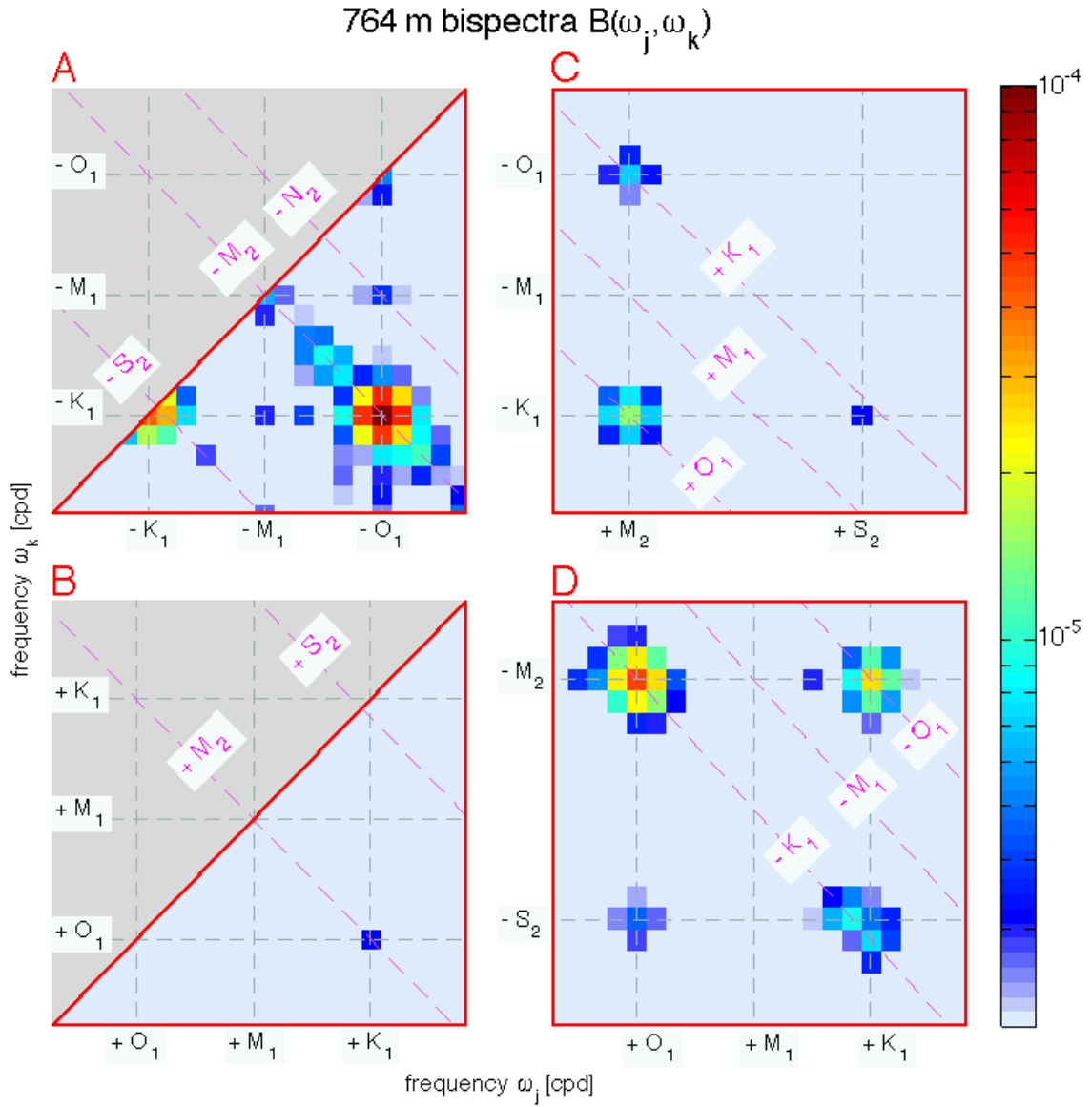
Figure 4.7 Bispectra of complex velocity from HOME A2 mooring at 764 m, with depth-averaging over ten 8-m depth-bins (728-800 m); bispectral values elevated at least an order of magnitude above the background are observed in regions **A (top left):** $(-O_1, -K_1, -M_2)$, $(-K_1, -K_1, -K_2)$ and **D (lower right):** $(+O_1, -M_2, -K_1)$, $(+K_1, -M_2, -O_1)$.

764 m bicoherence b(ω_j, ω_k)
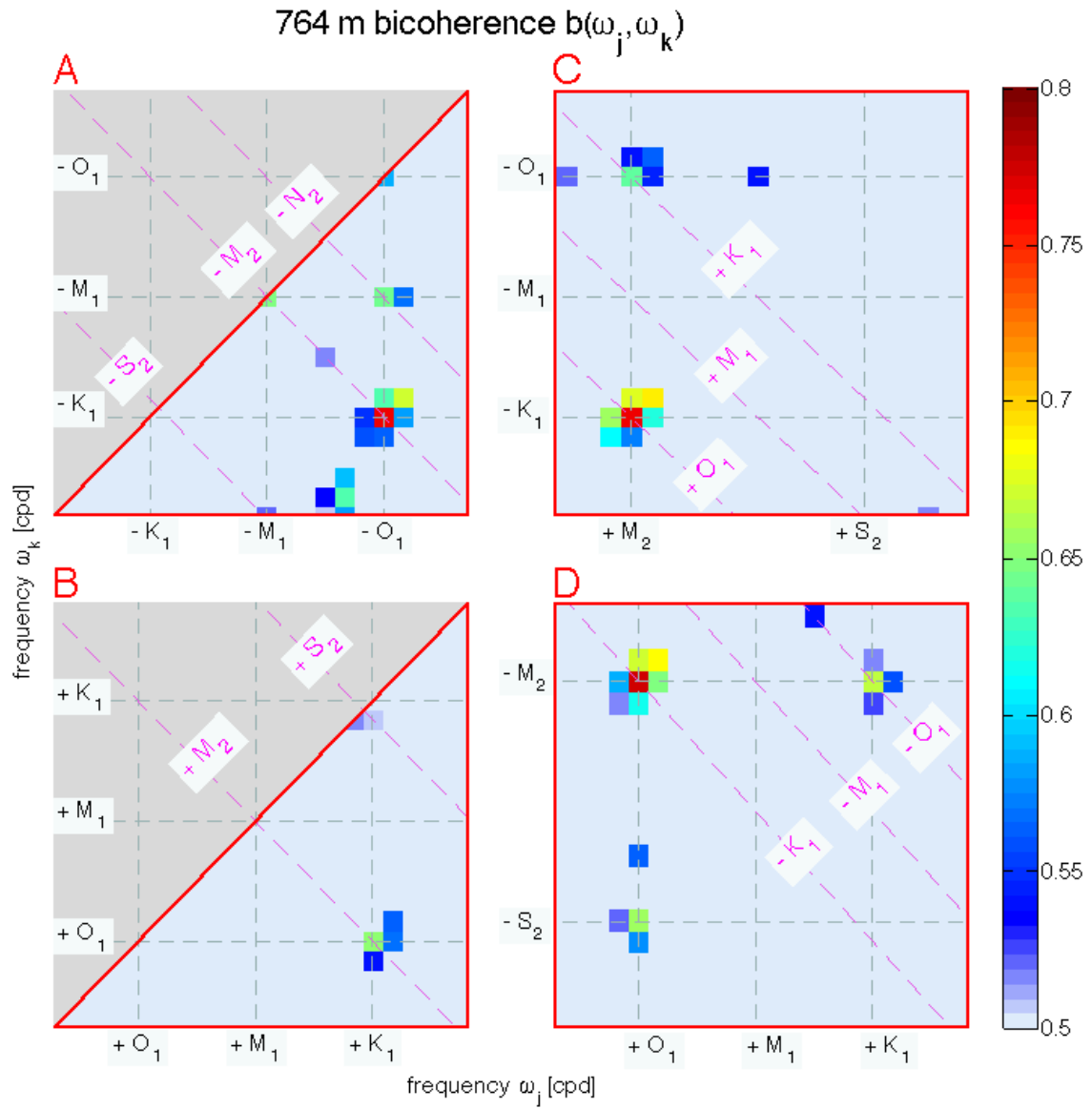
Figure 4.8 Based on estimate of 8 DOF , two frequency triplets show elevated bispectra and bicoherence values close to or above the 90% significance level (~ 0.76): (-O_1, -K_1, -M_2), (+O_1, -M_2 , -K_1).
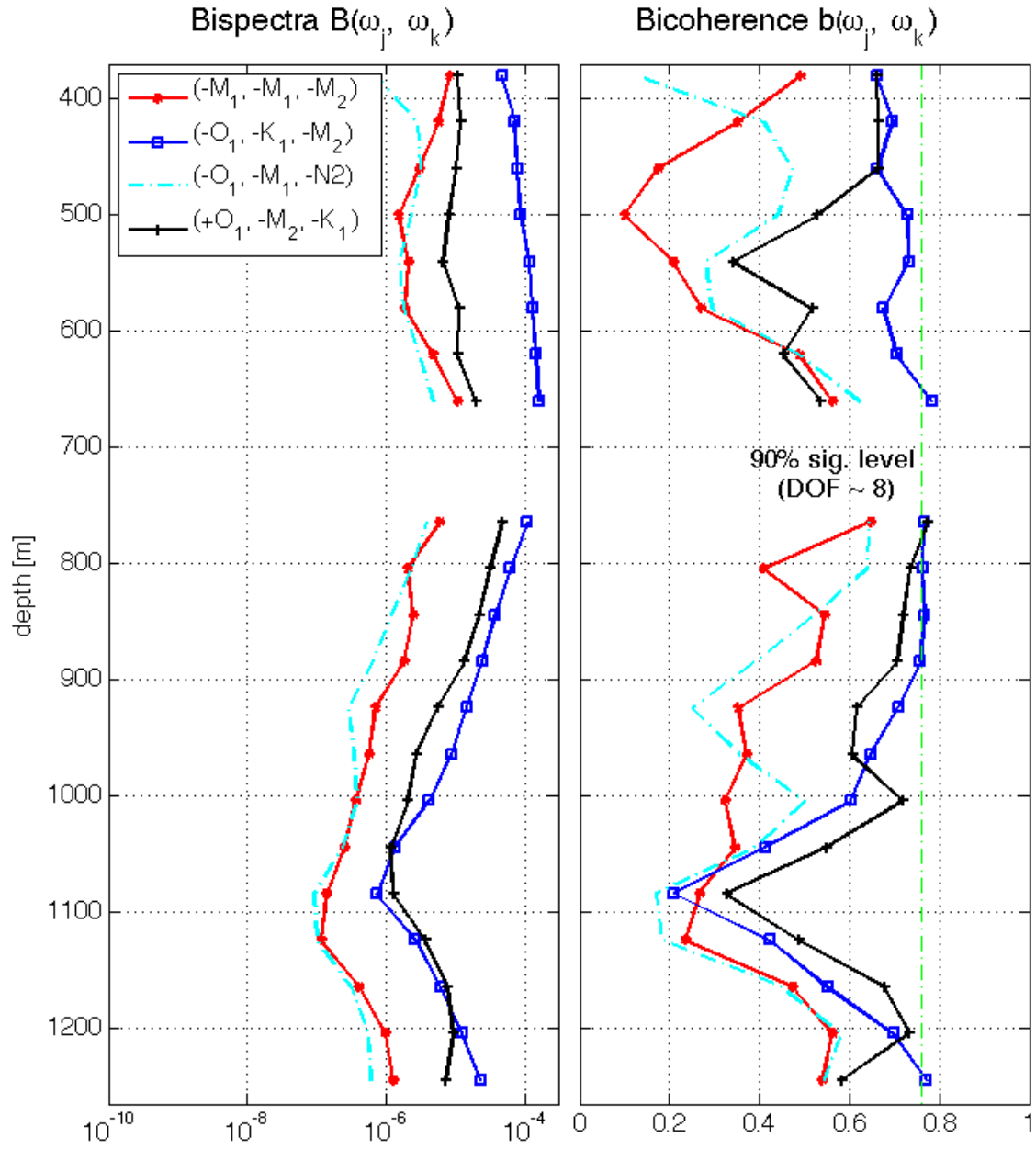
Figure 4.9 Bispectral energy and bicoherence for frequency triplets in region **A**: (-M$_1$, -M$_1$, -M$_2$), (-O$_1$, -K$_1$, -M$_2$), (-O$_1$, -M$_{21}$, -N$_2$) and **D:** (+O$_1$, -M$_2$, -K$_1$), with expectation values calculated from frequency and depth-averaging over ten 8-m depth-bins.

5. Discussion

5.1 Spectral Energy at M_2 Subharmonic

Within the depth ranges of strongest M_2 tidal energy at the HOME A2 and C2 mooring locations (550-800 m and 350-550 m, respectively), the velocity PSD at M_1 is approximately 10^{-2} of the velocity PSD at M_2 (at its highest near 1050 m at the A2 mooring location, the ratio is ~ 1/3). For convenience we define the Subharmonic Energy Ratio (SER),

$$\text{SER} \; := \; \frac{\text{velocity PSD at } M_1}{\text{velocity PSD at } M_2} \tag{8}$$

which can be useful as a benchmark for past and future models of non-linear energy transfer from the M_2 tide to M_1. Order of magnitude estimates of SER were made based on published figures of numerical modeling studies (with only M_2 and no diurnal tide forcing), and summarized in Table 5.1 (compare with Table 1.1).

	SER estimate	Notes:
MacKinnon and Winters (2003), or MW03	~ 1-4 at 21°S (inversely proportional to distance from bottom)	Estimates are based on Figure 4 (right panel) of horizontal kinetic energy spectra calculated from 4-day time series of quasi-steady state.
MacKinnon and Winters (2005), or MW05	~ 10^2 at 29°N ~ 10 at 28°N ~ 1 at 26°N ~ 10^{-1} at 24°N	Based on Figure 1 (bottom panel) of horizontal kinetic energy spectra. Results are sensitive to vertical resolution and M_2 amplitude. Bandwidth of M_1 appears to decrease with latitude (~1 cpd at 29°N and ~0.5 cpd at 24°N); horizontal wavenumber of M_1 is half of M_2.
Gerkema et al. (2006)	~ 10^{-3} at 45°N ~ ½ at 27.5°N ~ 2×10^{-2} at equator	Based on Figure 3 of depth-averaged total kinetic energy (u, v, and w) spectra, calculated from 3-day time series (the runs span ~8 days each).

Table 5.1 Comparison of SER estimated from various numerical modeling studies. Due to the short time series used, spectral estimates at M_1 are of the broader diurnal-band.

The model from MacKinnon and Winters (2003) is initialized with a bottom-localized, narrow-band field of upward propagating internal waves of M_2 frequency, at 21°S. The strength of PSI energy transfer is largest near the ocean bottom, decreasing with distance until SER is about 25% of the maximum at 4 km from the sea floor. We find the SER estimate from MW03 to be much larger than our observations in the Kauai Channel, even though the latitudes are similar. Differences in the spectral and physical characteristics of the M_2 forcing, distance of observations from the internal tide generation region, and techniques used to calculate frequency spectra, may contribute to differences in SER.

MacKinnon and Winters (2005) explore a larger model domain, spanning 30° in latitude, and initialize simulations with northward baroclinic (mode-1) M_2 flux of ~1.7k W/m. Although SER appears to be greater than 10 at the M_1 SHTL, it drops rapidly towards the equator, to approximately 10^{-1} at 24°N. There are many factors which might have caused the SER of MW05 to be different from the SER of MW03, one of which is that the direction of M_2 tide propagation is in the vertical for the latter, while for the former it is in the horizontal and over a much larger range. For MW05 spectral energy at M_1 is the greatest near the M_1 SHTL, and diminishes with latitude.

The simulation of Gerkema et al. (2006) is forced by the M_2 barotropic tide and models internal tide generation over a continental slope. The inclusion of more vertical modes in the M_2 solution is potentially an advantage in modeling non-linear resonant triad interactions when compared to simulations which are initialized with single mode baroclinic waves. However, comparison with our observations suggest that Gerkema et al. (2006) may be overestimating the net transfer of energy to M_1

since their SER at the equator is greater than what is observed at 22°N. There are no

SER estimates from Gerkema et al. (2006) near our location, and to our knowledge

there has not been further work using this model.

Regional numerical process studies at the Hawaiian Ridge would be useful to

further explore the dependence of non-linear wave-wave interactions (in terms of

energy transfer rates as well as the amplitude, frequency, and bandwidth of small-

scale secondary waves) on parameters such as amplitude as well as temporal and

spatial variability of the semi-diurnal tidal forcing, the slope and proximity of internal

tide generating topography, density stratification, and the space-time structure and

variability of inertial energy.

5.2 Nonlinear Interactions between M_2 and M_1

A broad diurnal spectral peak in shear PSD has often been considered as evidence

for energy transfer from the M_2 internal tide to M_1. Using moored current observations

from the northeastern South China Sea (~20°N), Xie et al. (2011) conclude that "The

occurrence of PSI for the entire 75-day is not occasional, as the [near-inertial and near-

diurnal] shear amplitude is heightened at each semidiurnal spring tide." However, it

appears that even with a relatively long dataset of 75 days there can be insufficient

frequency resolution for distinguishing between the principal diurnal internal tides and

M_1 in the shear field (Fig. 5.1).
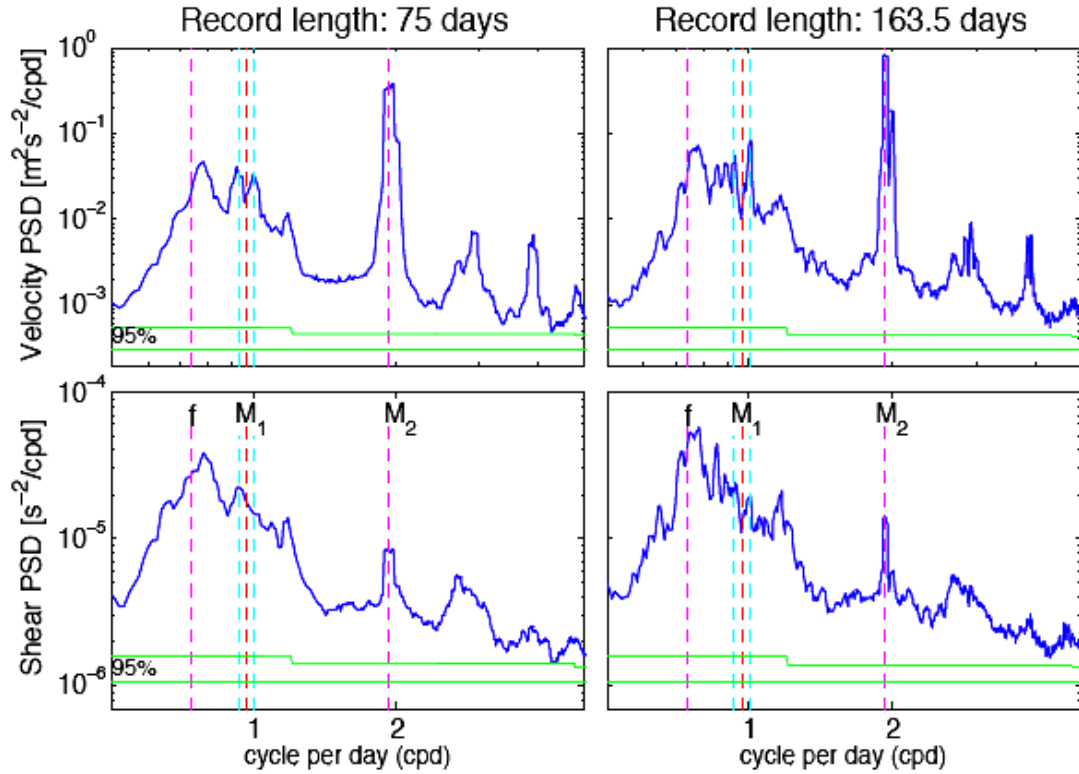
Figure 5.1 Depth-averaged (352-624 m) horizontal velocity **(top panels)** and vertical shear **(bottom panels)** PSD using HOME A2 mooring data subset of length 75 days **(left panel**: Mar. 20 to Jun. 4, 2003**)** and 163.5 days **(right panel**: Dec. 2, 2002 to May 15, 2003**)**. Frequency-smoothing in the diurnal-band is minimal at three-points; for comparison of different smoothing windows see Fig. 3.8.

Although it is outside the scope of the present study to comment on observational evidence of "PSI-induced near-inertial waves", our results suggest an alternative perspective on the observation of heightened near-diurnal shear amplitude. Based on the identification of O_1 and K_1 spectral peaks in the vertical shear field, the increase of near-diurnal shear amplitude could be more simply explained by the smaller vertical-scale diurnal internal tides which also follow a spring-neap cycle. Although diurnal and semi-diurnal spring-neap cycles appear "nearly out of phase" in the time-series used by Xie et al. (2011), it is unclear whether their observed diurnal shear amplitude is in phase with

either cycle[9]. Statistically reliable results are difficult to obtain when there are less than 6

spring-neap cycles in their observations, along with large variability in amplitudes and

spatial extent. In addition, the semi-diurnal tidal beam appears to have already reflected

off the sea surface, becoming less energetic and less beam-like.

Numerical simulations by (Simmons, 2008) suggest that subharmonic instabilities

require a minimum "threshold" of internal wave energy, and "internal tides with

sufficient energy principally occur in beam-like structures". The presence of energetic

semi-diurnal tidal beams is an important factor in explaining the small vertical extent of

significant bicoherence between M_1 and M_2 spectral energies in the study by Carter and

Gregg (2006). In Xie et al. (2011), bicoherence was found to be significant at the 95%

level for the frequency triplet (2, 2, 4) cpd from approximately 75-125 m, and for (0.83,

1.17, 2) cpd from 145-155 m. However, these depth ranges do not appear to coincide with

the depths of strongest semi-diurnal tidal energy for their dataset, making it unlikely that

non-linear interaction with the semi-diurnal tide is occurring only in this narrow depth-

range.

Sun (2010) studied evidence for PSI at both the HOME Farfield and Nearfield

locations. The apparent phase alignment of diurnal spring-neap energy flux with semi-

diurnal current at the HOME Farfield location (Rainville and Pinkel, 2006a), an argument

similar to the one employed by Xie et al. (2011), was found by Sun (2010) to be

inconclusive. At the HOME Nearfield location, Sun (2010) found evidence of PSI in the

across-ridge and along-ridge vertical shears, suggesting that upward and downward

9   Spring-neap cycles of diurnal and semi-diurnal barotropic tides are periodically in-phase and out-of-
      phase because the beat frequency of O_1-K_1 differs slightly from that of M_2-S_2 (Fig. 3.4). Care must be
      taken before drawing conclusions from short records with only a small number of cycles.

propagating internal waves near the diurnal period are interacting with the semi-diurnal

internal tide. However, the limitations due to short record length are again relevant for

this dataset (~35 days), and the interpretation of resultant spectra and bispectra need to

carefully take into account the presence of unresolved O_1 and K_1 internal tides.

Although resonant triads can exist at ~22°N with two waves that are both close

in frequency to M_1 (an example is given in Appendix B), observations from the HOME

A2 and C2 moorings show that there is less spectral energy at M_1 than at O_1 and K_1.

Bispectral analysis also does not show indication of non-linear energy transfers

between M_2 and M_1 at this location.

It is worth noting that many studies find that the efficiency of PSI drops

sharply equatorward of 25° latitude (Furuichi et al., 2005; MacKinnon and Winters,

2005; Qiu et al., 2012). This is expected and can be easily understood by examining

the horizontal group velocity of internal waves. When the aspect ratio α is small

compared to N/f, the hydrostatic approximation applies (Gill, 1982) and the

approximate form of the (f-plane) internal wave dispersion relation is:

$$\omega^2 \approx f^2 + N^2 \kappa_h^2 / \kappa_z^2 = f^2 + N^2 \alpha^2 \tag{9}$$

where κ_h and κ_z are the horizontal and vertical wave-numbers, respectively. From

the dispersion relation the horizontal group velocity can be calculated as follows:

$$c_{gH} := \frac{\partial \omega}{\partial \kappa_h} \approx \frac{N^2 \kappa_h}{\kappa_z^2 \omega} = \frac{\omega}{\kappa_h}\left(1 - \frac{f^2}{\omega^2}\right) = c_{pH}\left(1 - \frac{f^2}{\omega^2}\right) \tag{10}$$

and it is clear that energy transferred from PSI of the M_2 tide to secondary waves can

radiate away when $\omega > f$. At the M_1 SHTL where f is equal to $\omega = M_1$, the f-plane

representation is no longer valid and the β-plane formulation (Munk, 1980) is more

appropriate, but much more complicated. The important point which can be seen from

(10) is that the magnitude of the horizontal group velocity for M_1 decreases towards the

M_1 SHTL, and grows equatorward. Recent observational studies (Qiu et al., 2012;

MacKinnon et al., 2013a, 2013b) suggest that the importance of PSI is highly dependent

on latitude, with the highest growth rates near the M_1 SHTL[10], as predicted by numerical

and analytical studies (MacKinnon and Winters, 2005; Young et al., 2008; Simmons,

2008, Hazewinkel and Winters, 2011).

5.3 Consideration of Non-subharmonic Resonance

At the M_1 SHTL where f is equal to M_1, secondary PSI-waves forced by the M_2 tide

are restricted to having almost exactly M_1 frequency[11]. However, at latitudes equatorward

of the M_1 SHTL, internal waves with frequencies lower than M_1 can propagate freely, and

resonant interactions with the M_2 tide could involve internal waves with frequencies both

higher and lower than M_1. There is no general consensus on the issue of which

frequencies are preferred by the PSI mechanism, though analytical and numerical studies

---

10 In contrast, Dushaw et al., (2011) could detect no loss of mode-1 internal tide energy flux at the M_1
     SHTL north of the Hawaiian Ridge from a precise tidal analysis of altimetry data.

11 Resonant triads involving exactly two frequencies, M_2 and M_1, imply that the M_1 waves of such a triad
     would have larger horizontal length scales than the forcing wave M_2, contradicting the original
     definition of triads in the PSI class by McComas and Bretherton (1977). Such triads also do not occur in
     the numerical simulations of Hazewinkel and Winters (2011).

(Staquet and Sommeria, 2002; Hazewinkel and Winters, 2011) postulate that the closer

the secondary-wave frequencies are to being equal, the faster the PSI growth[12].

For the purpose of our empirical study, we briefly consider possible resonant triads

such as:

$$f + (M_2 - f) = M_2 \qquad (11)$$

$$K_1 + O_1 = M_2 \qquad (12)$$

$$K_1 + K_1 = K_2 \qquad (13)$$

At the HOME A2 mooring location, a large part of the spectral energy near $M_2 - f$ (and

$M_2 + f$) can be attributed to advection effects and possible non-linear wave-wave

interactions (non-resonant) between near-inertial waves and the M_2 internal tide (Guiles,

2009), thereby eliminating (11) as a potentially important resonant interaction at this

location. Results from bispectral analysis of current observations suggest that there are

triad interactions described by (12) and (13). However, experiments with a synthetic

time-series which does not contain any interaction mechanism also showed elevated

bispectral and bicoherence for triads (12) and (13) (Figures 3.11-12). Additionally,

numerical simulations of K_1 internal tide generation at Kaena Ridge are consistent with

observations from the HOME A2 and C2 moorings, especially at the depths where M_2 is

strongest (Fig. 2.9), suggesting that there is not a significant net transfer of energy from

M_2, S_2 or K_2 to K_1. The application of bispectral methods to deterministic signals such as

the tides has many unresolved issues and warrants further study.

---

12 Viscosity limits the maximum wavenumbers of secondary waves and determines how closely their
    frequencies can match (Hazewinkel and Winters, 2011; Joubaud et al., 2012).

6. SUMMARY AND CONCLUSION

Within the last two decades, altimetry-constrained barotropic and baroclinic tidal simulations have shown that barotropic tides, along with winds, could be a major source of mechanical energy for diapycnal mixing in the abyssal ocean. Of the roughly 25% of barotropic tidal energy estimated to be flowing into the internal tides, it is believed that the majority is converted to low-mode baroclinic internal wave energy that does not dissipate locally through turbulence, and the dominant mechanisms which transfer energy from large to small scales are still unknown. A number of studies have suggested that non-linear processes such as PSI will result in a flow of energy from the M_2 tide to small-vertical-scale oscillations at the M_2 subharmonic frequency, and that this can occur anywhere equatorward of 28.8˚ latitude.

Observations from the HOME A2 mooring show a beam-like concentration of semi-diurnal energy from 500-700 m depth, consistent with observations and numerical model predictions of strong internal tides moving southwestward from Kaena Ridge to intersect the mooring within a limited vertical extent. Frequency spectral analysis was used as a tool for examining the distribution of energy in frequency space for the large vertical-scale velocity field as well as the smaller vertical-scale shear field. We estimated the ratio of velocity PSD at M_1 relative to M_2, a useful metric for comparing with existing studies. This ratio is $O(10^{-2})$ where the M_2 internal tide amplitudes are strongest, lower than predicted by some numerical simulations.

Although numerous observational studies attribute energy in the diurnal-band to non-linear transfers of energy from the M_2 tide to waves of M_1 frequency, it was found in

this dataset that spectral energy in the diurnal-band is mostly distributed at the O_1 and K_1 frequencies, likely due to locally generated internal tides. Bispectral analysis indicates high bicoherence between O_1, K_1 and M_2 internal waves, but more work needs to be done for a proper interpretation of bispectral results when applied to nearly deterministic signals such as the tides. While previous studies have interpreted bicoherence maxima as indication of non-linear wave-wave interaction, experimentation with a simple synthetic dataset made up of non-interacting sinusoids at the tidal frequencies shows high and potentially significant bicoherence. These findings suggest that previous empirical studies which found high bicoherence between the M_2 tide and an unresolved diurnal-band might have been simply observing the energy and consistent phase-relationship of internal tides, and not of non-linear wave-wave interactions. Numerical experiments and Monte Carlo simulations would be useful for complementing existing results of bispectral analysis, and for investigating the various issues of applying bispectral techniques to tidal signals.

One of the main results of this work is the quantification of the spectral energy at M_1 (Figures 4.5-6), which can be used for comparison with numerical simulations of non-linear energy transfers from the M_2 tide to waves of M_1 frequency. Energetic semi-diurnal tidal beams are observed in this dataset, and diurnal-band spectral energies in both velocity and shear fields show peaks at O_1 and K_1, with nearly background levels at M_1. From bispectral analysis it was found that a triad of waves with frequencies at O_1, K_1 and M_2 has higher bispectral energy (by an order of magnitude) and higher bicoherence (> 0.1) than a triad with frequencies at M_1, M_1 and M_2 from 420-1000 m at the HOME A2 mooring location.

APPENDIX A – Vertical Coherence Length (VCL)

The vertical coherence as a function of frequency is estimated from the horizontal currents (with barotropic tide currents removed) at successively larger vertical separations in order to make a rough estimate of the vertical separation distance beyond which the oscillations in the diurnal band would be considered incoherent. This information is needed to determine statistical independence in the estimation of degrees of freedom when current spectra from neighboring depths are averaged.

Given time series of a physical variable (horizontal currents or shear in this case) at each of the depths i and j, let their one-sided auto-spectra and cross-spectra be represented as

$$G_{ii}(\omega_n), G_{jj}(\omega_n), G_{ij}(\omega_n),$$

$$\text{where } \omega_n = \frac{n}{T} \text{ for integers } n \text{ (such that): } 0 \leq n \leq \frac{T}{2\,dt} \tag{14}$$

and dt is the sample interval in time of the discrete time series of length T. In order to increase statistical reliability of the estimates in (14), spectral values are averaged over three adjacent frequencies. The averaging will be represented by an overbar, as follows:

$$\overline{G_{ii}}(\omega_m), \overline{G_{jj}}(\omega_m), \overline{G_{ij}}(\omega_m),$$

$$\text{where } \omega_m = \frac{3m+1}{T} \text{ for integers } m : 0 \leq m \leq \frac{T}{3(2\,dt)} - 1 \tag{15}$$

The spectral estimates in (15) each have 6 DOF and are used to create the squared coherence function

$$\gamma_{ij}^2(\omega_m) = \frac{\left|\overline{G}_{ij}(\omega_m)\right|^2}{\overline{G}_{ii}(\omega_m)\,\overline{G}_{jj}(\omega_m)} \tag{16}$$

The estimator, $\gamma_{ij}^2(\omega_m)$, has a high variance when the smoothing is over only three frequencies. To reduce the variance and to characterize the broader diurnal band, $\gamma_{ij}^2(\omega_m)$ is averaged over $0.7 - 1.3$ cpd, which includes 33 independent ω_m frequencies; this average is designated as $\langle\gamma_{ij}^2(\omega_m)\rangle_d$. Examples of averaged squared coherence $\langle\gamma_{ij}^2(\omega_m)\rangle_d$ for the cyclonic and anti-cyclonic velocities and shears are shown in Figure A1.

The sampling distribution of coherence squared for a pair of white noise sequences constructed with a fixed squared-correlation-coefficient ($R^2 = 0.33$) has a mean of 0.51 for frequency-averaging over three points (E. Firing, personal communication). Even when the true coherence is zero ($R^2 = 0$), the expected value of the coherence squared is 1/3, for frequency-averaging over three points. For the purposes of this study, the VCL will be defined as the minimum separation distance for which diurnal-band oscillations are less than 33% coherent for at least 90% of the depth bins being considered (Fig. A2). For the horizontal velocity field the VCL is 96 m, and there is no increase in DOF from depth-averaging over ten depth-bins, or 80 m. For the vertical shear field the VCL is 40 m, and averaging over ten depth-bins the DOF for shear spectral estimates are increased by a factor of 2.8:

Multiplicative Increase in DOF $= 1 + (N_{avg}-1)/N_{min}$, if $N_{avg} > N_{min}$

where N_{avg} is the number of spectra being depth-averaged (10), and N_{min} is the minimum number of bins which contain two independent estimates.
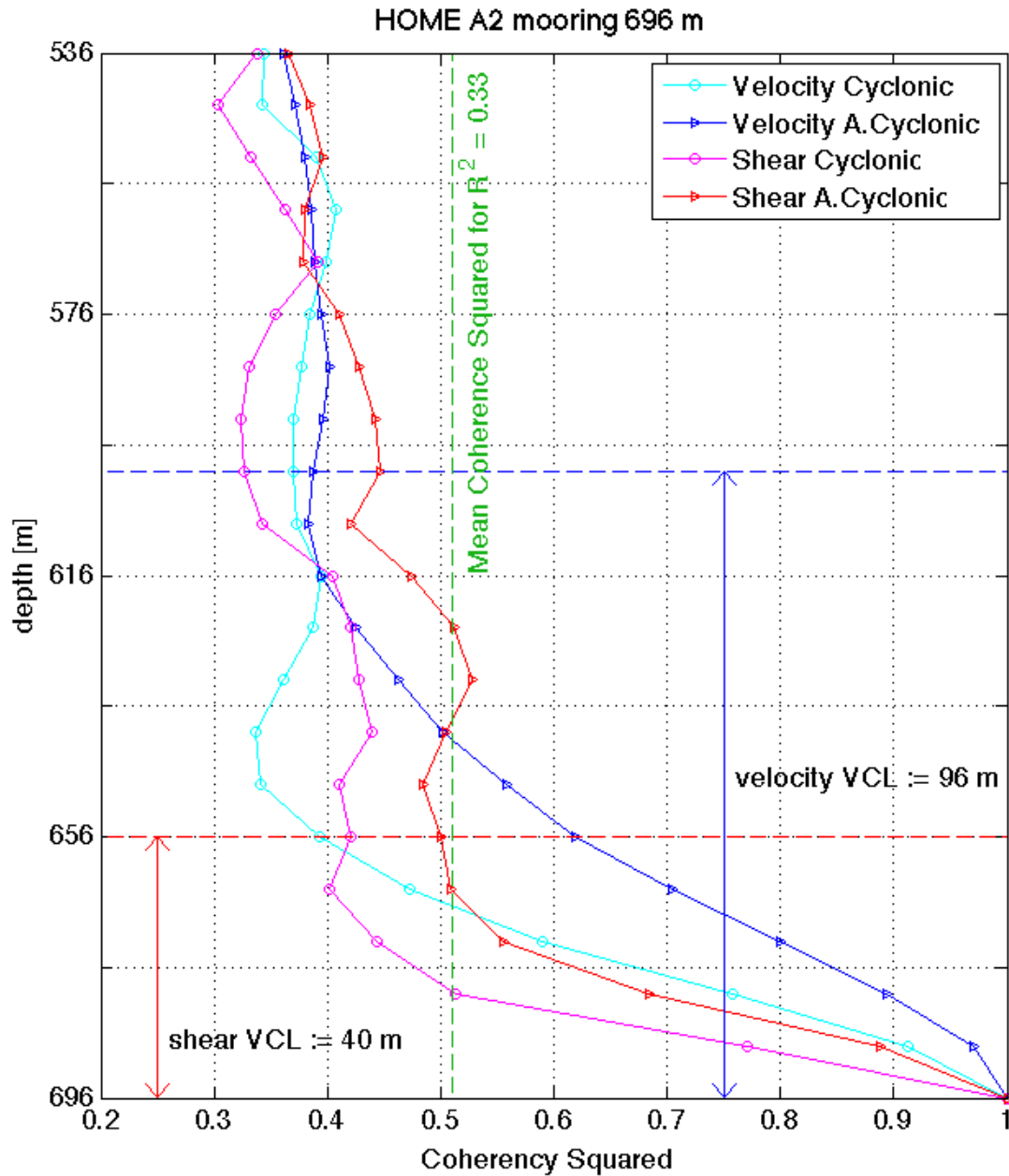
Figure A1. Diurnal band-averages of squared coherency (normalized to have only positive values between 0 and 1) are shown as a function of depth for reference depth of 696 m. The mean of a sampling distribution of coherence squared calculated with 3-point frequency smoothing for a pair of white noise sequences with squared-correlation-coefficient $R^2 = 1/3$ is 0.51 (green line). The velocity and shear VCLs are defined as 96 m and 40 m, respectively, based on the full range of depths. Therefore, the VCL estimates are conservative for many depths, such as the one shown here.

Figure A2. Averaged squared coherence at the chosen VCLs for velocity and shear are plotted as functions of depth; green line is as in Fig. A1.

APPENDIX B – Possible PSI triad at 22˚N

At the A2 mooring location (21.75˚N), where depth ~1 km and $f \sim 0.74$ cpd, the aspect ratio of M_2 is estimated with $N^2 \sim 2.8 \times 10^{-5}$ [s^{-2}]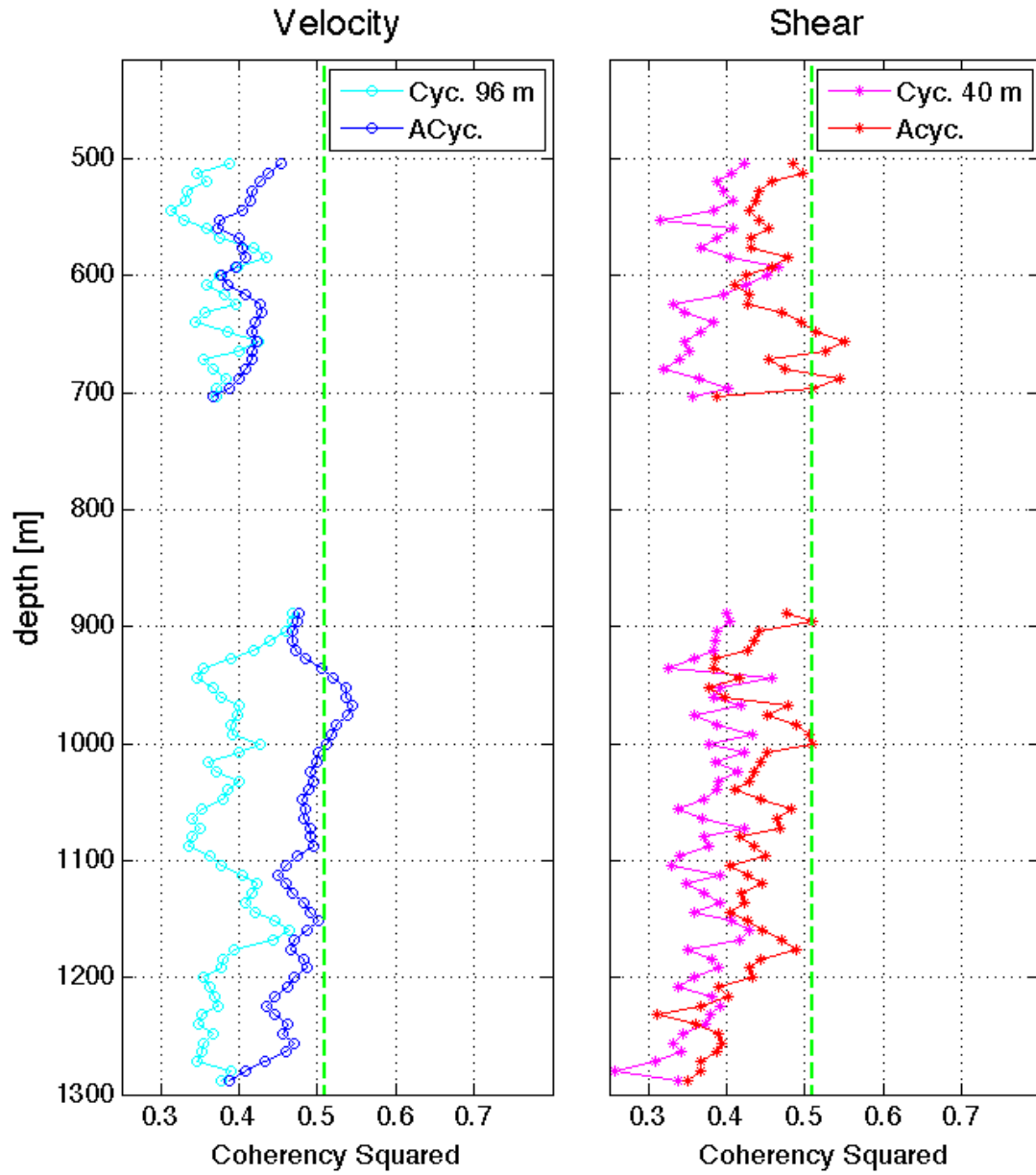 (the 300-800 m depth average at Station Kaena) to determine the horizontal wavelength of a mode-1 M_2 internal tide (the primary wave) with vertical wavelength ~1 km (Fig. 4.5). Estimating the vertical wavelengths of secondary waves to be ~50 m (Hazewinkel and Winters, 2011), PSI triads are possible with the secondary waves separated in frequency by < 0.04 cpd (Fig. B1).
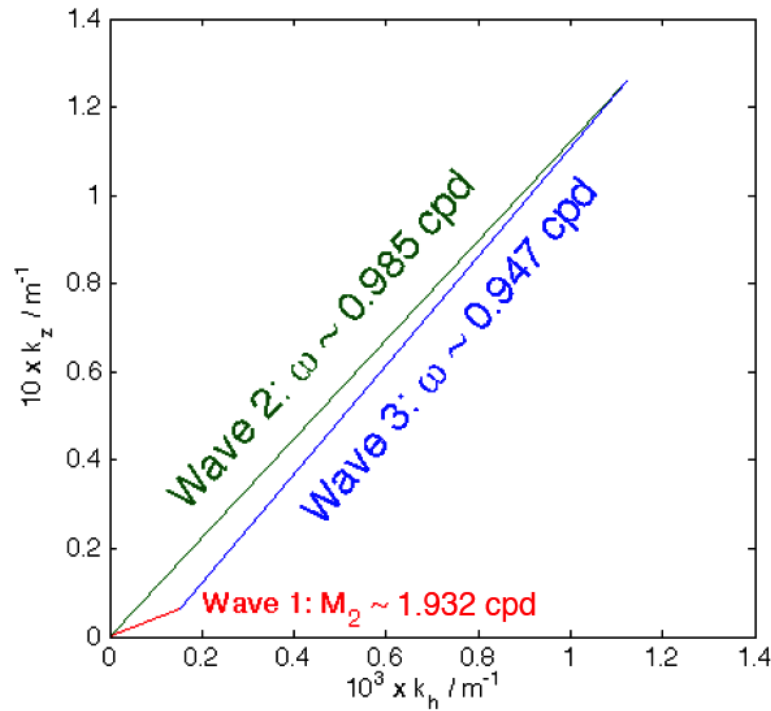
Figure B1. A possible PSI-triad is shown in wavenumber space.

	ω (cpd)	α	L_z, L_h [km]	k_z, k_h [x10^{-3} m^{-1}]	c_{pH}	c_{gH}
M_2 – Wave 1	1.9323	2.45×10^{-2}	1 , 40.7	6.3, 0.15	0.91 m/s	0.78 m/s
Wave 2 of triad	0.9851	8.9×10^{-3}	0.05, 5.59	126, 1.1	0.06 m/s	0.03 m/s
Wave 3 of triad	0.9468	8.1×10^{-3}	0.05, 6.48	119, 0.97	0.07 m/s	0.03 m/s

Table B1. Frequency (ω), aspect ratio (α), vertical and horizontal lengths (L_z, L_h), vertical and horizontal wavenumbers (k_z, k_h), and horizontal phase and group velocities (c_{gH}, c_{pH}) are calculated for each wave in a possible PSI-triad.

References

Alford, M. H. (2008). Observations of parametric subharmonic instability of the diurnal tide in the South China Sea. *Geophys. Res. Lett.*, 35:L15602.

Alford, M. H., MacKinnon, J. A., Zhao, Z., Pinkel, R., Klymak, J., and Peacock, T. (2007). Internal waves across the pacific. *Geophys. Res. Lett.*, 34:L24601.

Aucan, J. and Merrifield, M. (2008). Boundary mixing associated with tidal and near-inertial internal waves. *J. Phys. Oceanogr.*, 38:1238–1252.

Aucan, J., Merrifield, M., Luther, D., and Flament, P. (2006). Tidal mixing events on the deep flanks of Kaena Ridge, Hawaii. *J. Phys. Oceanogr.*, 36:1202–1219.

Bourget, B., Dauxois, T., Joubaud, S., and Odier, P. (2013). Experimental study of parametric subharmonic instability for internal plane waves. *J. Fluid Mech.*, 723:1–20.

Boyd, T. J., Levine, M. D., Gard, S. R., and Waldorf, W. (2005). Mooring observations from the Hawaiian Ridge re. 2005-1. Technical report, Oregon State University. Aug.2002-Jun.2003. Tech. Report No. Ref. 2005-1, Data Report 197.

Carter, G. S. and Gregg, M. C. (2006). Persistent near-diurnal internal waves observed above a site of M2 barotropic-to-baroclinic conversion. *J. Phys. Oceanogr.*, 36:1136–1147.

Carter, G. S., Merrifield, M. A., Becker, J. M., Katsumata, K., Gregg, M. C., Luther, D. S., Levine, M. D., Boyd, T. J., and Firing, Y. L. (2008). Energetics of M2 barotropic-to-baroclinic tidal conversion at the Hawaiian islands. *J. Phys. Oceanogr.*, 38:2205–2223.

Chavanne, C., Flament, P., Carter, G., Merrifield, M., Luther, D., Zaron, E., and Gurgel, K. W. (2010a). The surface expression of semidiurnal internal tides near a strong source in Hawaii. Part I: Observations and numerical predictions. *J. Phys. Oceanogr.*, 40(6):1155–1179.

Chavanne, C., Flament, P., Luther, D., and Gurgel, K. W. (2010b). The surface expression of semidiurnal internal tides near a strong source in Hawaii. Part II: Interactions with mesoscale currents. *J. Phys. Oceanogr.*, 40(6):1180–1200.

Chinn, B. S., Girton, J. B., and Alford, M. H. (2012). Observations of internal waves and parametric subharmonic instability in the philippines archipelago. *J. Geophys. Res.*, 117(C5):C05019.

Cole, S., Rudnick, D. L., Hodges, B. A., and Martin, J. P. (2009). Observations of tidal internal wave beams at Kauai Channel, Hawaii. *J. Phys. Oceanogr.*, 39(2):421–436.

Dushaw, B. D., Howe, B. M., Cornuelle, B. D., Worcester, P. F., and Luther, D. S. (1995). Barotropic and baroclinic tides in the central north pacific ocean determined from long-range reciprocal acoustic transmissions. *J. Phys. Oceanogr.*, 25:631–647.

Dushaw, B. D., Worcester, P. F., and Dzieciuch, M. A. (2011). On the predictability of mode-1 internal tides. *Deep Sea Research Part I*, 58:677–698.

Egbert, G. D. and Ray, R. D. (2000). Significant dissipation of tidal energy in the deep ocean inferred from satellite altimeter data. *Nature*, 405:775–778.

Egbert, G. D. and Ray, R. D. (2001). Estimates of M2 tidal energy dissipation from TOPEX/Poseidon altimeter data. *J. Geophys. Res.*, 106:22475–22502.

Egbert, G. D. and Ray, R. D. (2003). Semi-diurnal and diurnal tidal dissipation from TOPEX/Poseidon altimetry. *Geophys. Res. Lett.*, 30:1907.

Elgar, S. and Guza, R. T. (1988). Statistics of bicoherence. *IEEE Trans. Acoustics, Speech and Signal Processing*, 36:1668–1668.

Emery, W. J. and Thomson, R. E. (2004). *Data Analysis Methods in Physical Oceanography.* Elsevier.

Faraday, M. (1831). On a peculiar class of acoustical figures: and on certain forms assumed by groups of particles upon vibrating elastic surfaces. *Philosophical Transactions for the Royal Society of London*, 121:299–340.

Finnigan, T., Luther, D., and Lukas, R. (2002). Observations of enhanced diapycnal mixing near the Hawaiian Ridge. *J. Phys. Oceanogr.*, 32:2988–3002.

Foda, M. A. and Hill, D. F. (1998). Nonlinear Energy Transfer from Semidiurnal Barotropic Motion to Near-Inertial Baroclinic Motion. *J. Phys. Oceanogr.*, 28:1865–1872.

Furuichi, N., Hibiya, T., and Niwa, Y. (2005). Bispectral analysis of energy transfer within the two-dimensional oceanic internal wave field. *J. Phys. Oceanogr.*, 35:2104–2109.

Garrett, C. and Munk, W. H. (1972). Space-time scales of internal waves. *Geo. Fluid Mech.*, 3:225–264.

Garrett, C. and Munk, W. H. (1975). Space-time scales of internal waves: A progress report. *J. Geophys. Res.*, 80:291–297.

Garrett, C. and St. Laurent, L. (2002). Aspects of deep ocean mixing. *J. Phys. Oceanogr.*, 58:11–24.

Gerkema, T., Staquet, C., and Bouruet-Aubertot, P. (2006). Decay of semi-diurnal internal-tide beams due to subharmonic resonance. *Geophys. Res. Lett*, 33:L08604.

Gill, A. E. (1982). *Atmosphere-Ocean Dynamics*, volume 30. Academic Pr.

Gregg, M. C., Sanford, T. B., and Winkel, D. P. (2003). Reduced mixing from the breaking of internal waves in equatorial waters. *Nature*, 422:513–515.

Guiles, M. (2009). *Energy Redistribution through Tidal and Inertial Wave Interaction*. PhD thesis, University of Hawaii, Manoa.

Hasselmann, K. (1966). Feynman diagrams and interaction rules of wave-wave scattering processes. *Rev. Geophys.*, 4(1):1–32.

Hazewinkel, J. and Winters, K. B. (2011). PSI of the internal tide on a beta-plane: Flux divergence and near-inertial wave propagation. *J. Phys. Oceanogr.*, 41:1673–1682.

Hibiya, T. and Nagasawa, M. (2004). Latitudinal dependence of diapycnal diffusivity in the thermocline estimated using a finescale parameterization. *Geophys. Res. Lett.*, 31:LO1301.

Hibiya, T., Nagasawa, M., and Niwa, Y. (2002). Nonlinear transfer within the oceanic internal wave spectrum at mid and high latitudes. *J. Geophys. Res.*, 107(C11):3207.

Holloway, P. E. and Barnes, B. (1998). A numerical investigation into the bottom boundary layer flow and vertical structure of internal waves on a continental slope. *Cont. Shelf Res.*, 18:31–65.

Johnston, T. M. S. and Merrifield, M. A. (2003). Internal tide scattering at seamounts, ridges, and islands. *J. Geophys. Res.*, 108(C6):3180.

Joubaud, S., Munroe, J., Odier, P., and Dauxois, T. (2012). Experimental parametric subharmonic instability in stratified fluids. *Phys. Fluids*, 24(041703):1–6.

Kang, S., Foreman, M., Crawford, W., and Cherniawsky, J. (2000). Numerical modeling of internal tide generation along the Hawaiian Ridge. *J. Phys. Oceanogr.*, 30:1083–1098.

Kim, Y. C. and Powers, E. J. (1979). Digital bispectral analysis and its applications to nonlinear wave interactions. *IEEE Trans. Plasama Sci.*, 7:120–131.

Klymak, J., Legg, S., and Pinkel, R. (2010). A simple parameterization of turbulent tidal mixing near supercritical topography. *J. Phys. Oceanogr.*, 40(9):2059–2074.

Klymak, J., Moum, J., Nash, J., Kunze, E., Girton, J., Carter, G., Lee, C., Sanford, T., and Gregg, M. (2006). An estimate of tidal energy lost to turbulence at the Hawaiian Ridge. *J. Phys. Oceanogr.*, 36(6):1148–1164.

Klymak, J. M. and Moum, J. (2007a). Oceanic isopycnal slope spectra. Part I: Internal waves. *J. Phys. Oceanogr.*, 37:1215–1231.

Klymak, J. M. and Moum, J. (2007b). Oceanic isopycnal slope spectra. part II: Turbulence. *J. Phys. Oceanogr.*, 37:1232–1245.

Klymak, J. M., Pinkel, R., and Rainville, L. (2008). Direct breaking of the internal tide near topography: Kaena Ridge, Hawaii. *J. Phys. Oceanogr.*, 38:380–399.

Korobov, A. S. and Lamb, K. G. (2008). Interharmonics in internal gravity waves generated by tide-topography interaction. *J. Fluid Mech.*, 611:61–95.

Lamb, K. G. (2004). Nonlinear interaction among internal wave beams generated by tidal flow over supercritical topography. *Geophys. Res. Lett.*, 31:L09313.

Leaman, K. and Sanford, T. B. (1975). Vertical energy propagation of inertial waves: a vector spectral analysis of velocity profiles. *J. Geophys. Res.*, 80(15):1975–1978.

Levine, M. D. and Boyd, T. J. (2006). Tidally forced internal waves and overturns observed on a slope: Results from HOME. *J. Phys. Oceanogr.*, 36:1184–1201.

Liao, G., Yuan, Y., Yang, C., Chen, H., Wang, H., and Huang, W. (2012). Current observations of internal tides and parametric subharmonic instability in luzon strait. *Atmosphere-Ocean*, pages 1–18.

MacKinnon, J. A., Alford, M. H., Pinkel, R., Klymak, J., and Zhao, Z. (2013a). The Latitudinal Dependence of Shear and Mixing in the Pacific Transiting the Critical Latitude for PSI. *J. Phys. Oceanogr.*, 43:3–16.

MacKinnon, J. A., Alford, M. H., Sun, O., Pinkel, R., Zhao, Z., and Klymak, J. (2013b). Parametric Subharmonic Instability of the Internal Tide at 29N. *J. Phys. Oceanogr.*, 43:17–28.

MacKinnon, J. A. and Winters, K. B. (2003). Spectral Evolution of Bottom-Forced Internal Waves. In *Proceedings of the 13th 'Aha Huliko'a Hawaiian Winter Workshop*, pages 73–83.

MacKinnon, J. A. and Winters, K. B. (2005). Subtropical catastrophe: Significant loss of low-mode tidal energy at 28.9 degrees. *Geophys. Res. Lett.*, 32:L15605.

Martin, J. P. and Rudnick, D. L. (2007). Inferences and observations of turbulent dissipation and mixing in the upper ocean at the Hawaiian Ridge. *J. Phys. Oceanogr.*, 37:476–494.

McComas, C. H. and Bretherton, F. P. (1977). Resonant interaction of oceanic internal waves. *J. Geophys. Res.*, 82:1397–1412.

McComas, C. H. and Müller, P. (1981). Time scales of resonant interaction among oceanic internal waves. *J. Phys. Oceanogr.*, 11:139–147.

Merrifield, M. and Holloway, P. E. (2002). Model estimates of M2 internal tide energetics at the Hawaiian Ridge. *J. Geophys. Res.*, 107(C8):3179.

Merrifield, M. A., Holloway, P. E., and Johnston, T. M. S. (2001). The generation of internal tides at the Hawaiian Ridge. *Geophys. Res. Lett.*, 28:559–562.

Müller, P., Holloway, G., Henyey, F., and Pomphrey, N. (1986). Nonlinear interactions among internal gravity waves. *Rev. Geophys*, 24(3):493–536.

Müller, P., Olbers, D. J., and Willebrand, J. (1978). The IWEX spectrum. *J. Geophys. Res.*, 83(C1):479–500.

Müller, P. and Siedler, G. (1976). Consitency relations for internal waves. *Deep Sea Research*, 23:613–628.

Munk, W. and Wunsch, C. (1998). Abyssal recipes II: Energetics of tidal and wind mixing. *Deep Sea Research Part I*, 45:1977–2010.

Munk, W. H. (1980). Internal Wave Spectra at the Buoyant and Inertial Frequencies. *J. Phys. Oceanogr.*, 10:1718–1728.

Nagasawa, M., Hibiya, T., Niwa, Y., Watanabe, M., Isoda, Y., Takagi, S., and Kamei, Y. (2002). Distribution of fine-scale shear in the deep waters of the north pacific obtained using expendable current profilers. *J. Geophys. Res*, 107:3221.

Nikurashin, M. and Legg, S. (2011). A mechanism for local dissipation of internal tides generated at rough topography. *J. Phys. Oceanogr.*, 41:378–395.

Olbers, D. J. and Pomphrey, N. (1981). Disqualifying two candidates for the energy balance of oceanic internal waves. *J. Phys. Oceanogr.*, 11:1423–1425.

Phillips, O. M. (1960). On the dynamics of unsteady gravity waves of finite amplitude: Part 1. The elementary interactions. *J. Fluid Mech.*, 9:193–217.

Pickering, A. and Alford, M. H. (2012). Velocity Structure of Internal Tide Beams Emanating from Kaena Ridge, Hawaii. *J. Phys. Oceanogr.*, 42:1039–1044.

Pinkel, R., Munk, W., Worcester, P., Comuelle, B. D., Rudnick, D., Sherman, J., Filloux, J. H., Dushaw, B. D., Howe, B. M., Sanford, T. B., et al. (2000). Ocean mixing studied near Hawaiian Ridge. *Eos, Transactions American Geophysical Union*, 81(46):545–553.

Pinkel, R., Rainville, L., and Klymak, J. (2012). Semidiurnal Baroclinic Wave Momentum Fluxes at Kaena Ridge, Hawaii. *J. Phys. Oceanogr.*, 42:1249–1269.

Polzin, K. (2004). A heuristic description of internal wave dynamics. *J. Phys. Oceanogr.*, 34:214–230.

Powell, B. S., Janekovic, I., Carter, G. S., and Merrifield, M. A. (2012). Sensitivity of internal tide generation in Hawaii. *Geophys. Res. Lett.*, 39:L10606.

Qiu, B., Chen, S., and Carter, G. S. (2012). Time-varying parametric subharmonic instability from repeat CTD surveys in the northwestern pacific ocean. *J. Geophys. Res.*, 117(C9):C09012.

Rainville, L., Johnston, T. M. S., Carter, G. S., Merrifield, M. A., Pinkel, R., Worcester, P. F., and Dushaw, B. D. (2010). Interference pattern and propagation of the M2 internal tide south of the Hawaiian Ridge. *J. Phys. Oceanogr.*, 40:311–325.

Rainville, L. and Pinkel, R. (2006a). Baroclinic energy flux at the Hawaiian Ridge: Observations from the R/P FLIP. *J. Phys. Oceanogr.*, 36:1104–1122.

Rainville, L. and Pinkel, R. (2006b). Propagation of low-mode internal waves through the ocean. *J. Phys. Oceanogr.*, 36:1220–1236.

Ray, R. D. and Mitchum, G. T. (1996). Surface manifestation of internal tides generated near Hawaii. *Geophys. Res. Lett.*, 23:2101–2104.

Ray, R. D. and Mitchum, G. T. (1997). Surface manifestation of internal tides in the deep ocean: Observations from altimetry and island gauges. *Prog. Oceanogr.*, 40:135–162.

Rudnick, D. L., Boyd, T. J., Brainard, R. E., Carter, G. S., Egbert, G. D., Gregg, M. C., Holloway, P. E., Klymak, J. M., Kunze, E., Lee, C. M., Levine, M. D., Luther, D. S., Martin, J. P., Merrifield, M. A., Moum, J. N., Nash, J. D., Pinkel, R., Rainville, L., and Sanford, T. B. (2003). From tides to mixing along the Hawaiian Ridge. *Science*, 301:355–357.

Simmons, H. L. (2008). Spectral modification and geographic redistribution of the semi-diurnal internal tide. *Ocean Modeling*, 21(3):126–138.

St. Laurent, L. and Garrett, C. (2002). The role of internal tides in mixing the deep ocean. *J. Phys. Oceanogr.*, 32:2882–2899.

Staquet, C. and Sommeria, J. (2002). Internal Gravity Waves: From Instabilities to Turbulence. *Annu. Rev. Fluid Mech.*, 34:559–593.

Sun, L., Zheng, Q., Wang, D., Hu, J., Tai, C., and Sun, Z. (2011). A case study of near-inertial oscillation in the South China Sea using mooring observations and satellite altimeter data. *Journal of Oceanography*, 67(6):677–687.

Sun, O. M. (2010). *Identifying Two Steps in the Internal Wave Energy Cascade*. PhD thesis, University of California San Diego.

Sun, O. M. and Pinkel, R. (2012). Energy transfer from high-shear, low-frequency internal waves to high-frequency waves near Kaena Ridge, Hawaii. *J. Phys. Oceanogr.*, 42:1524–1547.

Toole, J. M. (2007). Temporal Characteristics of Abyssal Finescale Motions above Rough Bathymetry. *J. Phys. Oceanogr.*, 37:409–427.

Winters, K. B., MacKinnon, J. A., and Mills, B. (2004). A spectral model for process studies of rotating, density-stratified flows. *J. Atm. and Oceanic Tech.*, 21(1):69–94.

Xie, X. H., Shang, X. D., van Haren, H., Chen, G. Y., and Zhang, Y. Z. (2011). Observations of parametric subharmonic instability-induced near-inertial waves equatorward of the critical diurnal latitude. *Geophys. Res. Lett.*, 38(5):L05603.

Yao, N. C., Neshyba, S., and Crew, H. (1975). Rotary Cross-Bispectra and Energy Transfer Functions Between Non-Gaussian Vector Processes I. Development and Example. *J. Phys. Oceanogr.*, 5:164–172.

Yao, N. C. G. (1974). *Bispectral and Cross-bispectral Analysis of Wind and Currents off the Oregon Coast*. PhD thesis, Oregon State University.

Young, W. R., Tsang, Y. K., and Balmforth, N. J. (2008). Near-inertial parametric subharmonic instability. *J. Fluid Mech.*, 607:25–49.

Zaron, E. D., Chavanne, C., Egbert, G. D., and Flament, P. (2009). Baroclinic tidal generation in the Kauai Channel inferred from high-frequency radio doppler current meters. *Dyn. Atmos. Oceans*, 48(1):93–120.

Zaron, E. D. and Egbert, G. D. (2006). Estimating open-ocean barotropic tidal dissipation: The Hawaiian Ridge. *J. Phys. Oceanogr.*, 36:1019–1035.

Zilberman, N. V., Merrifield, M. A., Carter, G. S., Luther, D. S., Levine, M. D., and Boyd, T. J. (2011). Incoherent nature of M2 internal tides at the Hawaiian Ridge. *J. Phys. Oceanogr.*, 41(11):2021–2036.